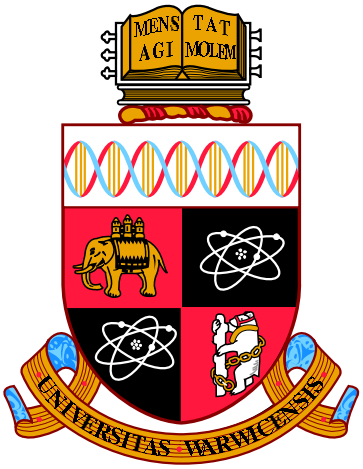

Structure and ferroelectricity at the atomic level in perovskite oxides.

by

Jonathan James Prescott Peters

Thesis

Submitted to the University of Warwick

for the degree of

Doctor of Philosophy

Department of Physics

July 2017

WARWICK
THE UNIVERSITY OF WARWICK

Contents

List of Figures

List of Tables

Acronyms

ABF	annular bright field.
ADF	annular dark field.
APB	anti phase boundary.
BF	bright field.
BTO	$BaTiO_3$.
CBED	convergent beam electron diffraction.
CCD	charged-coupled device.
D-LACBED	digital large angle convergent beam electron diffraction.
EDX	energy dispersive X-ray spectroscopy.
FFT	fast Fourier transform.
FIB	focussed ion beam.
FTJ	ferroelectric tunnel junction.
GPA	geometric phase analysis.
HDR	high dynamic range.
LACBED	large angle convergent beam electron diffraction.
LSMO	$(La_{0.7}Sr_{0.3})MnO_3$.
MFTJ	multiferroic tunnel junction.
MTJ	magnetic tunnel junction.
PIPS	precision ion polishing system.
PLD	pulsed laser deposition.
PNR	polar nano region.
PP	peak pairs.

PST Pb_2ScTaO_6.
PTO $PbTiO_3$.
PZT $Pb(Zr\,Ti)O_3$.

QCL quantum cascade laser.

SAED selected area electron diffraction.
SEM scanning electron microscopy.
SRO $SrRuO_3$.
STEM scanning transmission electron microscope.
STO $SrTiO_3$.

TDS thermal diffuse scattering.
TEM transmission electron microscope.
TER tunnelling electroresistance.
TMR tunnelling magnetoresistance.

XRD X-ray diffraction.

Acknowledgments

During my PhD I have had the privilege of working with many great people, without whom this thesis and I would be significantly worse off.

I must express a massive amount of gratitude to my supervisor, Dr Ana Sanchez, who has expertly guided me professionally and academically. I have never met anyone more qualified to be called a microscopist. Most importantly for me, she has also been a tremendous source of fun (and cakes).

Dr Richard Beanland, who has never failed to have a useful suggestion, has also helped immensely in elevating my work to the next level as well as teaching me the benefits of fiddling with multi-million pound equipment. Other microscopy academics, Dr Jeremy Sloan and Dr Neil Wilson, must also be thanked for making the group such an enjoyable place to work.

Within the group, I would like to specifically praise Dr Alex Marsden, who I have used as a role model and excellent influence. Dr Keith Evans and Dr Adam Dyson also need to be thanked for their more mischievous influences. Sam Marks deserves credit for being a fantastic friend and without him I would not have lived to see then end of my PhD. He has always been there to listen to my crap. I hope I have returned the favour.

I have also had great fortune to have worked with the microscope technicians, Steve York and Steve Hindmarsh, who have always been friendly and helpful with me, no matter how much equipment has been broken. Particular thanks to Steve Hindmarsh, who has wasted countless hours with me on the FIB.

I do not wish to ignore any other member of the microscopy group, all of

whom have answered my questions, listened to my answers and in general helped with every aspect of my PhD. In addition, I have made many friends, inside and outside of the university, who have helped keep my sanity.

Thanks should be extended to the 'functional electronic materials' group for their help. Particularly Geanina Apachitei, who not only provided me with samples and electrical measurements, but her great discussions as an intellectual and as a friend. Prof. Marin Alexe has also been indispensable in helping me understand ferroelectric systems and has always provided me with valued opportunities.

Finally, I would like to thank my family for their respite and love. At no point has my father's complete lack of scientific knowledge stopped him from making suggestions. My mother has never stopped wanting to spoil me and my brother has always shown an interest.

Declarations

I declare that this thesis contains an account of my research work carried out at the Department of Physics, University of Warwick, between October 2013 and June 2017 under the supervision of Dr A. M. Sanchez. The research reported here has not been previously submitted, wholly or in part, at this or any other academic institution for admission to a higher degree.

Parts of this thesis have been published by the author between October 2013 and June 2017:

- The experimental data in chapter 3 have been published in:

  Peters, J. J. P. *et al. "Polarization curling and flux closures in multiferroic tunnel junctions."* Nature communications **7,** 13484 (2016)

- All data and findings relating to geometric phase analysis in chapter 5 have been published in:

  Peters, J. J. P. *et al. "Artefacts in geometric phase analysis of compound materials."* Ultramicroscopy **157,** 91–97 (2015)

All the work presented here was completed by the author, except for the following:

- The image of the AlSb-GaAs interface in Fig. 1.17 was taken by A. Sanchez.
- The multiferroic tunnel junction devices examined in chapter 3 were produced by G. Apachitei.

- The electrical (tunnelling electroresistance and tunnelling magnetoresistance) measurements in chapter 3 and in Fig. 3.1(b) were performed by G. Apachitei.
- The Pb_2ScTaO_6 samples used in chapter 4 were provided by R. W. Whatmore.
- The quantum cascade laser sample in chapter 5 was provided by J. W. Cockburn.
- The $SrTiO_3$-$SrRuO_3$ sample in chapter 5 was provided by M. Alexe.

Additional publications by the author (not contained within this thesis) between October 2013 and June 2017:

- Huang, C. *et al. "Lateral heterojunctions within monolayer $MoSe_2$-WSe_2 semiconductors."* Nature materials **13,** 1096–1101 (2014)
- Doig, K. I. *et al. "Structural, optical and vibrational properties of self-assembled $Pb_{n+1}(Ti_{1-x}Fe_x)_nO_{3n+1-\delta}$ Ruddlesden-Popper superstructures."* Scientific reports **5,** 7719 (2015)
- Sanchez, A. M. *et al. "On the vertical stacking in semiconducting WSe_2 bilayers."* Materials science and technology **32,** 226–231 (2016)
- Nguyen, L. *et al. "Atomic defects and doping of monolayer $NbSe_2$."* Acs nano **11,** 2894–2904 (2017)
- Apachitei, G. *et al. "Antiferroelectric tunnel junctions."* Advanced electronic materials (2017)

Abstract

Ferroelectricity is a phenomenon that has been studied for nearly 100 years, forming one arm of the large field of ferroics that includes ferromagnetism and ferroelasticity. Ferroelectric materials have shown promise in a wide range of devices such as non volatile memory devices, micro mechanical actuators and infrared sensors. Further potential can be realised by combining the ferroelectric properties with other ferroic properties to form more complex devices. This thesis aims to leverage the power of transmission electron microscopy to examine ferroelectricity down to the atomic scale.

First, the polarisation in ferroelectric tunnel junction devices, consisting of an ultrathin ferroelectric between two electrodes, is studied in context of the depolarisation field created by bound charges in the ferroelectric. This drives the formation of vortex-type structures in the polarisation, however, the free charges in the electrodes act to screen the depolarisation field. This thesis investigates whether curling polarization structures are innate to ferroelectricity or induced by the absence of electrodes. Here it is shown that in unpoled ($La_{0.7}Sr_{0.3}$)MnO_3/$PbTiO_3$/Co ferroelectric tunnel junctions, the polarization in active $PbTiO_3$ layers 3.6 nm thick forms Kittel-like domains, while for 2.4 nm of $PbTiO_3$ there is a complex flux-closure curling behaviour resembling an incommensurate phase. Reducing the thickness to 1.2 nm, there is an almost complete loss of switchable polarization associated with an internal gradient. Additionally, the polarisation for thicker $PbTiO_3$ films extends into the ($La_{0.7}Sr_{0.3}$)MnO_3 whilst the 1.2 nm $PbTiO_3$ film is dominated by the substrate.

Next, the relaxor-like ferroelectric Pb_2ScTaO_6 has been examined, a highly dynamic system that is typified by the presence of polar nano regions that fluctuate rapidly in time. The properties of Pb_2ScTaO_6 are strongly dependent on the presence of ordering of the Ta and Sc ions into a chequerboard pattern. Here, highly ordered (> 85 %) Pb_2ScTaO_6 is examined in terms of its local ordering, where small, local fluctuations in the order are accompanied by disorder at anti phase boundaries. Furthermore, evidence for a phase transition at 220 K to the ferroelectric state is found from electron diffraction and dielectric data. The polar fluctuations are also examined, directly using dark field imaging and from scattering phenomena in atomic resolution scanning transmission electron microscopy. It is found that the polar fluctuations do not change in frequency or size as a function of temperature though electron beam effects cannot be excluded.

Finally, the application of geometric phase analysis, used to measure strain, is considered when applied to atomic resolution, Z-contrast images. It is demonstrated that, in such image, an additional phase can be present. If the structure changes from one area to another in the image (e.g. across an interface), the change in this additional phase will appear as a strain in conventional geometric phase analysis, even if there is no lattice strain. The origin of the artefact is formalised and strategies to avoid this pitfall are outlined.

Chapter 1

Introduction

1.1 Introduction

In Feynman's famous "Plenty of room at the bottom" talk in 1959 [1], he asked the question "What would the properties of materials be if we could really arrange the atoms the way we want them?" Whilst it may not yet be possible to exactly control the position of each atom on a large scale, he recognised the importance of their exact arrangement in a material [2].

This is of particular importance to perovskite oxides, where moving one atom a few tenths of an Ångstrom can have a profound effect on the properties of the material. The question then is: After a structure has been grown, how can the exact configuration of the atoms be determined?

In Feynman's same speech he recognised the important role of the transmission electron microscope (TEM) and the need to improve the resolution to measure such precise positions. These days, with the advent of aberration correctors [3–5], it is largely routine to image individual atoms in a material and measure their positions to picometre precision [6–10] as well as determine their chemical nature [11–13].

This opens the possibility to not only measure the exact structure that has

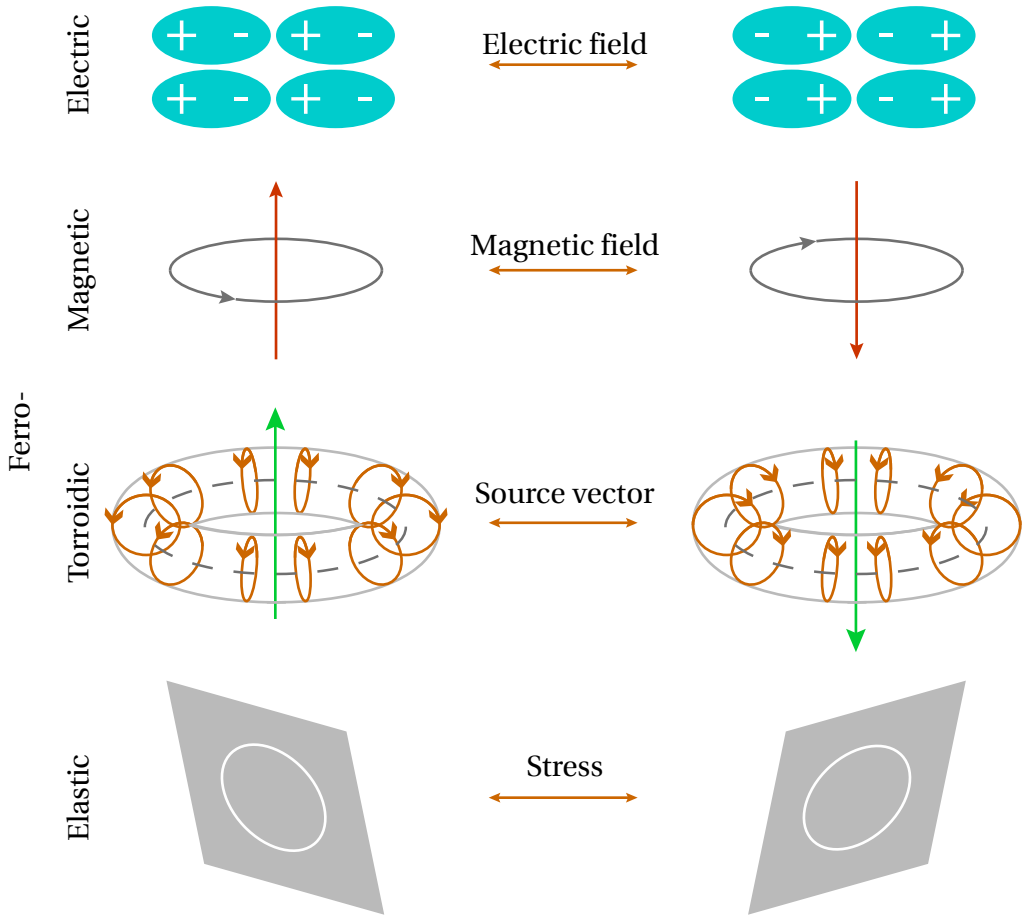

Figure 1.1: Schematic representing the four primary ferroic orders.

been grown, information that can be fed back to growers to help optimise growth techniques, but also to make measurements of functional properties at such small length scales.

This has become ever important in a world that desires ever smaller yet more power efficient electronic devices. Structures on the scale of < 14 nm are already being used in consumer devices and this number is expected to fall, making electron microscopy an indispensable technique for device characterisation.

Whilst semiconductors currently dominate the electronics field, oxide ferroelectrics are gaining increasing interest for use in non-volatile devices that utilise their spontaneous polarisation to maintain their data state without any power us-

age. Recent developments mean that such devices can be grown with length scales on the order of a few nanometres [14, 15].

This thesis aims to establish the appropriate methodology based on electron microscopy techniques to examine perovskite materials. Particular emphasis has been placed on atomic resolution imaging of heavy and light atoms to determine local functional properties, such as ferroelectricity and polarisation.

1.2 Ferroelectrics

Ferroelectrics form part of a larger class of materials known as ferroics (Fig. 1.1), the most famous of which is ferromagnetism, that often share similar concepts or principles. Ferroelectricity was first recognised by Valasek [16] in Rochelle salt in 1920 and the field has since seen intense research, particularly aided by the discovery of ferroelectricity in the simple perovskite oxide, $BaTiO_3$ (BTO), during the 1940s [17].

1.2.1 Ferroelectricity and polarisation

The term ferroics was coined by Aizu [18] to describe a material with several energetically equivalent states with a spontaneous order parameter (e.g. magnetisation, strain). When applying a conjugate field (e.g. magnetic field, stress) with a strength above a certain value (the coercive field), the system can be switched between the stable states. In the ferroelectrics studied in this thesis, the order parameter is the polarisation and the conjugate field is the electric field. Typically, ferroelectric materials are characterised by hysteresis loops in the polarisation with applied electric field, as shown in Fig. 1.2. Here the coercive field, E_{c}, can be seen at the points that the polarisation changes from positive to negative, in addition the polarisation at zero electric field is described as the remnant polarisation, P_{r}. In an ideal ferroelectric material, the remnant polarisation is the same as the polarisation with the

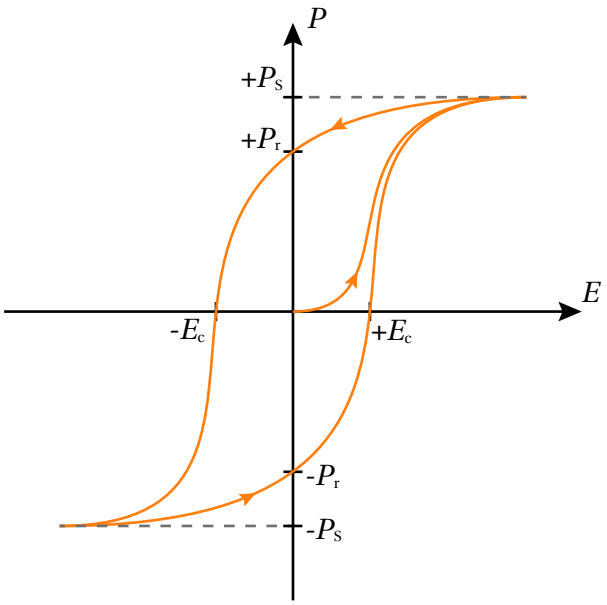

Figure 1.2: A typical hysteresis loop in ferroelectrics showing the polarisation, P, as a function of applied electric field, E. E_c is the coercive field, P_r is the remnant polarisation and P_S is the saturation polarisation.

full applied field, P_S. Importance should also be placed on the exact shape of the curve as imperfect dielectrics can also produce a hysteresis like curve [19].

All ferroelectrics are also piezoelectric, where an electric field is generated by an applied mechanical strain. Therefore ferroelectrics are popular for ultrasonic sensors and micro mechanical actuators. Furthermore, ferroelectrics exhibit the pyroelectric effect, where the spontaneous polarisation depends on the temperature, and have therefore found use as infrared sensors. At high enough temperatures, ferroelectrics enter a paraelectric phase where they posses no polarisation. The temperature at which this transition occurs is called the Curie temperature, analogously to ferromagnetism.

One reason that ferroelectrics evaded detection for so long is the ability for a single piece of a material to contain several domains of the different polarisation states at once. This formation of domains, that are necessarily separated by domain walls, is a key feature of ferroelectrics, particularly for devices. For instance, some

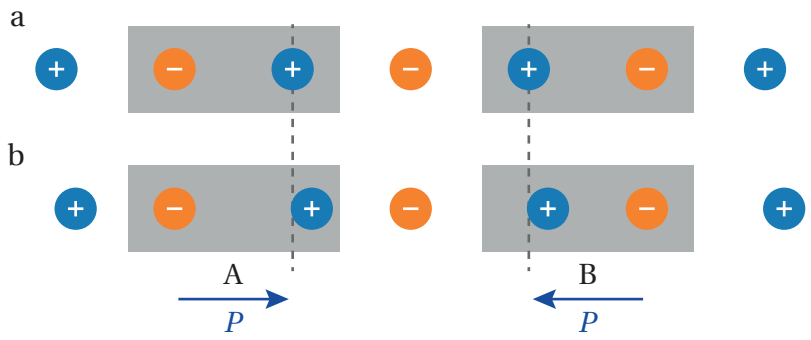

Figure 1.3: A simple 1D chain of alternating charges for a non-polar lattice, (a) and a polar lattice, (b), where the positive charges have been shifted to the right. A and B reference two choices of reference cell that produce different absolute measurements of polarisation.

devices use the polarisation to modulate a property of the device, such as conductance, and domains are used to form a high density of different states. In addition, domain walls have been shown to exhibit properties different from the bulk such as high conductance [20].

The exact definition of polarisation is perhaps not as trivial as might be expected. For some small, finite systems (i.e. molecules or small particles) it is possible to describe the polarisation, $\boldsymbol{P}$, simply as the dipole moment per unit volume, v. For discrete charges this is defined as

$$\boldsymbol{P} = \frac{1}{v}\sum_i \boldsymbol{r}_i q_i, \tag{1.1}$$

where $\boldsymbol{r}_i$ and q_i are the position and charge of each object respectively. This situation is not so clear for bulk solids. This is illustrated in Fig. 1.3 where simply by moving the reference frame, the measured polarisation is completely changed and even the non-polar structure appears polar when considering only the local scale. Originally this was a sticking point in the field until the introduction of the modern theory of polarisation [21–23]. This theory places emphasis on the change in polarisation, rather than absolute values, with reference to a non-polar state (i.e. one where the ions are at centres of inversion symmetry) [24]. This means that it is indeed valid

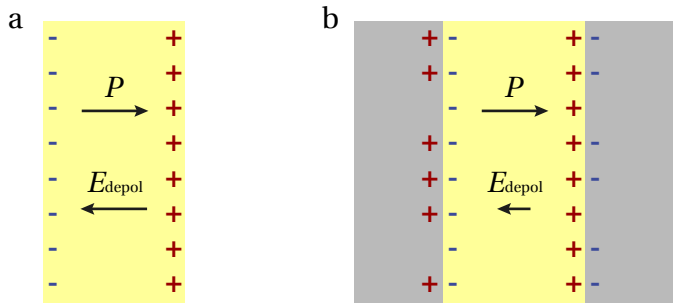

Figure 1.4: (a) Illustration of a ferroelectric thin film in vacuum showing the polarisation, P, the depolarisation field, E_{depol}, and the surface charges, $+$ and $-$. (b) The same system as in (a) but now with conducting electrodes. Plus and minus signs represent electric charge.

to measure the polarisation on unit-cell scale [25–30]. Usually the polarisation is measured within each unit cell of a crystal, but this is purely for convenience; as with the choice of structural unit cell, the cell used to measure polarisation can be at any point but a reference frame is often chosen that makes life easier (e.g. rational fractional position coordinates, ions at points of inversion symmetry etc.). Similarly, a full polarisation field could be calculated at every point but this does not readily yield any extra information compared to calculating polarisation with unit cell resolution.

1.2.2 Thin films

Until now, the presented review of ferroelectrics has ignored external or interface effects. With the development of growth techniques, such as pulsed laser deposition (PLD), the possibility of growing epitaxial thin ferroelectric films down to a few unit cells thick has been realised [14, 31–35] (see chapter 3). In these ultrathin film configurations, the surface to bulk ratio is drastically increased, compared to bulk or traditional thin films, and the surface effects can no longer be ignored. Considering a ferroelectric thin film in vacuum, if the polarisation is normal to the film, there will be a build up of bound, opposite charges at each interface (Fig. 1.4(a)). This charge splitting will create a depolarisation field, that acts to reduce the internal

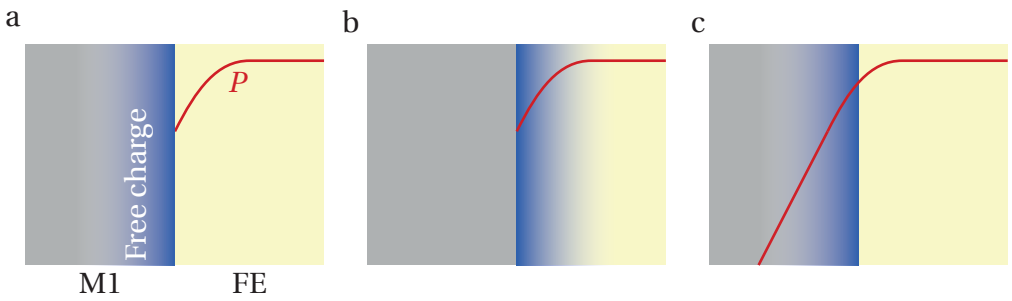

Figure 1.5: (a) Screening of polarisation, P (red line), bound charges by free charge (blue gradient) in the electrode, M1. (b) In-situ screening of the bound charge within the ferroelectric, FE, layer. (c) Polarisation extending into the electrode where bound charge can be in-situ screened by the free charge.

polarisation of the film.

An easy way to counter the depolarisation field is to simply change the polarisation direction to be in-plane with the film [36, 37]. Whilst this does negate surface charge effects, it also removes many of the possibilities for devices that rely on an out-of-plane polarisation. A more useful solution for devices is the addition of extra charges at the surfaces. This can be a result of the atmosphere the ferroelectric is in, adsorbants on the surface or, more commonly, the ferroelectric is grown as part of a more complex heterostructure. If the ferroelectric is sandwiched between conductive electrodes, the free charges in the metal can move so as to screen the bound charges at the interfaces and reduce the depolarisation field. Even in this case, it is rarely possible to be able to perfectly screen the bound charges exactly at the interface. The distance over which the electrode charges screen the ferroelectric charges is described by the Thomas-Fermi screening length (representative values are in the range of tenths of nanometres for metals and tens of nanometres for semiconductors) that is a function of the electronic density of states near the Fermi level [38]. However, it has been shown that the true screening length differs from the Thomas-Fermi value depending on the microscopic chemical environment at the interfaces [39, 40].

Because of the screening length and the fact that the polarisation cannot

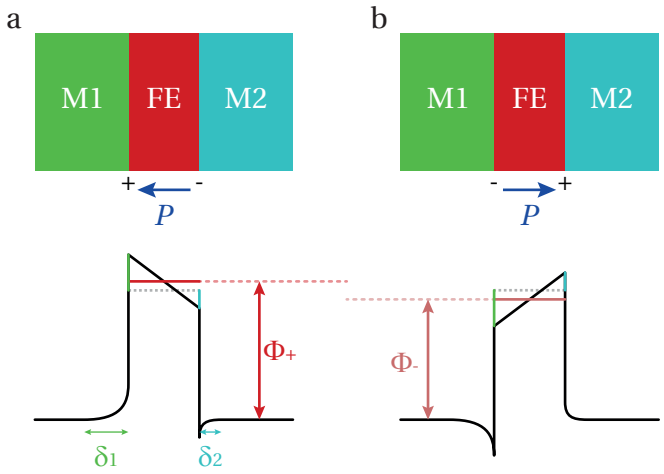

Figure 1.6: Schematics for a ferroelectric tunnel junction consisting of a ferroelectric, FE, between two conductive electrodes, M1 and M2, with different screening lengths, δ_1 and δ_2. Two barrier heights, Φ_+ and Φ_-, are present for the different polarisation, P, directions shown in (a) and (b). The grey dotted lines give the original barrier height and the solid red lines give the average barrier height.

abruptly change to zero [41], the bound charge is separated from the centre of gravity of the screening charges (Fig. 1.5(a)), effectively creating an interface capacitor [39, 42, 43], often negatively affecting the structures properties [44–46]. This effect is found to be much weaker for conductive metal oxide electrodes [44, 46] where the bound charges can be screened in-situ. One possibility is the presence of free charge in the ferroelectric (Fig. 1.5(b)), e.g. arising from doping or the contact phenomena [47, 48]. Also it is possible that the bound charge displacements extend into the electrode, where they can be screened in-site by the electrode free charge (Fig. 1.5(c)) [49].

For a ferroelectric capacitor, the difference in screening, and associated additional electrostatic potentials at the interfaces [50], forms the basis for a device called the ferroelectric tunnel junction (FTJ) [51]. Here, an ultrathin ferroelectric barrier is placed between two asymmetric electrodes so that a current can tunnel across the barrier. Due to the imperfect screening, there will be an increase or decrease in the potential if the polarisation points towards or away from the interface,

respectively. Due to the asymmetric screening, the average barrier height will be modulated by the polarisation, as shown in Fig. 1.6, and in turn will modulate the tunnel current. This device has use for non-volatile memory devices and can be combined with a magnetic tunnel junction (MTJ) to form a 4-state multiferroic tunnel junction (MFTJ) device [35, 40, 52].

Strain effects should also be considered in thin films due to the piezoelectric effect. If the ferroelectric film is grown epitaxially on a substrate, depending on the lattice parameter of the substrate, strain may act to enhance the polarisation [53, 54]. In this case there will be competition between the strain reinforcing the polarisation and the depolarisation field trying to reduce it. Even accounting for charge screening effects, some depolarisation field may still be present and the ferroelectric may form domains to reduce surface charge, as will be discussed further in the next section.

1.2.3 Ferroelectric domains

By forming domains within a ferroelectric, average surface charge can be reduced to zero. However, electric fields originating from the formation of domains are not energetically favourable and so their formation depends on the strain in the system and the depolarisation field without domains. The form of domains and domain walls is in many ways analogous to ferromagnetics, as was first formalised by Kittel [36] in 1946. Outside of a pure in-plane polarisation, Kittel considered two domain configurations.

First, domain walls where the polarisation switches 180° across the boundary, as demonstrated in Fig. 1.7(a), and which are now known as Kittel type domains. Second, so-called Landau-Lifshitz flux-closure domains where the 180° domain walls become in-plane polarised at the top and bottom electrode (Fig. 1.7(b)). This closure reduces the surface charge as the positive surface of an out-of-plane domain is accounted for by the negative surface of the closure domains (and vice versa). This

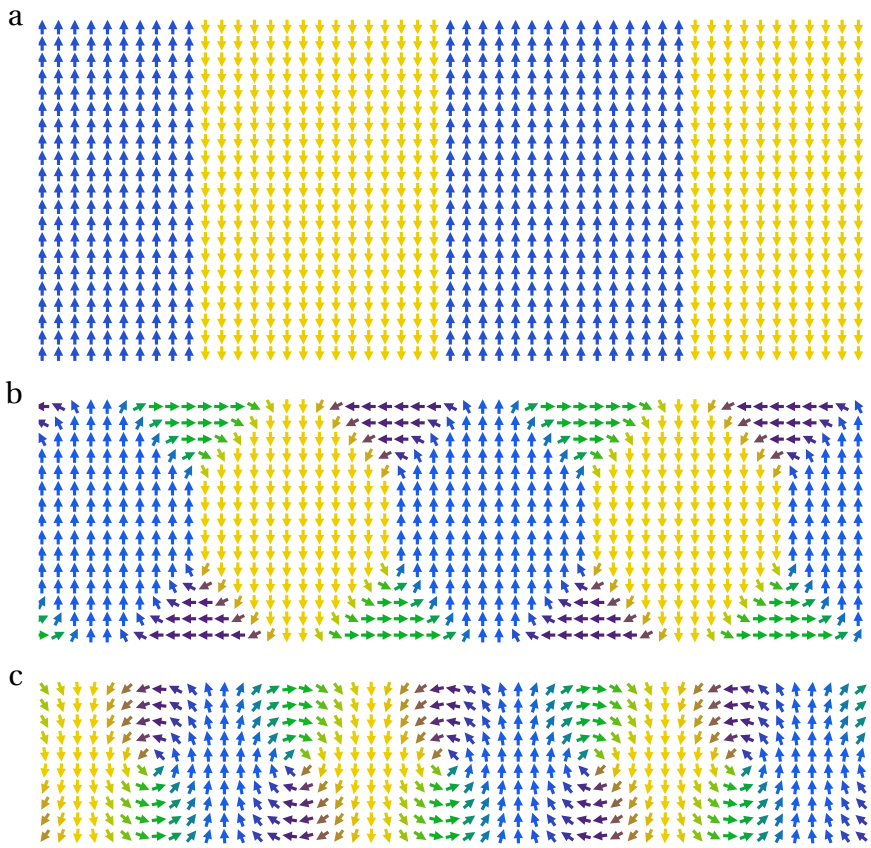

Figure 1.7: (a) Kittel, (b) Landau-Lifshitz and (c) vortex type domain configurations. The arrow directions and colour correspond to the polarisation direction.

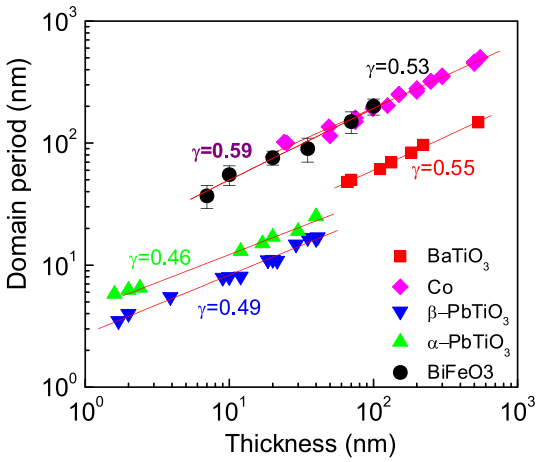

Figure 1.8: Domain periods for a given film thickness in different materials. Note that data for ferromagnets is also given. Data reproduced from Catalan *et al.* [58].

configuration may have an energy penalty due to the strain between the domains and the flux closure as well as the flux closure and the electrodes. The formation of the different type of domains is then dependent on the energy due to the charge separation that is more reduced in the Landau-Lifshitz configuration and the domain wall/interface strain that is typically reduced in the Kittel-type domains.

Since the work by Kittel, an additional domain structure has been described. The generation of polarisation vortices, where the polarisation continuously curls around a central point, have been discovered where multiple vortices with alternating chirality form a domain structure as shown in Fig. 1.7(c) [55, 56]. There is little bound surface charge compared to other domain configurations, though the strain penalty is higher due to the continuously changing ferroelectric axis. Vortex domains are of particular interest as they present the theoretical smallest domains that can be switched and therefore will provide the highest device densities [57].

In regards to thin films, when the film thickness decreases, the distance between bound charges at the interfaces is reduced and the depolarisation field is increased. This means that simply by reducing the film thickness, different domain structures can be induced to compensate for the depolarisation field. Considering

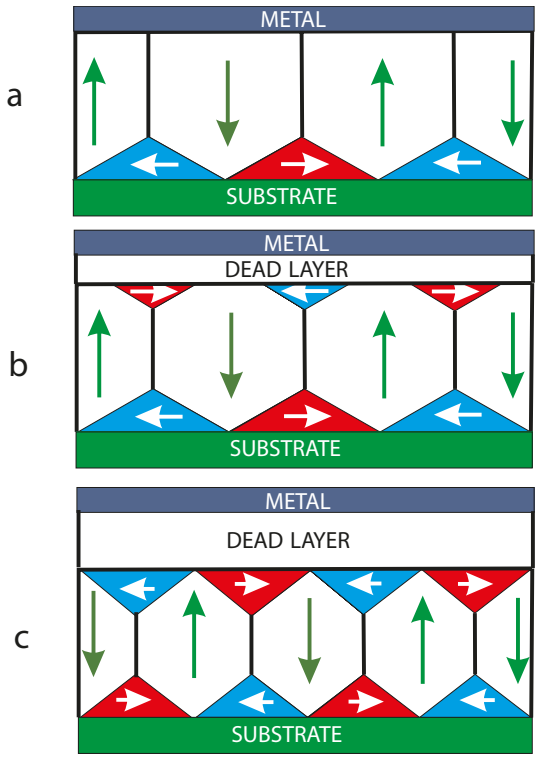

Figure 1.9: (a)-(c) The effect of decreasing the screening ability of one electrode by introducing an increasing dead layer. Reproduced from Prosandeev & Bellaiche [61].

this effect as well as strain effects, the periodicity of the domain can be described as

$$\omega = \sqrt{\frac{\sigma}{U}d} \tag{1.2}$$

where ω is the domain period, σ is the energy density of the domain walls, U is the energy density of the domains and d is the thickness of the films [59, 60]. Equation 1.2 is known as the Landau-Lifshitz-Kittel scaling law (often just called the Kittel scaling law). This has the effect that, as the film thickness is decreased, the domain widths are decreased which has been shown to hold for a wide range of thicknesses and materials, as shown in Fig. 1.8.

It is possible, and sometimes desirable [50], that electrodes on the ferroelectric are asymmetric (i.e. the conductivity is different for the two electrodes).

Additionally, defects from the growth or vacancy accumulation may create a dead layer that separates the bound charges and the screening electrode charges. This then creates an asymmetric screening of the bound surface charges in the ferroelectric and can influence the domain structure. First principles methods have shown that the change in screening from the presence of a dead layer significantly alters the formation of flux-closure or 180° domain walls at the surfaces, as shown in Fig. 1.9. This dead layer is analogous to a poorly conducting electrode where the large screening lengths create a separation of the free charge in the electrode and bound charge in the ferroelectric. Therefore, an excellent conductor at one surface of the ferroelectric and a poor conductor at the other creates half Kittel, half Landau-Lifshitz domain walls, shown in Fig. 1.9(a) [61]. Here the screening of the good conductor negates the requirement of flux-closure domains but the other surface still forms flux-closure domains to account for the lack of screening from the poor conductor. Additionally, changing the conductance of one of the electrodes results in a change of the domain width.

1.3 Perovskite oxides

Perovskite oxides are some of the most studied ferroelectric structures. Named after the mineral perovskite, $CaTiO_3$, the prototype perovskite structure is simple cubic and generally has the composition ABO_3 where A and B represent two cations alongside the oxygen anions. It is these anions and cations and, most importantly, the local displacements and distortions in the crystal that form the basis of ferroelectricity in such materials.

1.3.1 Paraelectric phase

At high temperatures, perovskite oxides assume a paraelectric phase where the structure is non-polar. For many perovskites this phase is cubic with a lattice pa-

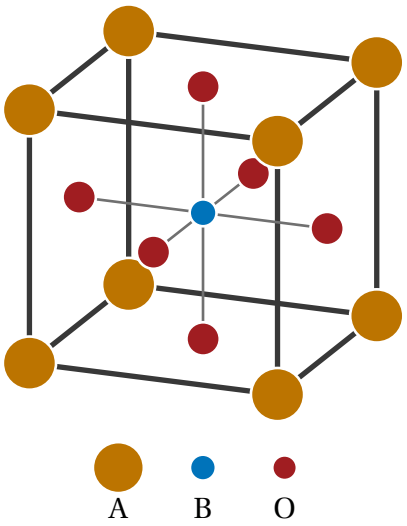

Figure 1.10: The cubic ABO_3 structure.

rameter of ~ 4 Å and $Pm\bar{3}m$ space group, whose centrosymmetry means the anions and cations must be arranged in a non polar form. The structure is shown in Fig. 1.10 with the unit cell centred around the B cation, oxygens on the cube faces and A cations on the cube vertices. A notable characteristic of the perovskite structure is the oxygen octahedron that is centred around the B cation. It can be imagined that a number of perturbations of the cation and anion positions can result in a polarisation and, at lower temperatures where bond distances are more restrained, can result in ferroelectricity.

1.3.2 Ferroelectric phases

The origin of ferroelectricity in the perovskite structure can be attributed to distortions in the lattice as restraints are placed on the interatomic distances at lower temperatures. This can be measured by a tolerance factor, t, given by Goldschmidt [62] as

$$t = \frac{r_A + r_O}{\sqrt{2}\,(r_B + r_O)} \tag{1.3}$$

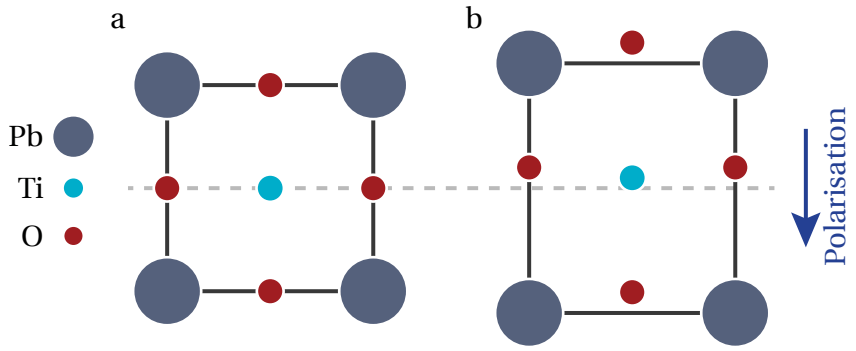

Figure 1.11: Schematic of the changes in $PbTiO_3$ from the paraelectric phase, (a), to the ferroelectric phase, (b). The grey line shows a mirror plane that is broken in the tetragonal ferroelectric structure.

where r_A, r_B and r_O are the radii of the A, B and O ions respectively. In the case of $t = 1$, the structure can adhere to the centrosymmetric structure and remains paraelectric. For $t > 1$, the B cation is too small for the oxygen octahedron and is free to move away from the point of centrosymmetry. With $t < 1$, the small A ion allows the oxygen octahedron to rotate, as will be discussed later. This tilting usually does not coexist with ferroelectricity [63].

The picture is more complex in the case of $PbTiO_3$ (PTO), a material that is a focus for this thesis, in that there exists hybridisation between the Pb and Ti leading to a strain that stabilises a tetragonal structure. This further induces hybridisation between the Ti and O, giving an off centring of the Ti. PTO therefore assumes a $P4mm$ structure where both the O and Ti are displaced in the same direction relative to the Pb. The valences of the atoms are Ti^{+4}, Pb^{+2} and O^{-2} and given that the displacement of the O is approximately three times that of the Ti, the polarisation is in the direction opposite to the oxygen displacement. In PTO this is along the tetragonal axis. This is illustrated in Fig. 1.11 where the full structural change is illustrated.

For different structures, different ferroelectric displacement axes may be possible and for some structures there is more than one ferroelectric phase. For example, BTO transitions from the cubic paraelectric structure to a tetragonal structure,

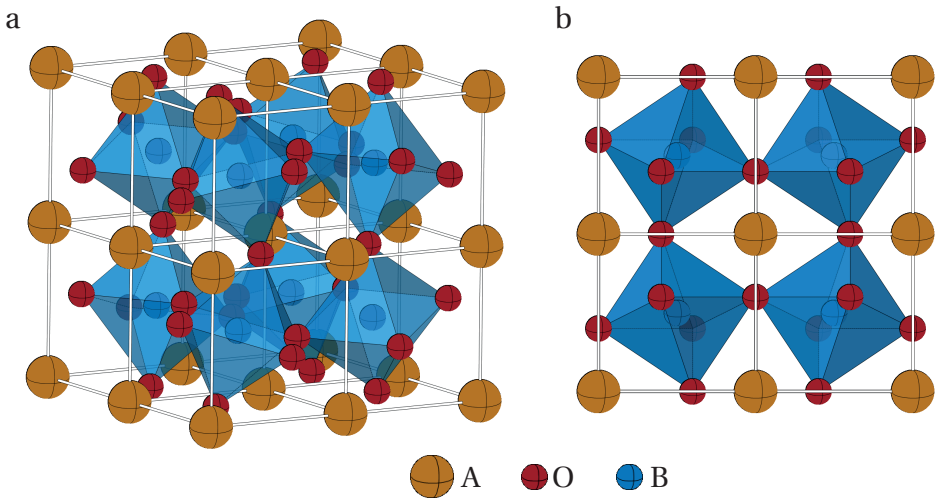

Figure 1.12: (a) 3D model of an example structure with the $a^+a^+a^+$ tilt system. The surfaces of the oxygen octahedra have been filled in blue. (b) Projection of the same structure along one of the cubic axes. Note the tilts have been exaggerated for clarity.

but on further cooling orthorhombic and then rhombohedral structures are formed. Each of these has a different polarisation axis, moving from $\langle 100 \rangle$ to $\langle 110 \rangle$ and finally $\langle 111 \rangle$.

A more complete description of ferroelectricity uses the condensing of a so-called soft phonon, where the ionic displacements lead to a decrease in the system energy. As the temperature is reduced, this soft mode condenses, or becomes frozen, leaving the ionic displacements. This stabilisation of polar distortions depends on short range (nearest neighbour) forces between the cations and long range dipole interactions. A full understanding requires knowledge of the specifics of the bonding between ions and has been studied via first principles [64, 65].

1.3.3 Octahedral tilting

A common structural phenomenon in perovskites is the tilting/rotation of the oxygen octahedra, typically this occurs where t is less than 1 (Eq. 1.3). These rotations can take multiple forms and a formalism was developed by Glazer [66] in order to

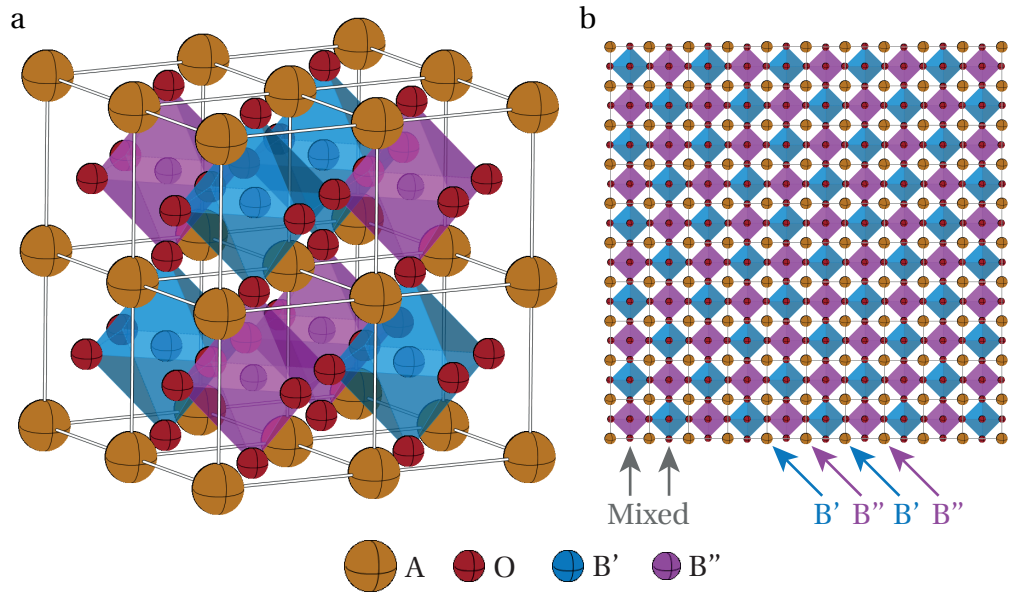

Figure 1.13: Example chequerboard (rock salt) ordered perovskite in 3D, (a), and for a single layer of octahedra, (b), viewed from a $\langle 100 \rangle$ direction. The oxygen octahedra have been highlighted in the colour of the B-site cation they encapsulate.

quickly describe the structure. In this notation, the tilting is described as three separate rotations around the cubic (or pseudocubic) axes of the perovskite unit cell. These separate tilts are assigned a letter (a, b, c) depending on their relative magnitude. Looking along an axis, the rotation of successive octahedra can be in phase or out of phase and is described using a superscript $+$ or $-$ respectively; a superscript 0 indicates no tilting. For example, a crystal that has no tilt around the x-axis, in phase tilt about the y-axis and the same magnitude tilt about the z axis, but out of phase, would be described by the notation $a^0b^+b^-$. A tilted structure, $a^+a^+a^+$, is schematically shown in Fig. 1.12. In total, 23 distinct tilt systems exist (including the no-tilt system) though more complicated structures do exist with tilts that can only be described with a longer periodicity than two unit cells.

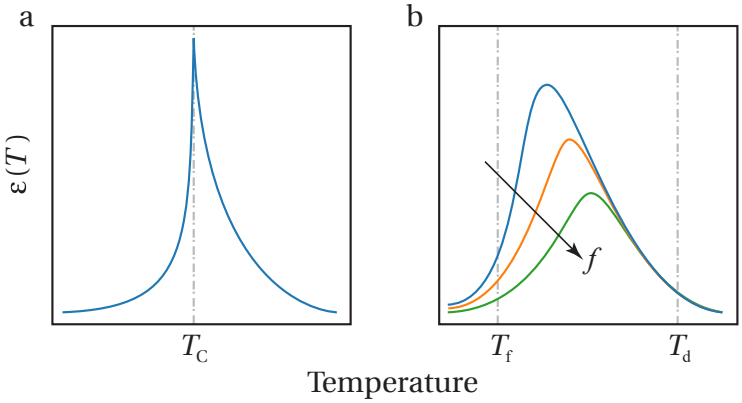

Figure 1.14: Demonstration of the dielectric response for a standard ferroelectric, (a), and a canonical relaxor, (b), as a function of temperature. For the relaxor, a range of frequencies, f, are shown. T_d and T_f are the temperatures where polar nano regions form and freeze respectively. T_C is the ferroelectric Curie temperature. Reproduced from Hirota, Wakimoto & E. Cox [67].

1.3.4 Double perovskites

In some cases where there is more than one species occupying a site in a perovskite, instead of forming a random distribution of elements (as with $Pb(Zr\,Ti)O_3$ (PZT)), there will be some degree of chemical ordering. This can result in multiple structures including chequerboard ordering, column ordering and layer ordering. Systems with ordered B-sites tend to arrange themselves in a chequerboard fashion whereas A-site ordering usually results in layer by layer ordering. This work is only concerned with systems with the stoichiometry $A_2B'B''O_6$ (sometimes referred to as $AB'_{0.5}B''_{0.5}O_3$) that results in the chequerboard or rock-salt ordering. This is demonstrated in Fig. 1.13 where the B-site alternates along any of the cubic axes, conversely, the cations form single species columns along the $\langle 110 \rangle$ axes. The extent of the ordering can vary and is described by the order value, Q, that give the fraction of the structure that is ordered.

Table 1.1: Characteristic temperatures for relaxors with typical values taken for Pb_2ScTaO_6.

Temperature	Symbol	Description	Value
Burns	T_d	Boundary between paraelectric phase and formation of polar nano regions	700 K [68]
Intermediate	T^*	Onset of coupling between different polar nano regions	500 K [68]
Dielectric max	T_m	Temperature of the dielectric maximum	300 K [69]
Curie	T_C	Transition to standard ferroelectric domains	$T_\mathrm{C} \approx T_\mathrm{m}$ [70]
Freezing	T_f	Polar nano regions freeze into a non-ergodic state	270 K [71]

1.4 Relaxor ferroelectrics

Relaxor ferroelectrics form a special subset of ferroelectrics that exhibit a range of peculiar phenomena. The most common measurement used to identify a relaxor is the dielectric spectrum that shows phase transition given by a diffuse peak with a strong frequency dependence, shown in Fig. 1.14. Though plenty of the underlying mechanisms are not fully understood, the diffuse phase transition can be associated with the presence of polar nano region (PNR)s or polar tweed, small polarised regions that fluctuate between several states in time (often described as flickering). PNRs are sometimes distinguished from polar tweed as being strictly from a canonical relaxor (i.e. lower ordered Pb_2ScTaO_6 (PST)), where tweed arises in the non-relaxor state, though there is a very close relationship between them [72]. The ergodic nature of these fluctuations means that averaging over either space or time results in a net zero polarisation. The nucleation of these PNRs occurs at the Burns temperature, T_d, that is greater then temperature of the peak in the dielectric spectrum [73]. The Curie-Weiss law used to describe ferroelectric transitions is only valid above T_d in relaxors, between T_d and the transition temperature a quadratic relationship is required [74]. On further cooling below T_d, the polar nano regions

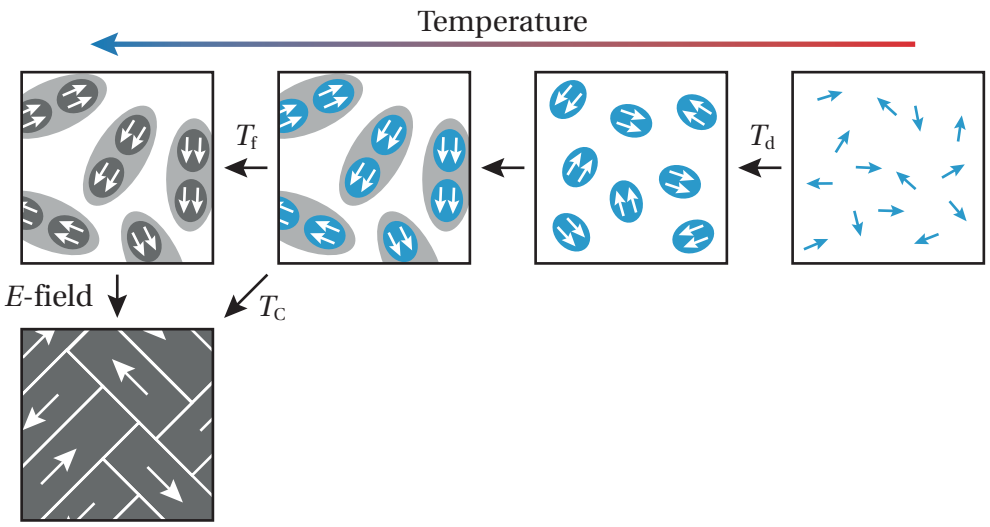

Figure 1.15: Illustration of the characteristic temperatures in a relaxor that are described in Table. 1.1. Arrows indicate electric dipoles where blue indicates dynamic fluctuations and dark grey indicates static dipoles.

begin to couple via their electric fields at the intermediate temperature, T^*, and the point of the dielectric maximum is reached at T_m. At low temperatures, the dynamic PNRs can freeze, either by transforming into a non-ergodic relaxor state at T_f, where the PNRs remain but are static, or by transitioning into a ferroelectric state below T_C. A summary of the characteristic temperatures in the relaxor PST can be seen in Table 1.1 that are also illustrated in Fig. 1.15. It should be noted that a relaxor is still a ferroelectric and applying an electric field will still induce a corresponding polarisation, at low temperatures which will change the non-ergodic, frozen PNRs to a conventional ferroelectric state.

The extent of the B-site ordering parameter, Q, plays a large role in the properties of the relaxor. The diffuse transition temperature decreases with decreasing order and in crystals with high enough order, the system is no longer truly a relaxor and does not exhibit the dielectric peak shift with frequency. Nevertheless, transitions similar to those described in Table. 1.1 have been measured as well as the presence of fluctuating polar regions [72] (sometimes called tweed to distinguish them from PNRs in relaxors).

This order dependence leads to initial theories by Smolensky [75] and Isupov, Pronin & Sizykh [76] that explain the diffuse phase transition as a result of inhomogeneity in the local chemical ordering. If the crystal can be described as a collection of regions, each of different ordering and with its own transition temperature, then the macroscopic crystal will see a smeared transition resulting from spread of transitions in the local structure. This theory has the advantage of explaining that if the average degree of ordering is higher than the maximum of the phase transition is different. Cross [77] proposed an analogy to superparamagnetism, called superparaelectricity, as a model for relaxors where the thermal energy of the system is comparable to the energy required to reorient the polarisation. However, the polarisation direction is not truly random but is aligned to one of the crystallographic polar directions, leading to grouping or formation of PNRs. This was further developed by Bokov [78] who included effects of local elastic and electric fields. So far, these theories have assumed PNRs to be embedded in a cubic or paraelectric matrix and have several pitfalls such as the inability to explain the transition from relaxor to ferroelectric under an external electric field.

A second approach to describe relaxors involves the inclusion of random fields where the formation of polar regions arises from the competition between the energy of domain walls and the energy of the domains themselves [79–81]. In this model, the crystal consists entirely of domains that are separated by domain walls with a thickness comparable to the domain width. The presence of random fields from sources such as compositional fluctuations provides the driving force for the fluctuations [80].

PST is a common relaxor ferroelectric that has seen particularly intense study due to its strong potential for use in infrared detectors [82]. Typical values of the characteristic temperatures for PST are given in Table. 1.1 with the dielectric maximum being roughly at room temperature, though the exact value depends on the extent of the ordering in the material (given by the fraction Q). If the ordering is

high enough, PST is no longer a true relaxor, this crossover happens at Q values around 0.75 to 0.82 [83] though frequency independence of the dielectric maximum has been seen in crystals with ordering as low as $Q = 0.55$ [84]. In this highly-ordered, non-relaxor state, equivalent characteristic temperatures are still measured by acoustic emission at similar temperatures to those given in Table. 1.1. This indicates that there is still a fluctuating polar structure and the crystal does not undergo a simple paraelectric to ferroelectric transition of a conventional ferroelectric. At levels of order greater than $Q = 0.85$, it has been reported that there is an incommensurate modulated anti-ferroelectric phase in the range of $\sim 220 - 300$ K [72, 85, 86]. In this phase, the polarisation will vary periodically along some crystallographic direction, changing in sign from positive to negative [85].

Structural studies have also been conducted on PST. At high temperatures, it is agreed that a simple, cubic structure with space group $Fm\bar{3}m$ gives the paraelectric phase. The low temperature phase is generally agreed to be rhombohedral (either $R3$ or $R3m$) [87, 88]. Neutron diffraction studies have shown the low-temperature, ferroelectric structure to be $R3$ in a crystal with ordering $Q = 0.52$. The structure gives rise to Pb ion displacements and no octahedral tilting is observed [89]. Additionally, direct observations of the ferroelectric domains have been made and note that there is no direct interaction between the order and the domain structure [69, 86, 90]. Several studies have also indicated that the size of the PNRs increases with decreasing temperature in addition to the fluctuation frequency of the PNRs [91–93].

1.5 Strain measurements from atomic resolution images

Strain is an important component to many systems. It has already been shown that strain can enhance ferroelectricity in a thin film and many other functional properties can be created, enhanced or destroyed by strain [94–98]. Strain measurements

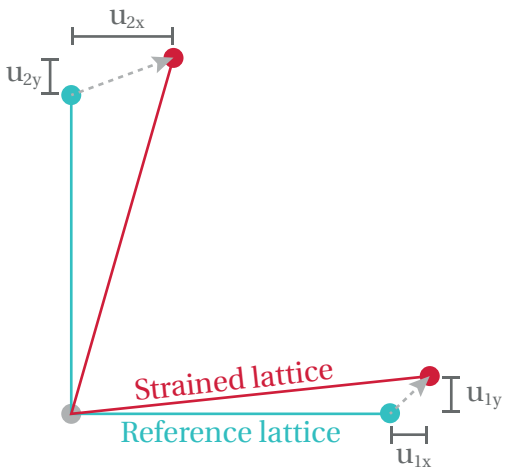

Figure 1.16: Demonstration of strain for a simple 2D case. The displacement field, u at each point describes the displacement vector from the reference lattice (blue) to the measured lattice (red).

are also useful for growth optimisation, where buffer layers are often used to compensate for lattice mismatch. In general, the distortion of a lattice is given by

$$e = \begin{pmatrix} e_{xx} & e_{xy} \\ e_{yx} & e_{yy} \end{pmatrix} = \begin{pmatrix} \frac{\partial u_x}{\partial x} & \frac{\partial u_x}{\partial y} \\ \frac{\partial u_y}{\partial x} & \frac{\partial u_y}{\partial y} \end{pmatrix} \tag{1.4}$$

where u_x and u_y are the displacement fields in the x and y directions, shown in Fig. 1.16. The strain, ε, is defined as the symmetric components of Eq. 1.4 and the antisymmetric part gives the rotation, ω. These can be calculated as

$$\varepsilon = \frac{1}{2}\left(e + e^{\mathrm{T}}\right) \tag{1.5a}$$

$$\omega = \frac{1}{2}\left(e - e^{\mathrm{T}}\right), \tag{1.5b}$$

where e^{T} is the transpose of the distortion matrix. It should be noted that whilst Eq. 1.5a is the strict definition of strain though Eq. 1.4 is often also referred to as the strain of the system. Multiple techniques exist for measuring the deformation and strain, some of which require special acquisition or even apparatus [99, 100].

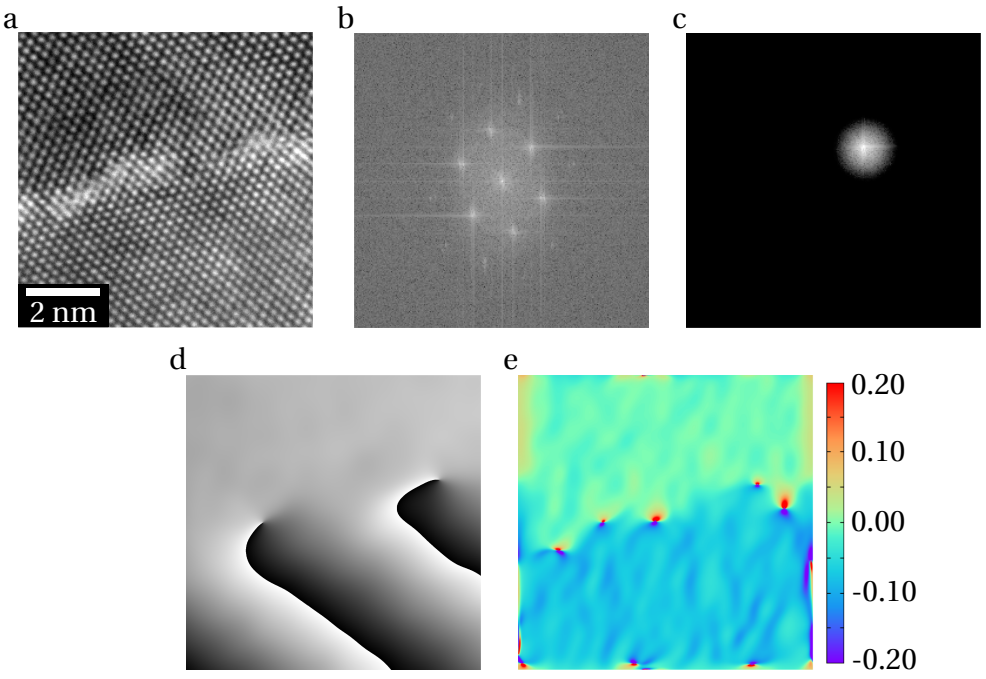

Figure 1.17: (a) High resolution transmission electron microscope image of a AlSb-GaAs interface. (b) Fast Fourier transform (FFT) of (a). (c) Masked FFT. (d) Phase image, P_{g}. (e) Strain image produced using (d) along and another $\boldsymbol{g}$ vector.

However, it is also possible to measure strain from any image with lattice resolution (e.g. a TEM image) which is a task of measuring the displacement vectors of the atom/lattice positions. Three main methodologies have been developed for measuring strain from atomic resolution images: geometric phase analysis (GPA) [101], peak pairs (PP) [102] and template matching [103].

1.5.1 Geometric phase analysis

GPA is a technique performed in Fourier space, and measures the phase of lattice planes from an image to calculate the displacement vectors. First, an image, $I(\boldsymbol{r})$, needs to be defined as a Fourier series,

$$I(\boldsymbol{r}) = \sum_{\mathrm{g}} H_{\mathrm{g}}(\boldsymbol{r}) \exp(2\pi i \boldsymbol{g} \cdot \boldsymbol{r}), \tag{1.6}$$

where $\boldsymbol{r}$ is the position in the image and $\boldsymbol{g}$ is the position in reciprocal space. The Fourier coefficients, H_g, are defined as

$$H_g(\boldsymbol{r}) = A_{\mathrm{g}}(\boldsymbol{r}) \exp(iP_{\mathrm{g}}(\boldsymbol{r})). \tag{1.7}$$

Here, A_{g} and P_{g} define the amplitude and phase of the corresponding sinusoidal fringes. Considering Eqs. 1.6 and 1.7, the image can be considered as the sum of a set of perfect lattice planes, defined by $\boldsymbol{g}$ vectors, with phase shifts given by P_{g}. If a Bragg spot in Fourier space is selected using a circular mask centred at a particular $\boldsymbol{g}$, the inverse Fourier transform results in a complex image, $H'_{\mathrm{g}}(\boldsymbol{r})$. The phase changes from the reference, perfect lattice (and therefore displacement, $\boldsymbol{u}$) can then be defined as

$$P_{\mathrm{g}}(\boldsymbol{r}) = \text{Phase}\left[H'_{\mathrm{g}}(\boldsymbol{r})\right] - 2\pi\boldsymbol{g}\cdot\boldsymbol{r} = -2\pi\boldsymbol{g}\cdot\boldsymbol{u}. \tag{1.8}$$

To calculate the strain in all directions, Eq. 1.8 needs to be calculated for two, non-collinear $\boldsymbol{g}$ vectors. From these two phase images, the displacement field is calculated as

$$\begin{pmatrix} u_x \\ u_y \end{pmatrix} = -\frac{1}{2\pi} \begin{pmatrix} g_{1x} & g_{1y} \\ g_{2x} & g_{2y} \end{pmatrix}^{-1} \begin{pmatrix} P_{\mathrm{g1}} \\ P_{\mathrm{g2}} \end{pmatrix}. \tag{1.9}$$

where the vectors $\boldsymbol{g}_1$ and $\boldsymbol{g}_2$ are the Bragg spots masked to generate the phase images P_{g1} and P_{g2}, respectively. Subscript x and y indicate the x and y components of the vectors. From this, Eq. 1.4 and Eq. 1.5a can be used to find the strain.

Due to the inherent image filtering when masking the Bragg spots, GPA provides a robust method of measuring strain that requires little or no image processing. Hence, GPA has become a popular choice for quick and easy analyses. Care needs to be taken with the choice of mask, as the resolution in the strain image is determined by the mask size [104]. A large mask will give more resolution but can also introduce artefacts such as noise or at extremes will also include components from

other Bragg spots.

1.5.2 Peak pairs

PP works in real space, using a much more direct and intuitive method of measuring the displacement vectors [102]. First, the peaks in the image must be identified which usually involves image filtering. Usually, the peaks are initially identified at pixel accuracy by finding local maxima. Later, peaks positions can be refined to sub-pixel accuracy, often using parabola or Gaussian fitting. Once all peaks have been found, two reference basis vectors need to be defined, this can be done in a similar fashion to GPA, using Bragg spots in the fast Fourier transform (FFT), or by measuring the distance of multiples of the vector in real space and then averaging. For each peak position, corresponding partners are found that are separated by the basis vectors. It is then easy to find the distances between each peak and its pair, and, by comparison to the reference basis vectors, the displacement field, u, can be found. The main difference to GPA, is that the displacement field is found at a set of discrete positions (the peaks) instead of at every pixel. To get a full displacement/strain field, interpolation methods must be employed.

This method has found popularity due to its intuitiveness and also the ability to process oversampled images, where GPA would struggle due to the compactness of the Bragg spots. Additionally, PP can be less computationally heavy [102], though this is not as much of a concern with modern computing power. However, the presence of noise means that the image usually needs to be filtered in order to identify the atom column peaks and this filtering can introduce shifts in the peak positions. Additionally, due to the need for interpolation to get the full strain field (i.e. one defined at every pixel), caution needs to be taken that spurious information is not being added to the data.

1.5.3 Template matching

Template matching can be considered an extension of the PP method, differing only in the method that lattice points are identified [103]. Instead of peak finding from maxima in the pixel values, a template image is created and, through the use of cross correlations, is found within the image. The template is often of the unit cell, but can be of any particular feature to be identified (e.g. the silicon dumbbells in the 110 projection). The positions where the template has the closest correlation are then used as the input for the peak pairs method where the distance between the template positions is compared to a pre-defined reference. This reference can be defined by the template itself or an additional measurement of lattice spacings in a strain free region. Template matching has the advantage of being robust to noise, though does require the user to generate the template and also may not produce predictable results around defects.

1.6 Thesis outline

In this thesis, focus is placed on using electron microscopy to examine materials in terms of their atomic structure, dynamics and properties. Various TEM techniques have been employed, ranging from advanced atomic resolution imaging to more traditional techniques such as selected area electron diffraction (SAED). To back these techniques up, modern computing power has been leveraged to extract information from these images that previously evaded discovery. Two main materials are the focus of this thesis, PTO and PST. For two structures with similar prototype phases, the functional properties and phenomena are vastly different.

Firstly, the experimental equipment and methods that have been employed in this thesis are described in chapter 2. As TEM is a major component of this thesis, this chapter covers the image formation mechanisms as well as the various operation modes that have been used. Additionally, the specimen preparation has

been detailed as well as a description of the actual equipment used. Finally, the complementary techniques, such as the computation and dielectric spectroscopy, have been explained.

The first results in chapter 3 examine the popular ferroelectric PTO as an ultrathin (< 4 nm) active layer in a working MFTJ device. At such thicknesses, the interfaces of the layer play a much stronger role that in thicker films or bulk materials, and the consequences of these surfaces is explored in context with the ferroelectric polarisation. Accurately measuring the polarisation on such scales requires the precise determination of all the atom positions and their relative shifts. For materials containing both heavy (Pb) and light (O) atoms, imaging every atom species is normally not possible and requires special imaging modes. The results shed light on the structure of polarisation in a working device, differing from the simple configurations shown in Fig. 1.7.

Next, chapter 4 places focus on highly-ordered, bulk PST, a crystal that is usually a relaxor ferroelectric, but at the levels of order studied diverges from canonical relaxor behaviour. However, the system still exhibits a wide range of phenomena, many of which are analogous to true relaxors. Such a dynamic system can only be examined with atomic resolution imaging to an extent, therefore SAED and dark field imaging have been employed alongside dielectric spectroscopy to provide information on the dynamics and phase transitions as a function of temperature.

Finally, in chapter 5 the consequences of atomic resolution imaging on such systems described above (as well as other systems, e.g. III-V semiconductors) when combined with various strain analyses is discussed. Many strain measurement systems were developed before atomic resolution imaging was widespread and the extra information present in such images can affect any strain analysis. Focus is placed particularly on GPA and complications when using atomic resolution imaging are detailed and methods to avoid them are provided.

Chapter 2

Methods

2.1 Transmission electron microscopy

2.1.1 Conventional TEM

In conventional TEM, the sample is illuminated by a plane wave of electrons which are then transmitted though the sample before being projected onto a detector (charged-coupled device (CCD), phosphor screen etc.). Contrast is formed through two mechanisms: Amplitude contrast, where variations in specimen mass and/or thickness will alter the electron scattering, and phase contrast, where interactions in the sample alter the phase of the electron wave. For the relatively thick and heavy specimens studied in this thesis, interaction between the electrons and material need to be considered using dynamic scattering theories (e.g. Bloch waves) to approach the physical reality. Nevertheless, a useful description of the image formation in a microscope is the weak phase object approximation where the specimen only alters the phase of the electron wave (as is more closely modelled by thin specimens). Given an incident plane wave $\psi_{\text{in}} = 1$, the wave after passing through the sample (or exit plane wave), ψ_{ep}, is

$$\psi_{\text{ep}}(\boldsymbol{r}) = 1 - i\phi(\boldsymbol{r}). \tag{2.1}$$

where $\phi(\boldsymbol{r})$ is the object function that represents the phase shifts induced by the specimen [105]. This exit wave at the back focal plane is described by it's Fourier transform,

$$\psi_{\text{ep}}(\boldsymbol{q}) = \mathcal{F}[\psi_{\text{ep}}(\boldsymbol{r})], \tag{2.2}$$

where $\boldsymbol{q}$ is a reciprocal space vector and taking the square amplitude of $\psi_{\text{ep}}(\boldsymbol{q})$ gives the intensity in the measured diffraction pattern. The effect of the post specimen lenses and apertures is described by the transfer function, $t(\boldsymbol{r})$, such that the wave function at the image plane is given by the convolution,

$$\psi(\boldsymbol{r}) = \psi_{\text{ep}}(\boldsymbol{r}) \otimes t(\boldsymbol{r}) \tag{2.3}$$

and the actual intensity measured by a detector is

$$I(\boldsymbol{r}) = |\psi(\boldsymbol{r})|^2 \tag{2.4}$$

The transfer function usually consists of two parts, an objective aperture and the lens system. The objective aperture, t_{a}, is often modelled as a simple top-hat function

$$t_{\text{a}}(\boldsymbol{q}) = \begin{cases} 1 \text{ if } |\boldsymbol{q}| < |\boldsymbol{q}_a| \\ 0 \text{ otherwise} \end{cases} \tag{2.5}$$

where $|\boldsymbol{q}_a|$ is the radius of the aperture. Lens transmission, t_{l}, is expressed as

$$t_{\text{l}}(\boldsymbol{q}) = \exp\left[-\frac{2\pi i}{\lambda}\chi(\boldsymbol{q})\right] \tag{2.6}$$

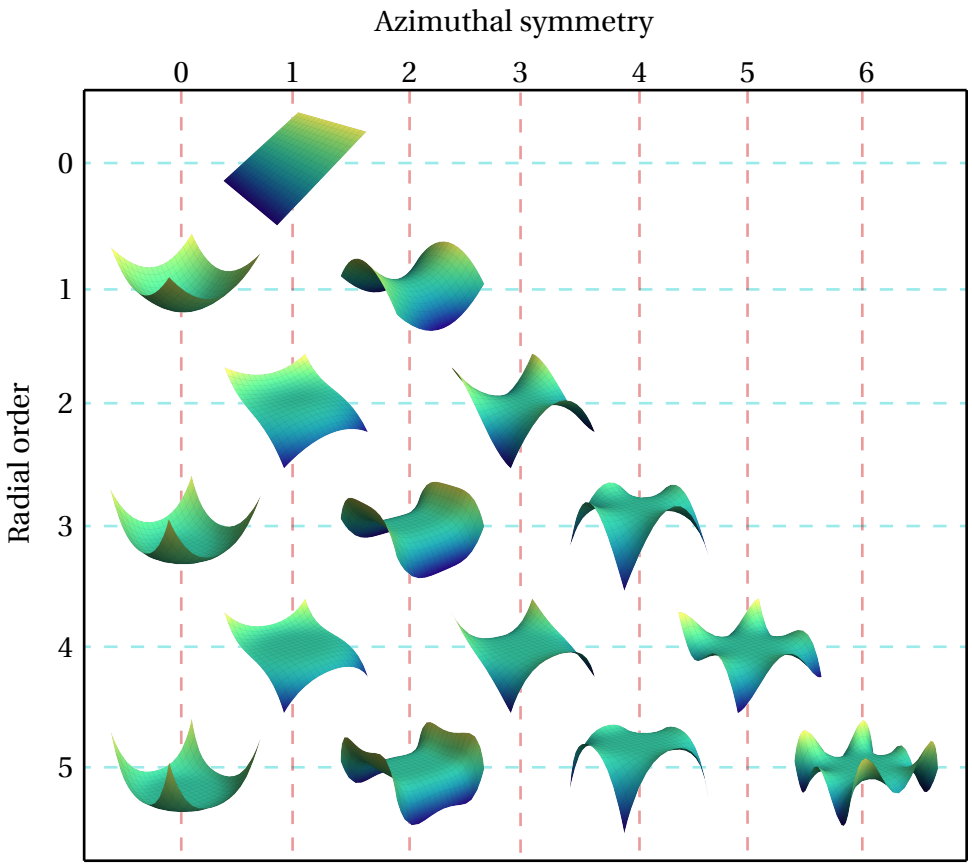

Figure 2.1: Surface plots of individual terms in the aberration function.

where λ is the (relativistic) wavelength and χ is the aberration function given by the expansion

$$\begin{aligned}\chi(\omega) = \text{Real}\Big[&\frac{1}{2}C_{1,0}\omega^{*}\omega + \frac{1}{2}C_{1,2}\omega^{*2} + \frac{1}{3}C_{2,1}\omega^{*2}\omega + \frac{1}{3}C_{2,3}\omega^{*3} + \\ &\frac{1}{4}C_{3,0}\omega^{*2}\omega^{2} + \frac{1}{4}C_{3,2}\omega^{*3}\omega + \frac{1}{4}C_{3,4}\omega^{*4} + \\ &\frac{1}{5}C_{4,1}\omega^{*3}\omega^{2} + \frac{1}{5}C_{4,4}\omega^{*4}\omega + \frac{1}{5}C_{4,5}\omega^{*5} + \\ &\frac{1}{6}C_{5,0}\omega^{*3}\omega^{3} + \frac{1}{6}C_{5,2}\omega^{*4}\omega^{2} + \frac{1}{6}C_{5,4}\omega^{*5}\omega + \frac{1}{6}C_{5,6}\omega^{*6} + \ldots\Big]\end{aligned} \tag{2.7}$$

where the complex angle, $\omega = \lambda(q_x + iq_y)$, has been substituted and ω^* is the complex conjugate [105]. $C_{m,n}$ are the aberrations where m and n here are the radial order and azimuthal symmetry. Each aberration term up to fifth order has been

plotted in figure 2.1. In uncorrected microscopes, it is the spherical aberration, $C_{3,0}$, that limits the resolution [5]. Typical aberration corrected microscopes only correct up to third order aberrations which is sufficient for atomic resolution imaging of Si dumbbells [106], this is discussed further in section 2.1.6.

In addition to the aperture and lens transfer functions, partial temporal and spatial coherence terms describe the imperfections in the electron source, i.e. non-point like and non monochromatic [107]. A discussion of these terms is outside the scope of this thesis and will not be discussed.

The ray diagram for conventional TEM is shown in Fig. 2.2(a) where the image plane (Eq. 2.1) and diffraction plane (Eq. 2.2) are shown. At the bottom of the column, a CCD camera is used in combination with a fluorescent screen to digitally capture the signal described by Eq. 2.4.

2.1.2 Selected area electron diffraction

If back focal plane is projected onto the detector, a SAED pattern is acquired. Electron diffraction has two key differences to the more prevalent X-ray diffraction. Firstly, the electron wavelength is much smaller then X-ray wavelengths meaning that the Ewald sphere in reciprocal space is much larger, or the surface is flatter. Secondly, the thinness of the sample means that each reciprocal lattice point is elongated in the direction of the beam. Therefore the Ewald sphere intersects more points and a greater number of spots can be seen (Fig. 2.2(g)). Whilst Bragg peaks cannot be measured as precisely as in X-ray diffraction (due to aberrations and distortions in post specimen optics), the large number of spots in one image does make SAED useful for quickly visualising structural changes, i.e. extra spots or spot splitting. In addition, diffraction patterns can be obtained from small and precise locations from the specimen.

One problem of electron diffraction is the dynamic range of detectors. To detect less intense spots/features a high acquisition time must be used, but this will

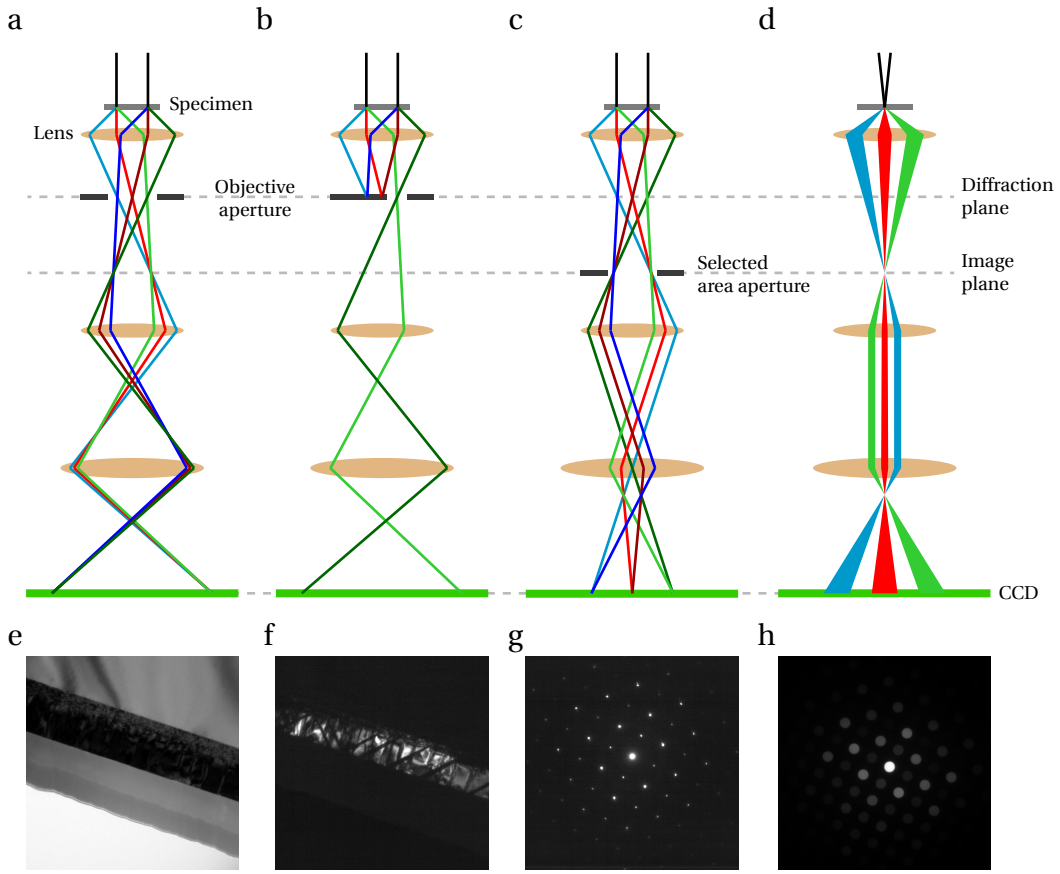

Figure 2.2: Ray paths of electrons in 4 modes of transmission electron microscope operation: (a) Imaging, (b) dark field, (c) diffraction and (d) convergent beam diffraction. (e)-(h) Example images taken from a $Pb(Zr\,Ti)O_3$ layer taken using the modes shown in (a)-(d) respectively.

cause bright features to be saturated. Conversely, a low acquisition time will reveal bright features without saturating, but weak features will have a low signal to noise ratio. To account for the limited dynamic range of the detector, a high dynamic range (HDR) image can be formed by acquiring several images with different acquisition times [108]. First taking a long exposure (typically minutes), the exposure is then reduced until the image is no longer saturated and the images can be stitched together to form a single image covering the whole dynamic range.

2.1.3 Diffraction contrast imaging

In conventional TEM imaging the beams diffracted by the sample are focussed on top of each other to provide phase contrast (Fig. 2.2(a)). However, using an objective aperture it is possible to allow only one diffracted beam through to form an image, shown in Fig. 2.2(b). This image will produce a map of where the diffraction is stronger/weaker at the reciprocal vectors selected by the aperture, for example if two crystal structures are present it may be possible to map each structure if they diffract differently or to visualise defects [109]. In a similar fashion, a displacive ferroelectric may scatter the electrons differently for different polarisation directions and dark field can be used to visualise the domains. For example, Fig. 2.2(g) shows dark stripes at 45° to a film of PZT (bright) that correspond to ferroelectric domains with the polarisation oriented at 90° to the rest of the film. This provides an easy way to visualise structural changes in real time, limited by the electron signal and the efficiency of the CCD camera.

2.1.4 Digital large angle convergent beam electron diffraction

If the incident beam is converged onto a single point on the specimen, a convergent beam electron diffraction (CBED) pattern is formed at the back focal plane (Fig. 2.3(a)). Instead of individual spots of a conventional diffraction pattern, there are now discs (corresponding to the range of incident momenta). Inside each disc

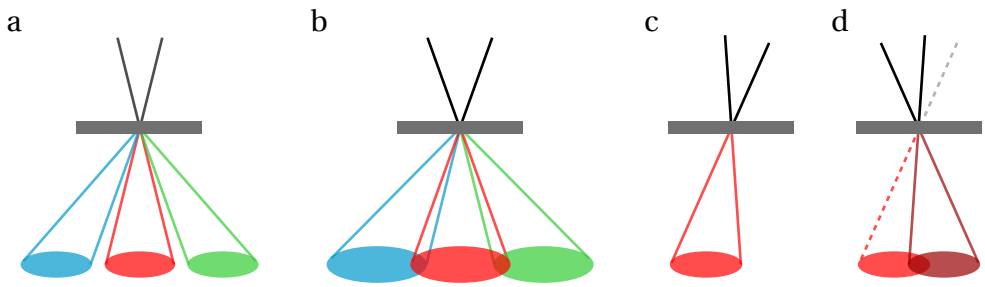

Figure 2.3: (a) Example of convergent beam electron diffraction simplified to only 3 discs. (b) Demonstration of the overlap between separate discs when the convergence angle is increased. Considering only one disc, (c), a larger disc can effectively be formed using the same convergence angle as in (a) but by scanning the beam tilt, (d).

is a wealth of extra features from dynamical scattering, usually used to determine the symmetry of the crystal. However, the field of view of each disc is limited by the convergence angle (defined by the condenser system) and small tilts can easily obscure a CBED pattern's symmetry. An obvious solution would be to increase the condenser aperture size to create a large angle convergent beam electron diffraction (LACBED) pattern [110], but quite quickly the LACBED discs will start to overlap and the information cannot be easily separated (Fig. 2.3(b)). It is possible to select only one LACBED reflection by moving the beam cross over position below the specimen and then using an aperture. However this is time consuming and the area the pattern is obtained from is large due to the beam crossover.

Beanland *et al.* [111] developed a new technique to form a LACBED pattern by taking multiple CBED patterns from different incident beam tilts. Instead of expanding the incoming probe angle, a smaller angle can be used so that the CBED spots do not overlap, but the beam is rastered in tilt to cover the same angle range (Figs. 2.3(c) and 2.3(d)). Since the individual CBED spots do not overlap, they can be separated and stitched together to form the LACBED pattern. Leveraging computer control to automate the acquisition of multiple CBED patterns and the processing, a full LACBED pattern can be obtained in $\sim$5 minutes. An experimental example of a digital large angle convergent beam electron diffraction (D-LACBED)

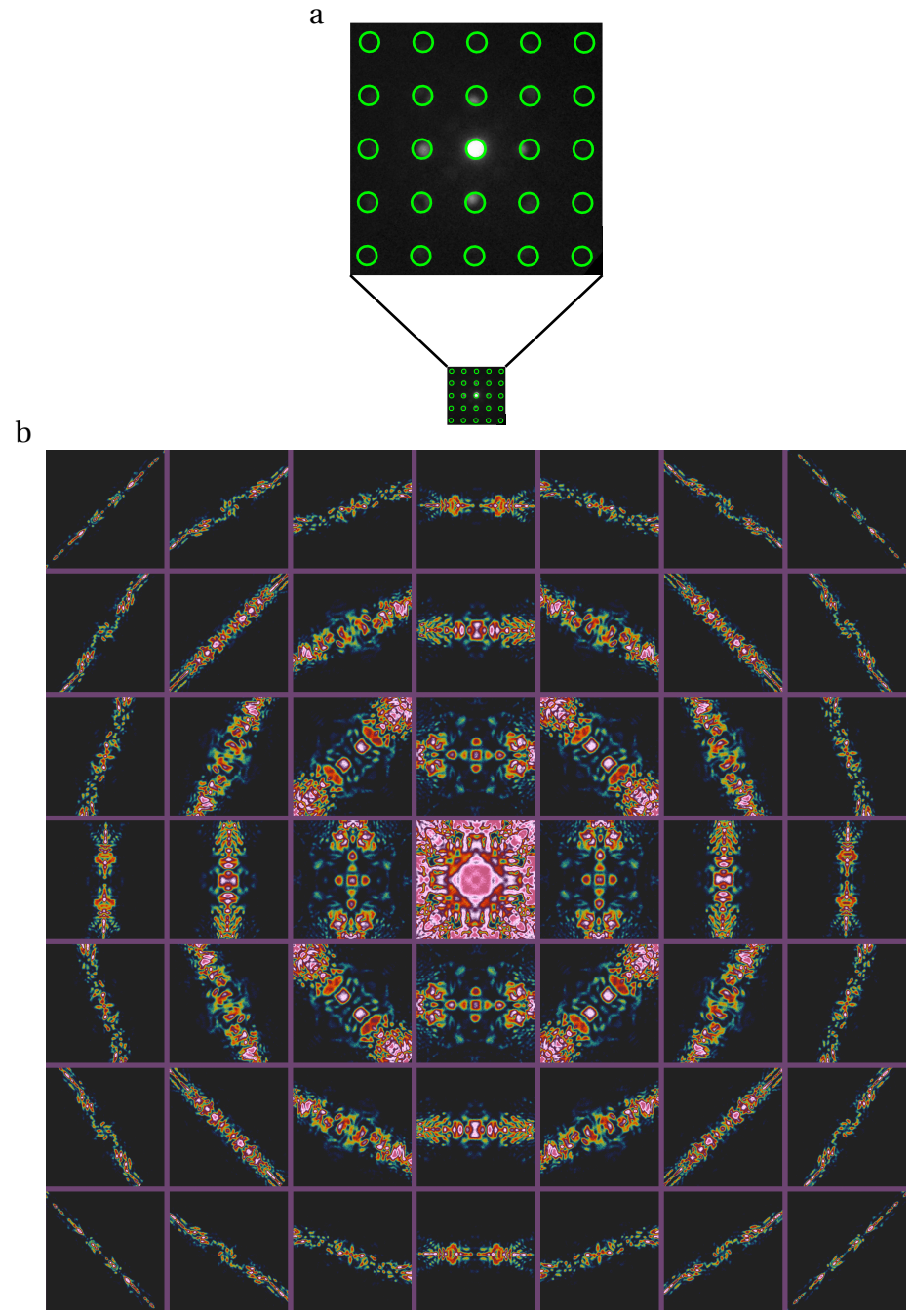

Figure 2.4: (a) Conventional convergent beam electron diffraction pattern acquired from $SrTiO_3$. The diffraction disks are highlighted with green circles. (b) Digital large angle convergent beam electron diffraction pattern acquired from the same area as (a) showing the full information in the diffraction pattern. A scaled version of (a) is shown for direct comparison to (b).

pattern is shown in Fig. 2.4 with comparison to an equivalent CBED pattern.

2.1.5 Scanning transmission electron microscopy

A commonly used tool in the microscopist's arsenal is the scanning transmission electron microscope (STEM). This mode of operation requires the beam to be condensed down to a point, much the same as in CBED though the discs overlap (as in Fig. 2.3(b)), and rastered across the sample. At each point on the sample, the intensity of the electrons is collected at various scattering angles to form images. The most common imaging modes are annular dark field (ADF), collecting at high scattering angles and bright field (BF) (as well as annular bright field (ABF)) that collect at low angles (see Fig. 2.5), these will be discussed later. One of the strengths of STEM is that many signals may be acquired at once, including a range of spectroscopic signals such as map X-rays and electron loss. Due to the serial, scanning beam, the resolution of STEM in principle depends on the probe size formed. The probe shape is given by a Bessel function (Fig. 2.6), where the probe size is defined as the width of the central disc. Diffraction effects give a source radius, r_{d} as

$$r_{\mathrm{d}} = \frac{0.61\lambda}{\alpha} \tag{2.8}$$

where α is the beam semi-convergence angle (or the condenser aperture radius), shown in Fig. 2.5, and λ is the electron wavelength. In addition, aberrations must also be considered, giving a source size, r_{a}, as

$$r_{\mathrm{a}} = A_{\mathrm{n}} C_{\mathrm{n},0} \alpha^{\mathrm{n}} \tag{2.9}$$

where n is the radial order of the aberration term, $C_{\mathrm{n},0}$ are the aberration coefficients and A_{n} are factors that account for that fact that the smallest probe diameter due to each aberration are not at the image plane. Non-rotationally symmetric aberrations have been ignores here for simplicity and, additionally, chromatic aberration

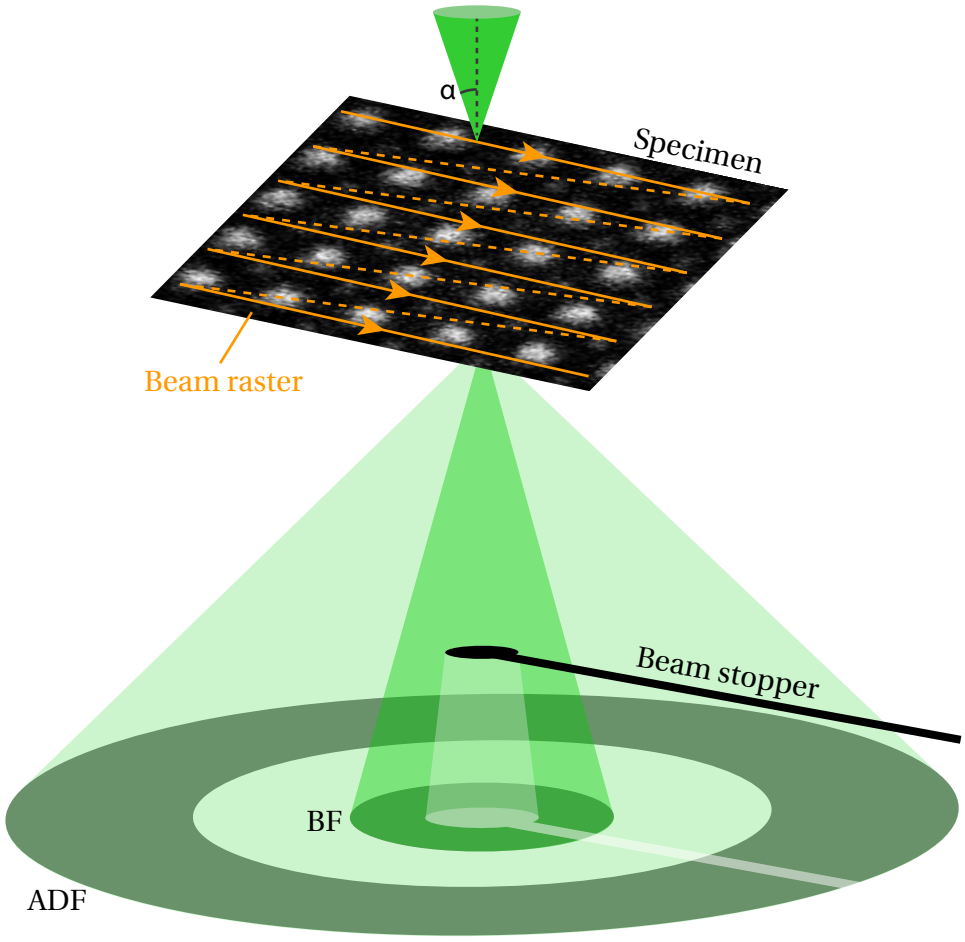

Figure 2.5: Schematic of scanning transmission electron microscope measurements showing the convergent beam being rastered across the sample and the scattered electrons being collected by various detectors, annular dark field (ADF), bright field (BF) and annular bright field (ABF). ABF is demonstrated here by using a beam stopper to block the centre portion of the BF detector.

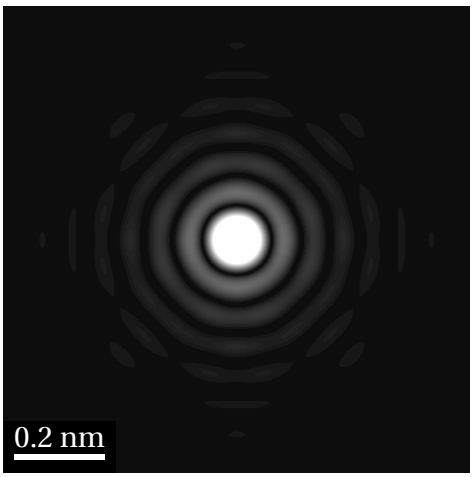

Figure 2.6: (a) Example simulated scanning transmission electron microscope probe formed with minimal aberrations and a condenser aperture of 20 mrad. The image gamma has been adjusted for clarity.

is included for n $= 1$ and A_1 is $\frac{\Delta E}{E_0}$, where E_0 is the source energy and ΔE is its energy spread. Finally, the finite source size must be considered, giving a probe size, r_s, of

$$r_\mathrm{s} = \frac{1}{\pi\alpha}\sqrt{\frac{IM}{B}} \tag{2.10}$$

where, I is the probe current, B is the source brightness and M is the source magnification [112]. The total probe radius can be calculated by adding the individual terms in quadrature. It should be noted that the diffraction limiting term, Eq. 2.8, and the source size term, Eq. 2.10, give a smaller probe size for larger condenser apertures. However, the aberration term, Eq. 2.9, acts in an opposite manner and, at a certain point, the aberrations will start increasing the probe size. As higher order aberrations are corrected, the aperture can be made larger and will decrease the probe size, as indicated in Fig. 2.7.

However, resolution is also limited by imperfections in the scanning system, where the beam position does not perfectly correspond to the pixel grid of the image. In addition, as the acquisition for each pixel is not in parallel, any drift of the specimen will produce distortions in the resulting image. Most of the specimen

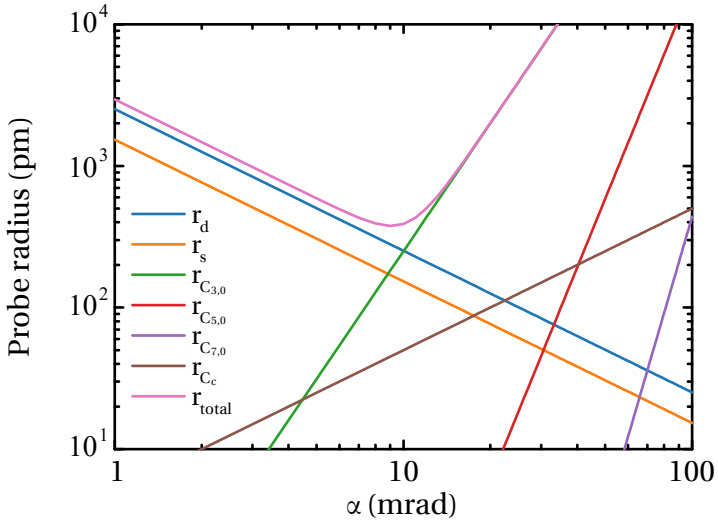

Figure 2.7: (a) Plot of the scanning transmission electron microscope probe radius terms for varying condenser aperture/convergence angle. It can be seen that the total probe radius, r_{total}, is limited by the spherical aberrations here. Values used are $E_0 = 200$ keV, $\Delta E = 1$ eV, $M = 4 \times 10^{-9}$ and $C_{3,0} = C_{5,0} = C_{7,0} = C_C = 1$ mm.

drift can be removed by simply waiting for the sample to stabilise, though there will always be some drift due to the microscope or holder design as well as thermal expansion. Likewise, the scan imperfections depends on the design and construction of the microscope and there it is not possible to easily correct. To circumvent specimen drift, rapid scans can be performed were the total displacement across the whole image is reduced. However, this drastically reduced the signal so multiple scans are acquired and combined later, also having the effect of averaging out the scan imperfections [113]. This is performed here using simple cross correlations between successive images, with parabola fitting to obtain sub-pixel accuracy shifts.

The most common imaging detector is an ADF detector that is a ring centred on the optic axis (see Fig. 2.5), typically at ~ 50 to ~ 150 mrad (typical semi angles of the incident beam are < 30 mrad) [114–116]. Because of the large detector, ADF imaging can be described as incoherent and is therefore insensitive to phase information. This can be qualitatively explained by considering scattering

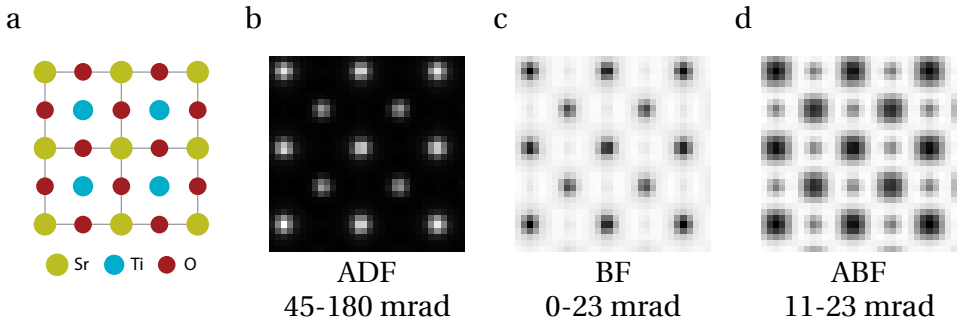

Figure 2.8: (a) Example structure consisting of 2×2 unit cells of $SrTiO_3$. (b-d) Annular dark field (ADF), bright field (BF) and annular bright field (ABF) simulations of the structure in (a), respectively. An incident beam convergence angle of 20 mrad was used, collection angles are shown below the images.

from two individual atoms. Due to the coherent source, a set of Young's interference fringes is formed and, for a large detector, the signal is averaged over many fringes. Therefore, any phase information, that would change the phase of the fringes is averaged out [112, 115]. The images produced (Fig. 2.8(b)) are therefore intuitive in general; regions with higher signal/intensity correspond to the position of atoms whereas vacuum corresponds to no signal (due to the lack of scattering). Though the theory needed to properly describe the scattering relies on thermal diffuse scattering (TDS) (i.e. from phonons), the scattered intensity is approximately proportional to Z^2, where Z is the atomic number atom column [115, 117]. This Z-contrast imaging is much stronger than in conventional TEM imaging and provides a useful aid to analysing elemental composition. Note that the exponent proportionality Z^2 is not exact and, depending on the collection angles of the detector, may be as low as $Z^{1.5}$ [115]. In this thesis, no quantitative intensity measurements are made so the relation Z^2 will be used (as is the case for Rutherford scattering at high collection angles) for simplicity.

The main alternative imaging mode is BF where a circular detector, with approximately the same collection range as the incoming probe angle ($\lesssim 30$ mrad), is placed on the beam axis (see Fig. 2.5). The immediate difference to ADF is that the image contrast is inverted (see Fig. 2.8(c)). However, as the diffracted

beams overlap, phase differences between the different beams will provide phase contrast (the same as in conventional TEM) and considering only two beams, will form fringes corresponding to the atom planes. Because the fringes are on the order of the BF detector size, this phase contrast is present in the images; this is contrary to ADF where the large detector averages over many fringes. An extension of BF is ABF, where the centre region (< 10 mrad) of the BF signal is not collected (usually by insertion of a beam stopper as shown in Fig. 2.5) [118–121]. This imaging condition allows for imaging of very light atoms (i.e. carbon and oxygen), shown in Fig. 2.8(d), that would normally only provide very weak contrast. This relies on the fact that at the lower angles, the phase contrast is destructive, and any phase shifts can only increase constructive interference while at the outer angles ($\sim 10 - 20$ mrad) the opposite is true [119]. As a BF-STEM image has lower intensity for atom columns and higher intensity for vacuum, selecting only the destructive interference in the outer BF region enhances the contrast.

2.1.6 Aberration correction

In order to remove any aberrations in the microscopes illumination system, first they must be measured. The most common method, and the one used here, is the Zemlin-tableau method. Although it was originally developed to minimise axial coma in conventional TEM, it has since evolved to determine all aberrations to be removed for a aberration corrected study. The core principle relies on the fact that the effects of the aberrations increase as a function of beam tilt and the contrast transfer function will alter. This can be easily measured by imaging an amorphous specimen and calculating the diffractograms (i.e. the FFT of the real space image) for each tilt. Figure 2.9(a) shows a typical diffractogram showing the central Airy disk and the outer, concentric Thon rings. From this single diffractogram, the defocus $C_{1,0}$ can be measured as the spacing of the rings and twofold astigmatism as the ellipticity (figure 2.9(b)). To measure other aberrations, a series of diffractograms is

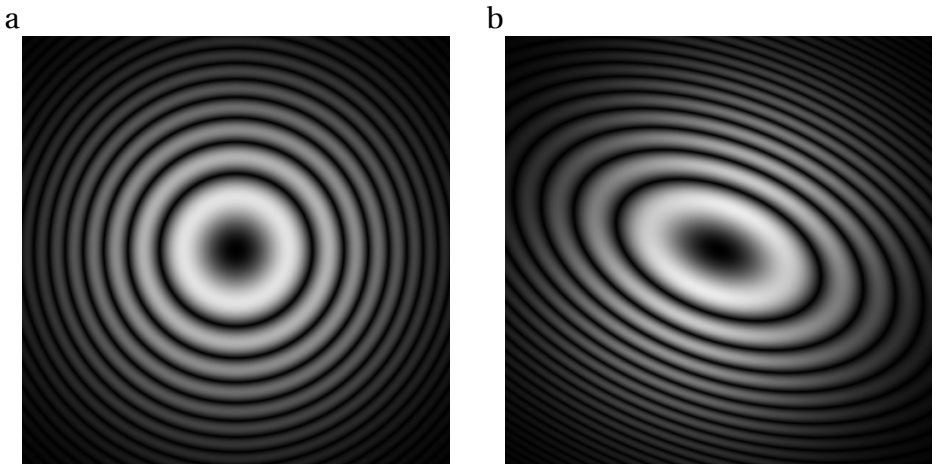

Figure 2.9: (a) Diffractogram with focus as the only aberration. (b) Diffractogram with introduced astigmatism.

Table 2.1: Typical experimental aberration values after correction.

Aberration	Notation	Value
Twofold astigmatism	$C_{1,2}$	< 1 nm
Second-order axial coma	$C_{2,1}$	< 30 nm
Threefold astigmatism	$C_{2,3}$	< 20 nm
Third-order spherical aberration	$C_{3,0}$	< 1 μm
Third-order star aberration	$C_{3,2}$	< 1 μm
Fourfold astigmatism	$C_{3,4}$	< 1 μm

collected at varying beam tilts and azimuthal angles, called a Zemlin tableau [105, 122], where the effective defocus and twofold astigmatism are measured to build a map of how the aberrations distort the electron wavefront. Figure 2.10 demonstrates this process, where the aberrations can be clearly seen at higher tilt angles.

The process for STEM/probe correction is slightly different though relies on similar principles. First a reference image under no tilt is obtained close to focus, followed by a series of micrographs at various tilts and both underfocus and overfocus. These different focus images can be compared to the reference image to obtain the effective defocus and twofold astigmatism [105, 114]. Typical values of aberrations after correction are shown in table 2.1.

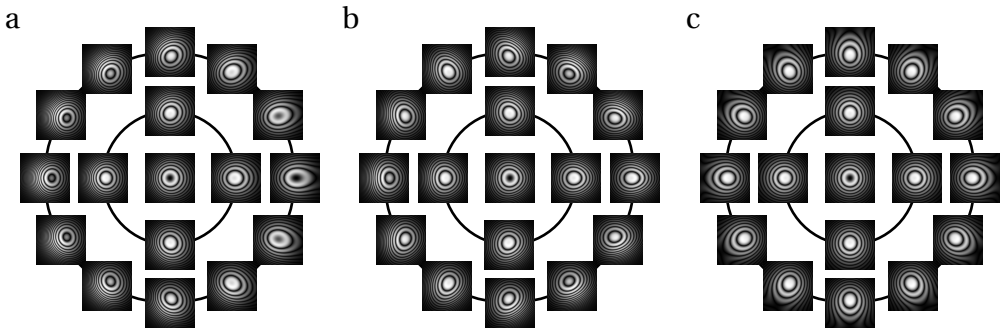

Figure 2.10: Simulated Zemlin tableaux showing (a) coma, (b) threefold astigmatism, (c) spherical aberration. The position from the centre indicates the polar angle of the tilt, and the position around the circles indicates the azimuthal tilt angle.

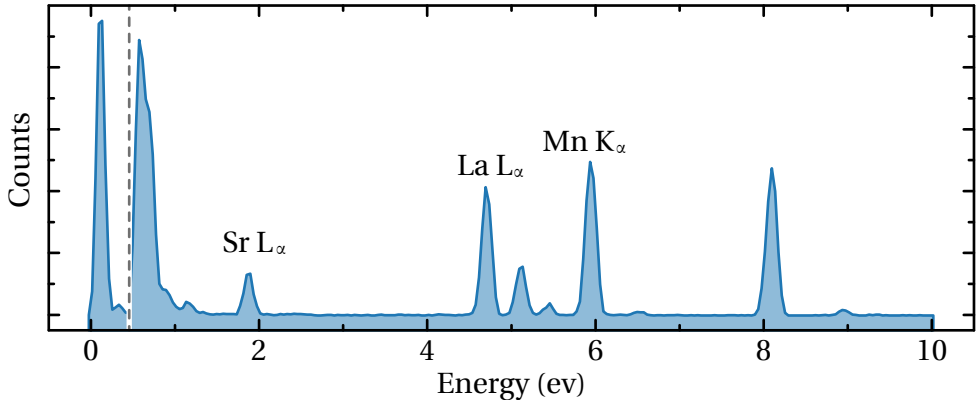

Figure 2.11: Example energy dispersive X-ray spectroscopy spectrum from $(La_{0.7}Sr_{0.3})MnO_3$ with some of the characteristic peaks labelled. The region to the right of the dashed line has been scaled by 10.

2.1.7 X-ray spectroscopy

When the electron beam hits the specimen, various excitations are produced. If an incoming electron ejects an inner shell electron from an atom, the outer electrons will relax inwards to fill the hole left. When these electrons relax they can give off X-rays with an energy characteristic of the element of the atom. This phenomenon is exploited in energy dispersive X-ray spectroscopy (EDX) to perform elemental identification inside the TEM, where X-rays are detected by a silicon drift detector. An example spectrum is shown in Fig. 2.11 where the characteristic peaks can be seen at different energies. Combing this with STEM allows the collection of a

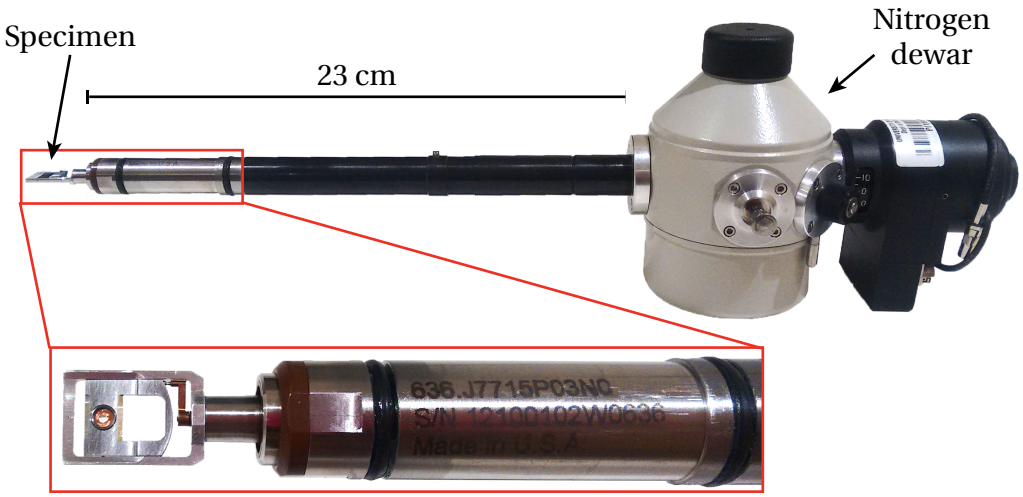

Figure 2.12: The cooling holder demonstrating the configuration of the sample and the liquid nitrogen dewar.

spectrum at every probe position, which can then provide a 2D map of the elemental composition, even at the atomic scale [13].

2.1.8 In-situ TEM cooling

In order to study temperature related phase changes inside the TEM, a specially designed specimen holder needs to be used. In this work a Gatan 636 cooling holder was used, shown in Fig. 2.12. The specimen is cooled via a liquid nitrogen dewar at the external end. The dewar is connected to the specimen via a copper heat transfer rod. Temperatures in the region of 120 K were attainable, with a temperature accuracy of ± 1 K. Temperature values are controlled by using an electrical heater on the transfer rod between the dewar and specimen. Heat transfer from the actual specimen needs to be considered, for example, if the specimen is suspended on a lacy carbon film, the heat transfer will be limited. To aid in heat transfer and obtain accurate temperature measurements, any in-situ cooling experiments were performed with samples embedded in aluminium.

2.1.9 Specimen preparation

To use TEM to study materials, first the samples must be made electron transparent (< 100 nm). Several techniques have been employed here.

First, focussed ion beam (FIB) has been utilised to prepare specimens at specific sites [123]. Gallium ion beams are used to extract a small (~ 5 μm) lamella from the surface of the samples. To protect the surfaces of the samples, a carbon layer is deposited on top with the ion beam. For surface sensitive samples (see Chapter 3), the protective carbon layer is deposited using a scanning electron microscopy (SEM) beam first. After attaching the sample to a grid, the sample is thinned to electron transparency using the ion beam (here Ga ions accelerated at 30 kV) at an incident angle of 1.5° to the surface. To reduce damage and redeposition, the accelerating voltage of the ion beam is lowered as the sample gets thinner, final polishing is performed at an accelerating voltage of 5 kV. In this work there are no samples containing Ga, so implantation from the ion source is easily detectable.

Conventional specimen were also made via mechanical methods [124]. This involves thinning down a sample via polishing the sample with lapping papers, or crushing the sample to a powder. Then, the specimen is thinned to electron transparency using a Gatan precision ion polishing system (PIPS) using argon ions accelerated at 5-6 kV at incident angles of 3° and 4° (the higher angle to avoid milling the copper TEM grid). To remove redeposition and surface damage, final thinning was performed using 3 kV. For samples used for in-situ TEM cooling experiments, the sample was crushed and mixed with aluminium powder, encased in aluminium foil and then cold rolled/compressed. The sample was then mechanically thinned then ion milled using the PIPS, as before.

2.1.10 Microscopes

In this thesis, two TEMs have been used. First, an uncorrected JEOL 2100 fitted with a LaB_6 source operated at an accelerating voltage of 200 kV and using a Gatan Orius CCD. Second, a JEOL ARM-200F (ARM) with a Schottky field emission gun operated at 200 kV and fitted with CEOS probe and image correctors (up to third order). The ARM uses JEOL ADF and BF detectors and an Oxford Instruments X-Max^N 100TLE detector is fitted for EDX measurements. The FIB used to prepare samples was a JEOL 4500 dual beam FIB and SEM.

All low magnification work was performed on the 2100 system, including SAED, D-LACBED and dark field imaging. The ARM was used for all atomic resolution STEM imaging and EDX.

2.2 Strain measurements from atomic resolution images

The strain measurements described in section 1.5.1 (and used in chapter 5) rely heavily on the selection of a reference lattice that is considered as the zero strain case. The obvious method is to define a vector in real space, perhaps averaging over multiple vectors to improve accuracy. This does not produce accurate results as noise and small deviations can affect the basis selection. Even if the basis vector is averaged, images often do not include enough strain free area to average over more than a few vectors. Instead, a Bragg spot in the image FFT can be used to define the lattice spacing. This is not directly accurate, but can be refined through the use of the phase image defined by Eq. 1.8. After the initial measurement of the reference vector, an area is selected that is of constant strain. Using multilinear regression, the gradients of the phase image within the defined area can be calculated. This corresponds to a deviation from the $\boldsymbol{g}$ vector given by

$$\nabla P_{\mathrm{g}}\left(\boldsymbol{r}\right) = 2\pi\Delta\boldsymbol{g}, \tag{2.11}$$

from which the previously defined $\boldsymbol{g}$ vector can be corrected [101]. This method used for both basis vectors as long as the same area is used for refining.

2.3 Image simulation

An important component of experimental TEM is being able to simulate images for comparison to real experimental results and ensure the images are being interpreted in the correct way. Simulations are performed using the multislice method [107], where atomic potentials are calculated from the crystal structure and separated into slice. The input electron wave is propagated through the first slice, and the exit wave of this slice is used as an input wave to the next slice. To perform TEM or STEM simulations, the initial wave function is set as a plane wave or a probe, respectively.

For STEM a full multislice simulation needs to be performed for each pixel, and the final exit wave is summed over a defined detector area. In addition, STEM simulations need to account for TDS [125, 126]. This is performed by simulating each pixel multiple times. With each iteration a small, random displacement is applied to every atom, where the displacement is given by a mean square displacement depending on the crystal. All simulations in this thesis where performed using in-house developed software using graphics processing unit acceleration.

2.4 Dielectric spectroscopy

In the study of polar materials, it is useful to examine the response to applied electric fields. In dielectric spectroscopy, an alternating field is applied at various frequencies using an impedance analyser. As the field is applied, the resistance and capacitance is measured. This can be converted to the complex permittivity, ε, where

$$\varepsilon = \varepsilon' - i\varepsilon'' \tag{2.12}$$

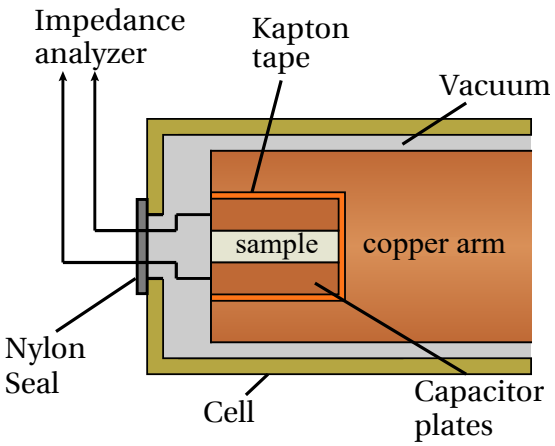

Figure 2.13: The experimental configuration for dielectric measurements. Cooling and heating are performed through the copper arm.

where the real and imaginary components are defined as

$$\varepsilon' = \frac{C}{C_0} \tag{2.13a}$$

$$\varepsilon'' = \frac{1}{RC_0\omega} \tag{2.13b}$$

where C and R are the measured capacitance and resistance, C_0 is the vacuum capacitance of the system and ω is the angular frequency of the field [127]. The real component can be used to describe the energy stored in the system and the imaginary part related to the energy loss. As such, dielectric spectroscopy is a useful tool for studying phase changes in materials. For example, if a material changes structure, the electric susceptibility may also change, and there will be a large dielectric loss as well as a change in the real component of the permittivity.

To study phase changes, the temperature needs to be controlled, the experimental set up is shown in Fig. 2.13. Here the sample is placed in between the capacitor plates ($\sim$ 1 mm apart), which is then held in a slot in a copper rod (insulated with Kapton tape). Inside the copper rod a liquid nitrogen source cools the sample whilst an electric heating element is used by an Oxford Instruments ITC503S to control the temperature to a precision of 0.1 K above 200 K and 0.01 K below

200 K. Electrical measurements were made with an HP 4192A impedance analyser, capable of applying an electric field frequency of 5 Hz to 13 MHz (though Eqs. 2.13 are only valid to 10 MHz [127]). To avoid ice build up, the whole sample and heating rod system is kept in vacuum.

2.5 Device growth

An important influence on the functionality of a device is the quality of the growth of the structures. Two main methods have been used for growth of the devices examined in this thesis.

2.5.1 Pulsed laser deposition

For the FTJ devices described in 1.2.2, the thickness and uniformity of the ferroelectric layer need to be precisely controlled. PLD is a physical vapour deposition technique that has been successfully employed for growth of ultrathin, complex oxide thin films [128, 129]. A target of the desired material and stoichiometry is placed opposite a substrate and in vacuum ($\sim 10^{-6}$ mbar), though gases are often added to control partial pressure or stoichiometry (e.g. by adding oxygen). A high powered ultraviolet laser pulse ($10 - 50$ ns) then strikes the target, ablating it into a plasma plume that deposits onto the substrate. Three main growth modes are observed, depending on surface mobility of the ions and lattice mismatch: layer-by-layer (Frank-van der Merwe), island (Volmer-Weber) and combined island and layer growth (Stranski-Krastanov) [129]. Many parameters can be controlled (laser energy density, pulse time, gas pressures, substrate temperature, etc.) to optimise the growth as desired. To aid in film growth, reflection high energy electron diffraction is used in-situ to monitor film thickness [129].

2.5.2 Sputtering

Metal electrodes for FTJs are formed using magnetron sputtering. Here, a cathode target is irradiated with energetic cations (Ar^+) that are confined with electric and magnetic fields. The cations eject parts of the target (individual atoms or larger clusters) towards an anode substrate where the material is deposited. This can later be patterned using photolithography to form individual contacts.

Chapter 3

Atomic scale study of ferroelectricity in $PbTiO_3$ ultrathin films

3.1 Introduction

The discovery of ferroelectricity in films as thin as 3 unit cells (~ 1.2 nm) [14], combined with the desire for ever smaller devices, has created great interest in ferroelectric based devices. A promising device structure is the FTJ, where two conducting electrodes encompass an insulating, ferroelectric layer thin enough for a current to tunnel between the electrodes (see section 1.2.2). By switching the polarisation of the ferroelectric, the tunnel current can be modulated by $> 10^4$ % [130–132], forming binary states, or one bit in computational terms. Because the polarisation is intrinsic to the ferroelectric layer, the devices are non-volatile and maintain their state. The principles of such an FTJ are therefore very similar to a MTJ where the a tunnel current is modulated by aligned/unaligned magnetic fields in the electrodes. As such, it is possible to combine both phenomena by using ferromagnetic electrodes with a ferroelectric insulating layer. This forms a MFTJ, a four-state device

comprising of two ferroelectric and two ferromagnetic states. Whilst ferroelectricity is present down to 3 unit cells of thickness, it is counterproductive to have a device small in one dimension if the remaining dimensions cannot be similarly small. In the case of ferroelectric thin films, the in-plane density depends on the ability to have two different polarisation directions next to each other. The configurations available then depend on the size of the domains and the domain walls separating them. Fortunately, the domain widths follow the Kittel law and thus by making the films thin, the domain sizes are also decreased [58, 133].

Ideally, Kittel type domains would be preferred with abrupt domain walls, but, as the thickness of the film is reduced and the depolarisation field is increased, it is predicted that the domain walls become more complex, involving Landau-Lifshitz flux closure regions and even vortices. However, it is unclear how the domains are configured when in the presence of conductive electrodes (as are necessary to apply electric fields to manipulate the polarisation) that will screen the depolarising field (see section 1.2.2). As the ferroelectric phenomenon in perovskites is a result of atom displacements that can change from unit cell to unit cell, aberration corrected TEM is a perfect tool for studying such systems and how exactly the polarisation changes between domains.

3.2 Multiferroic tunnel junctions

The devices consist of an $SrTiO_3$ (STO) substrate with 24 nm of $(La_{0.7}Sr_{0.3})MnO_3$ (LSMO) (that is half-metallic) acting as the first electrode. On top of this PTO films of 1.2, 2.4 or 3.6 nm were deposited as the dielectric barrier. Both oxide layers were deposited using reflection high energy electron diffraction assisted pulsed laser deposition. The second electrode was formed by sputtering ~ 30 nm of polycrystalline Co on top of the PTO and then patterning 40×40 μm contacts using photolithography. Figure 3.1(a) shows an example device structure where the growth can be

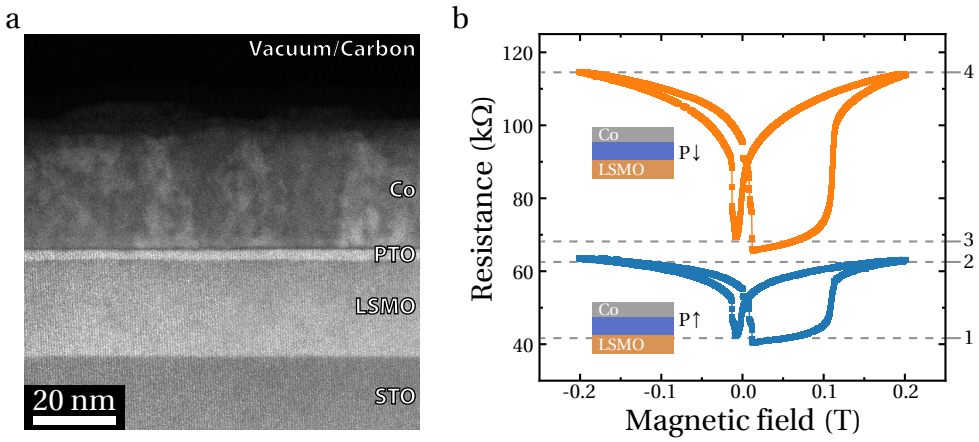

Figure 3.1: (a) Annular dark field image of a multiferroic tunnel junction where the $PbTiO_3$ (PTO) barrier thickness is 2.4 nm between the Co and $(La_{0.7}Sr_{0.3})MnO_3$ (LSMO) electrodes. The whole device is grown on a $SrTiO_3$ (STO) substrate. (b) Corresponding tunnelling magnetoresistance loops for both polarisation towards Co (blue circles) and towards $(La_{0.7}Sr_{0.3})MnO_3$ (LSMO) (orange squares). Resistance was measured at a 0.2 V bias after cooling 10 K in a -0.8 T magnetic field. The 4 resistance states have been highlighted by the dashed grey lines.

seen to be defect free apart from the interface between PTO and Co. Figure 3.1(b) gives the electrical properties, showing the MFTJ to be functional. Depending on the combination of polarisation direction and magnetic field, 4 resistance states are clearly visible with a tunnelling electroresistance (TER) effect of ~ 81 % and a tunnelling magnetoresistance (TMR) effect of ~ 90 % (measurements were performed after cooling the samples to 10 K in a -0.8 T magnetic field).

3.3 Quantitative measurements from transmission electron microscopy images

3.3.1 Atom displacement measurements

As discussed in section 1.3.2, the polarisation in ferroelectrics such as PTO depends on the relative displacement of the atoms within each unit cell. With the aid of modern computer processing, the task of finding the peaks and measuring the dis-

placements is made relatively quick (a few seconds). The basis of the technique borrows heavily from the PP method of measuring strain (section 1.5.2) [102]. After acquisition of the atomic resolution image, the local maxima (or minima, depending on imaging mode) are found by comparing each pixel value to the values of the surrounding 8 pixels. Depending on the image quality, it may be necessary to apply a filter to remove noise that could be erroneously detected as atom positions. In this work, where peak positions are typically separated by $\gtrsim 20$ pixels, a median filter with a square window with sides of 3 pixels was used to remove noise outliers, this was followed by convolution with a Gaussian ($\sigma = 1$ pixel) to restore smooth edges.

Once the initial peaks have been measured, the positions can be refined using a number of fitting methods. Three main position refinement methods are considered here: Interpolation, parabola fitting and Gaussian fitting. Bicubic interpolation [134] is used to effectively estimate data to form a higher resolution image and performs well if the image is sufficiently noise free or the image has been smoothed. For this reason this technique has not been favoured, though it finds its use as a quick and robust method for initial examinations. Both parabola fitting and Gaussian fitting are more robust to noise, and can be performed on the original data using the initial positions measured from the filtered image. Parabola fitting involves the fitting of two parabolae (using least squares [135]), one in both the x and y directions, and using the maxima to determine the peak centre. For the Gaussian fitting, full 2D Gaussians were fitted using non-linear least squares [136]. Whilst this is a more accurate technique than parabola fitting, it requires a larger fit area to converge and therefore a higher magnification image. On the other hand, parabola fitting can be employed on an area only 3×3 pixels in size. As such, Gaussian fitting often fails and the work here uses Gaussian fitting where possible, and parabola fitting otherwise.

Once all of the atom column positions have been measured, the columns need to be identified and separated into their own sublattices. By manually defining

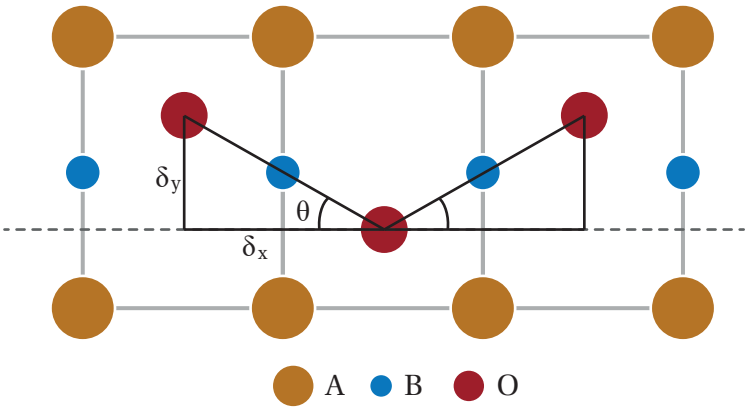

Figure 3.2: Schematic of a tilted ABO_3 perovskite $\langle 110 \rangle$ showing how the octahedral tilting is measured.

basis vectors for the unit cell and an initial position on each sublattice, the sublattices can be calculated using an iterative procedure. The procedure starts with the user defined initial positions, then the defined basis vectors are added/subtracted to this position and the nearest (within a defined threshold) peak is added to the sublattice. These new positions then form the initial positions for the next iteration until all the peaks have been added to a sublattice. As with PP, this is performed in affine space so the Euclidean distance can be used when searching for a peak's corresponding pair [102].

This method is very robust as long as there is no considerable strain or any defects that cause the expected positions of one sublattice to overlap with another (as would be the case in Ruddlesden-Popper defects or an anti phase boundary (APB)). Once the positions of all the sublattices are known, it is simple to calculate the relative displacements by, for example, taking each position in one sublattice and finding the average position of the nearest 4 neighbours from another sublattice and calculating the difference.

3.3.2 Octahedral tilt measurements

In perovskite crystals, the tilting of the oxygen octahedra can play a major role in the crystal's properties, for example octahedral tilting is often antithetical to ferroelectric displacements [63]. With the use of ABF imaging and the possibility to accurately measure the oxygen positions, it is possible to measure any octahedral tilt visible in the image and relate this to the functional properties of the material.

It is important to remember that the tilt may not always be measurable using TEM, depending on the crystal zone axis and tilt system. Using the Glazer notation [66] and assuming a $\langle 100 \rangle$ zone axis, only a^+ rotations will be visible as the out of phase rotations will overlap in the image projection. On the other hand a rhombohedral crystal with the $a^-a^-a^-$ tilt system (as found in LSMO) will have two distinct pseudocubic $\langle 110 \rangle$ projections, one where the tilted oxygen atoms align to a (relatively) well defined column, and a second where the oxygen positions are displaced within one column.

Figure 3.2 shows how the octahedral tilt is measured in a $\langle 110 \rangle$ projection. To simplify the measurement, only the oxygen positions are required and it is the relative distances, δ_{x} and δ_{y}, that need to be measured. These two distances form a right angle triangle from which it is trivial to calculate the projected tilt angle, θ. Because each oxygen column has two nearest neighbour oxygen columns, the tilt for each position is calculated as the average of the angles between both neighbours. Additionally, some experimental images have a small amount of rotation or skew that can easily be corrected as this simply adds a constant to the angles which is trivial to calculate and remove.

All the measurements made here use the (pseudocubic) $\langle 110 \rangle$ projections and therefore the directly measured angles are not the real tilt about the $\langle 100 \rangle$ axes, as used in the Glazer notation. The latter can be calculated by converting δ_{x} to the corresponding $\frac{1}{2}\,[100]$ distance.

3.3.3 Accuracy of position measurements

Whilst atomic resolution STEM imaging is routine with current aberration correctors, the complicated nature of electron interactions in the specimen raises questions about whether the peak/trough that is interpreted as an atom column is actually the true position. An obvious situation is one where the beam is not perfectly parallel with a crystal axis. As each column will have a range of positions perpendicular to the beam, is the position imaged that at the beam incidence, the exit plane, or perhaps an average of positions through the specimen? To answer this question, multislice simulations have been carried out with varying conditions. Figure 3.3 shows simulated ADF and BF images through 20 nm of PTO at 3 difference focusses and with various perturbations to the tilt of the sample. It is evident from examining the images that the position of the peaks does not significantly change and the contrast is relatively similar even at larger angles. On the other hand the contrast changes significantly in the ABF images shown in Fig. 3.4 where the atom positions become ill defined even at lower angles. To quantify this, the peak positions, and the distances between them, were measured from the simulated images using the exact same program functions used for the experimental images. The displacements have been compared to values obtained for bulk PTO from Joseph *et al.* [137]. For the polarisation measurements required here, it is only the difference in the displacement of the oxygen and B-site cation that has any effect and a mutual shift has no effect. Therefore, the percentage change in polarisation given by the difference in displacement has been measured for each tilt and is shown in Fig. 3.5. As can be seen, the tilt in the ABF image can produce a significant error in the measured displacement (> 100 %). Generally, the y-displacement exhibits the largest changes, though interestingly produces less error for combined positive α and β tilts. The x-displacements are much less severe (< 10 %), even at high tilts, though these shifts cannot be disregarded. A noticeable feature is the inclusion of some anomalous measurements or noise at high β tilts, particularly in the $+1$ nm defocus images. It

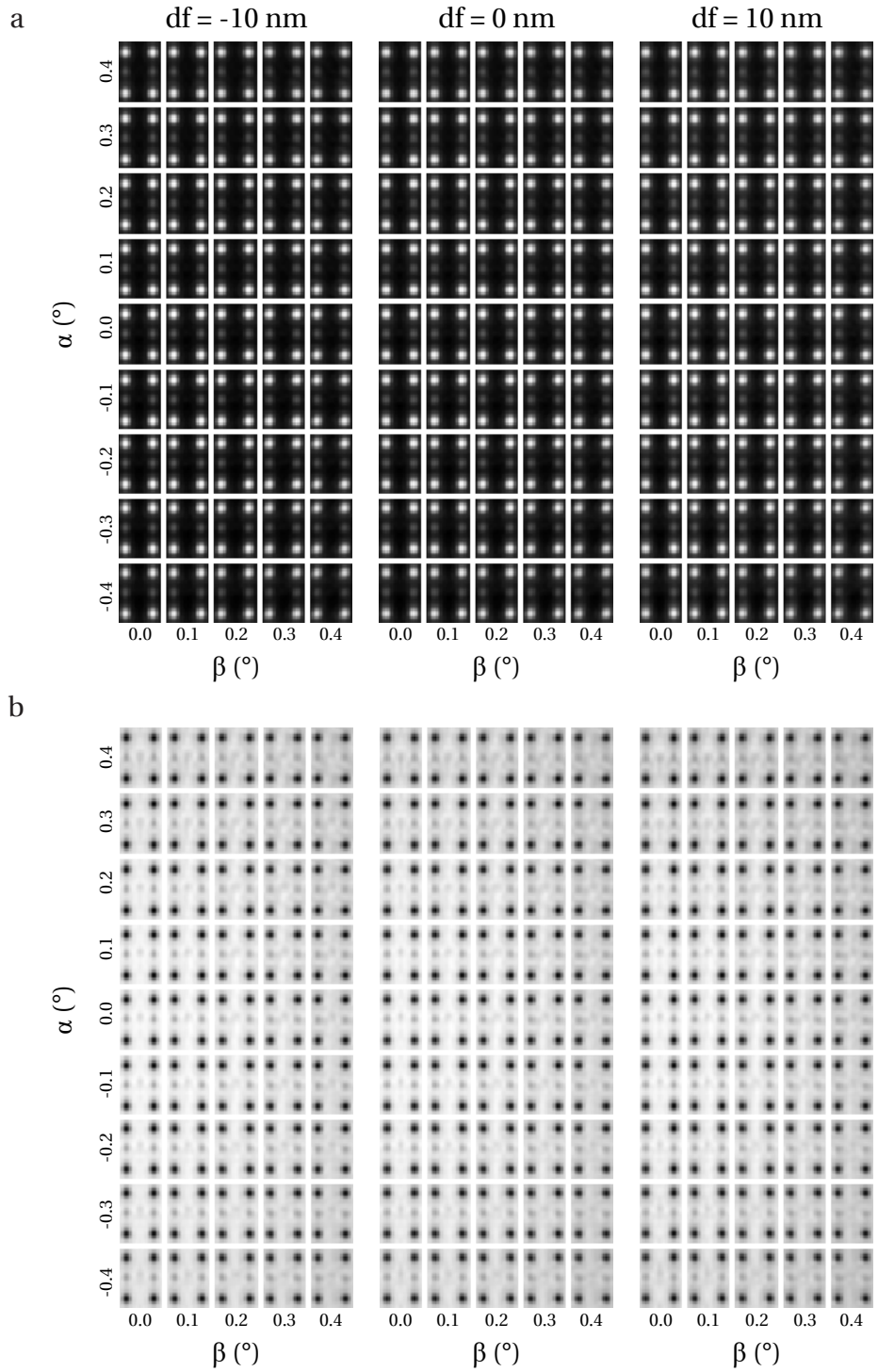

Figure 3.3: (a) and (b) Simulations of annular dark field and bright field images, respectively, of $\langle 110 \rangle$ $PbTiO_3$ with different sample tilt and defocus (df) values. The detection ranges used were 85-267 mrad for annular dark field and 0-23 mrad for bright field. A convergence angle of 20 mrad was used throughout.

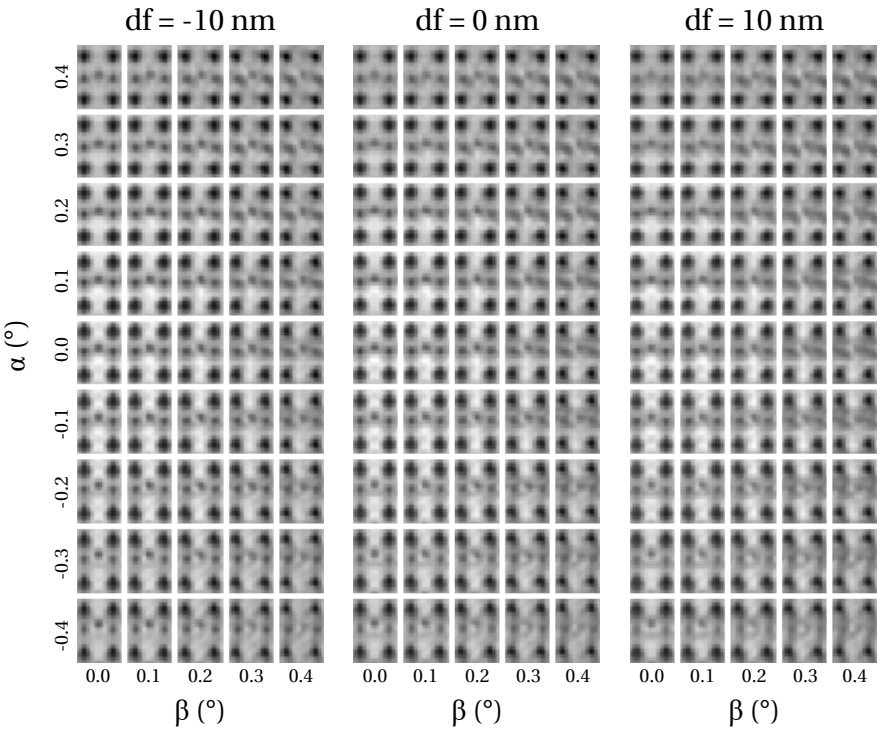

Figure 3.4: Simulations of annular bright field images of $\langle 110 \rangle$ $PbTiO_3$ with various degrees of sample tilt and for different defocus (df) values. The detection range used was 12-23 mrad with a condenser aperture of 20 mrad.

quickly becomes clear that this is an issue with the fitting procedure on the images, rather than an inherent shift of the atom positions. In these images, the O and Ti positions are very poorly defined and even merge in certain cases, causing the fitting to fail or essentially fit the same peak for the O and Ti positions. Luckily, contrast of these strongly affected images is very easy to notice and therefore avoid, however, the accuracy of the measurements can still be unacceptable (up to 20 %), even for tilts of $< 0.2°$.

It is also important to consider thickness effects with sample tilt. It is expected that the thicker a sample, the more effect the tilt has as the projection of an atom column becomes more broad. Likewise, a thinner sample is less prone to tilt effects. Indeed this is the case as shown in Fig. 3.6 where the change in polarisation reaches no more than 30 % even at the extremes. One therefore wants any sample to be as thin as possible, though the usual caveats exist in that the effects of the specimen surfaces need to be considered when the sample is very thin.

It is worthwhile comparing the ABF imaging with the more common ADF and BF techniques. The polarisation errors produced by tilt are significantly less with both ADF and BF imaging as shown in Fig. 3.5. Even at high tilt the errors are reasonable (< 5 %) due to the relatively simple contrast mechanisms. However, it is not always the case that this imaging will produce better results. An obvious flaw is that the oxygen columns are no longer detectable and the relative displacement must be assumed from bulk structure and polarisation measurements. While this assumption will hold in bulk/thick films, it becomes less clear how valid it is when examining thin films where interfaces play a prominent role as well as the varying polarisation magnitudes and directions.

Another issue with the lack of oxygen contrast is that the B-site displacement in bulk material is only on the order of 0.16 Å compared to 0.47 Å for the oxygen displacement. Therefore, any error in the displacement (not just from tilt but other factor such as image noise) will have a larger relative effect, particularly in regions

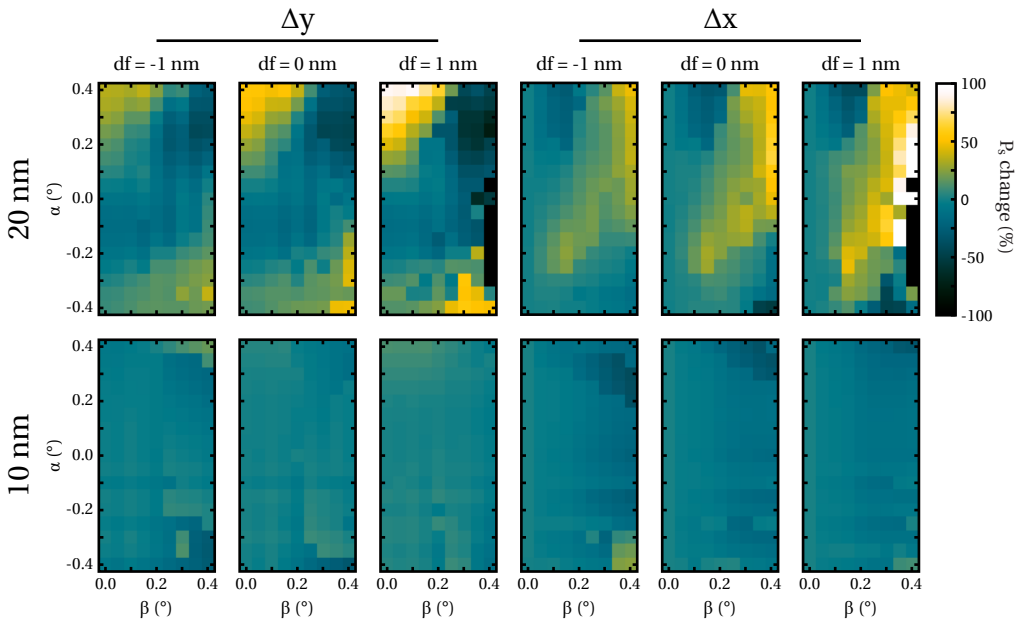

Figure 3.5: Percentage errors in vertical (Δy) and horizontal (Δx) relative displacements with changing α and β tilts as well as different defocusses ($C_{1,0}$). The top and bottom rows show displacements measured from 20 nm and 10 nm thick crystals respectively.

where the polarisation has a lower magnitude. This is compounded in materials such as PTO by the difference in contrast of the Pb and Ti columns, particularly in thinner specimens, where the large, bright Pb contrast can overshadow the dimmer Ti positions, making it harder to detect the small position changes.

As ABF has more potential for accurate polarisation measurements, it is helpful to have a way to confirm the lack of tilt effects (other than belief in the ability of the microscope operator). In the case of the LSMO-PTO system, the LSMO structure provides a reference frame where the oxygen octahedra have the tilt system $a^-a^-a^-$ and therefore, when viewed along the $\langle 110 \rangle$ directions, have either no displacement or alternating up and down displacements. In either case, the average displacement is zero and this can be used to measure any tilt effects present in the image.

Another potential source of uncertainty in any polarisation measurements comes from the projection of multiple domains through the thickness of the speci-

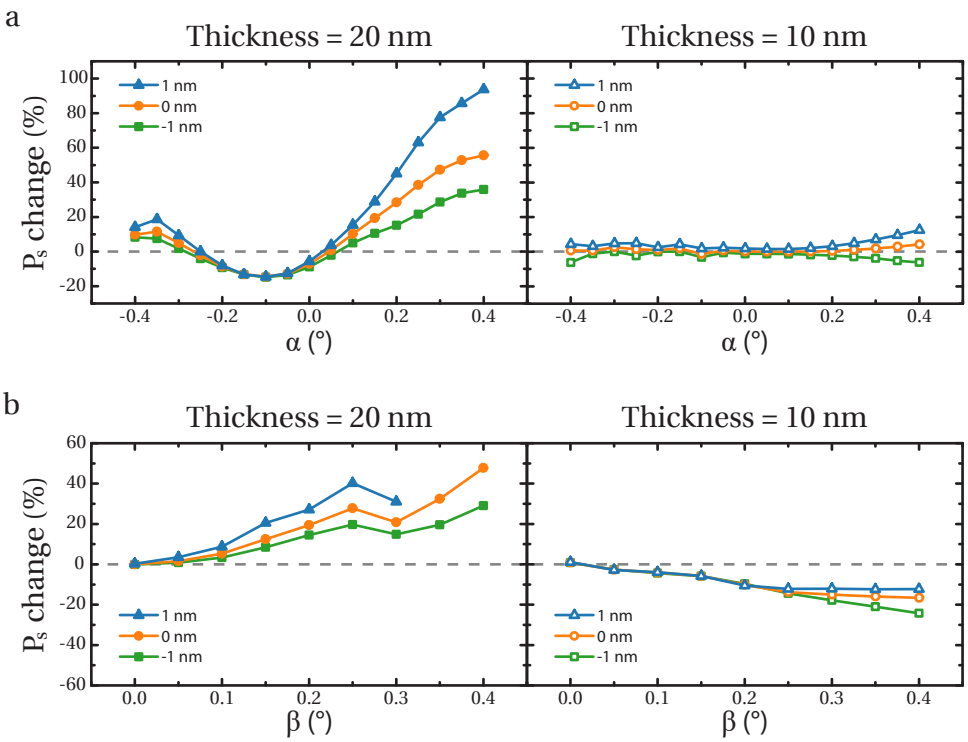

Figure 3.6: (a) Displacement error in the y direction with tilt about the x axis (α). (b) Displacement error in the x direction with tilt about the y axis (β). Left and right plots correspond to the 20 nm and 10 nm thickness crystals and three defocus values have been simulated for each.

men. The Kittel law predicts that the domain widths decrease with the film thickness [59, 60], therefore it may be expected that a TEM specimen on the order of tens of nanometres thick will contain multiple domains and domain walls through its thickness. This will present itself as an error in any measured column position as there will be multiple positions in the projected image. To see the effects of this domain overlap in the STEM images, simulations were performed using an example structure containing two domains oriented by $180°$ to each other and separated by a relatively thick Ising type domain wall with a width of ~ 8 unit cells (Fig. 3.7). The displacement magnitudes of the oxygens in each domain have been set to the bulk values of 0.04672 Å [137] and the displacements in the domain walls smoothly transition between the domains as shown in Fig. 3.7(a). Figures (a-c) show the re-

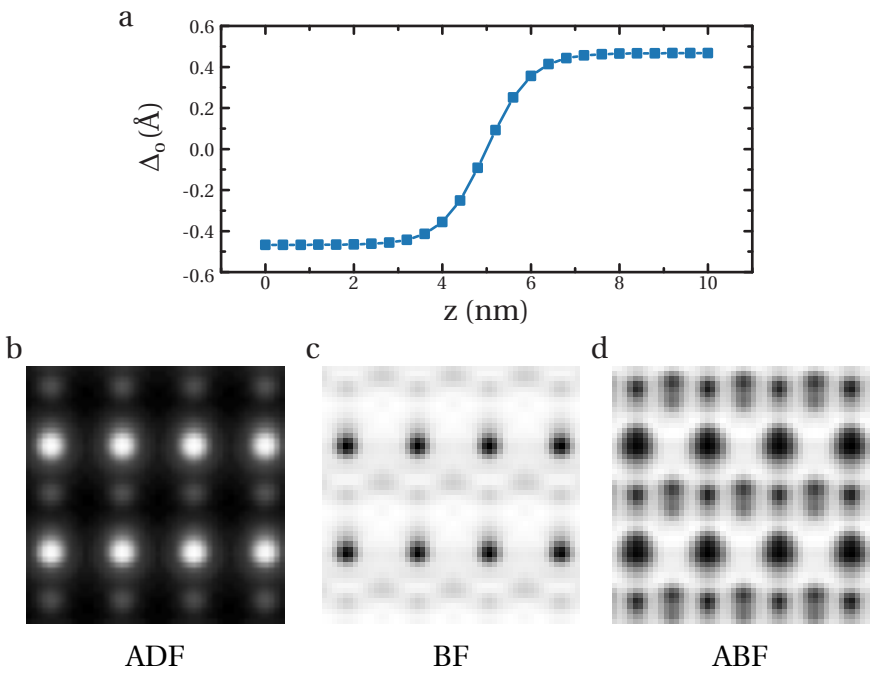

Figure 3.7: (a) Model of oxygen displacements in $PbTiO_3$, Δ_O, as a function of position across a domain wall. The domain wall is Ising type with a width of ~ 8 unit cells. (b-d) $\langle 110 \rangle$ Annular dark field (ADF), bright field (BF) and annular bright field (ABF) image simulations through 10 nm of $PbTiO_3$ with two antiparallel domains in the image projection (as described by (a)).

sulting simulations, in the ABF image there is a clear splitting of the oxygen position that is easily identifiable and can be excluded from any analyses.

Furthermore, the combined displacements are not distinct in the ADF or BF images, making them hard to detect and add an extra uncertainty in the measurements. Considering the ADF image of the 10 nm structure without any tilt (from Fig. 3.7), the error in the oxygen displacement can be as large as 7 % compared to < 0.3 % for the single domain case.

Finally, the stability of the microscope needs to be considered. Unwanted distortions, and therefore uncertainty, can arise from specimen drift, inaccuracy in the scanning coils and external vibrations. Microscope error and external vibrations are generally a function of the microscope and room design and cannot be easily altered. Specimen drift can be reduced by leaving time for the stage to settle, how-

ever even a small amount of drift can easily skew a high-quality, slow acquisition. Equally, drift parallel to the beam will effectively change the defocus, shown above to reduce the accuracy of any displacement measurements. To reduce all of these sources of error in the measurements carried out in this thesis, images were acquired as a stack of images, each with a short beam dwell time at each pixel (typically ~ 5 μs), that where summed to form a high quality, low noise image [138]. To align the image before summing, a rigid translation was used, calculated from cross correlations with sub-pixel refinement from fitting 3-point parabolae. As large specimen drift will not be accurately accounted for using this method, the images were taken after drift had been reduced to < 50 pm s^{-1} and stacks of up to 20 images were used to reduce any effect of focus change. Reducing the distortion in the images using this method gives a position accuracy of ~ 5 pm [6, 7].

3.4 Quantitative polarisation measurements

In its general form, the spontaneous polarisation, $\boldsymbol{P}_{\mathrm{S}}$, of a system is written as

$$\boldsymbol{P}_{\mathrm{S}} = \frac{1}{v} \sum_i \boldsymbol{\delta}_i Z_i, \tag{3.1}$$

where Z_i is the electrical charge of atom i and $\boldsymbol{\delta}_i$ are the displacement vectors from the positions of centrosymmetry (see section 1.2.1). In the case of PTO, this is usually approximated as

$$\boldsymbol{P}_{\mathrm{S}} = \kappa \boldsymbol{\Delta}_{\mathrm{Ti}} = \kappa \left(\delta_{\mathrm{O}} - \delta_{\mathrm{Ti}}\right) = \kappa \left(2.96\delta_{\mathrm{Ti}} - \delta_{\mathrm{Ti}}\right) \tag{3.2}$$

where $\boldsymbol{\Delta}_{\mathrm{Ti}}$ is the displacement of the Ti ion from the centre of the oxygen octahedra (shown in Fig. 3.8), κ is a constant of proportionality and $2.96\delta_{\mathrm{Ti}} = \delta_{\mathrm{O}}$ is an empirical relation between the O and Ti displacements from bulk data [25, 139]. The value of κ is also determined using bulk values and, for PTO, $\kappa = 2726$

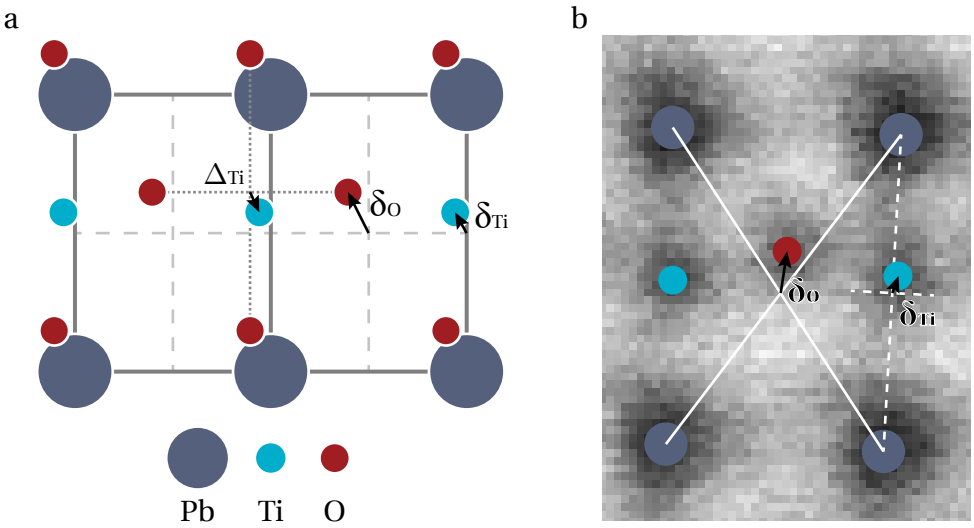

Figure 3.8: (a) Schematic of the $PbTiO_3$ $\langle 110 \rangle$ zone axis showing the relative displacement between the O-sites and B-sites, Δ_{Ti}, as well as the ion displacements from the centres of inversion symmetry, $\delta_{Ti,O}$. Dashed lines are used to indicate the centre of the Pb planes and dotted lines are to indicate the centre of the oxygen octahedra. (b) Displacements shown on an experimental annular bright field image of $PbTiO_3$. The dashed white lines indicate the centre of the 2 nearest Pb neighbours to the Ti position. Solid white lines indicate the centre of the 4 nearest Pb neighbours to the O position.

μC cm^{-2} nm^{-1} [25]. This is then used as an approximation for the polarisation from measuring only the Ti displacements. However, in ABF every atom column in PTO can be resolved, opening the possibility of calculating the polarisation directly as a result of the separation of charge. Eq. 3.1 then becomes

$$\boldsymbol{P}_{\mathrm{S}} = \frac{1}{v}\left(3\boldsymbol{\delta}_{\mathrm{O}}\bar{Z}_{\mathrm{O}} + \boldsymbol{\delta}_{\mathrm{Ti}}Z_{\mathrm{Ti}}\right), \tag{3.3}$$

where v is the volume of the unit cell, $\boldsymbol{\delta}_{\mathrm{O,\,Ti}}$ are the displacements of the O and Ti atoms from the positions of centrosymmetry (see Fig. 3.8) and $Z_{\mathrm{O,\,Ti}}$ are the effective charges of the O and B atoms. In the measurements made here, the Pb lattice is used as a static reference frame to define the non-polar positions of the O and Ti ions. This is calculated as centre of gravity of the 4 and 2 nearest neighbours to each O and Ti ion respectively (see Fig. 3.8(b)).

The values for the charges used here have been calculated by Bellaiche & Vanderbilt [140] using the Berry-phase approach. Note that because there are three oxygen atoms per unit cell with two distinct symmetries, the effective charge is defined as an average of their values. Using these charge values the values of $\boldsymbol{\delta}_{\mathrm{O,\,B}}$ and v can be measured from the TEM images, it is therefore possible to get a measurement of $\mathbf{P}_{\mathrm{S}}$ on a unit cell by unit cell basis. In this work the polarisation is mapped using the 2D unit cell of the projected $[110]$ image (i.e. defined by two perpendicular vectors with lengths of $\frac{1}{2}\sqrt{a^2+b^2}$ and c, where a, b and c are the 3D unit cell vectors) instead of the 3D unit cell. This is purely for convenience as each 2D unit cell has one oxygen column at its centre (the choice of unit cell for polarisation measurements has been discussed in section 1.2.1).

3.5 Polarisation mapping

As TEM can measure the position of an atom column to a precision of ~ 5 pm, it is possible to accurately measure $\mathbf{P}_{\mathrm{S}}$ from a TEM image, even on the single unit

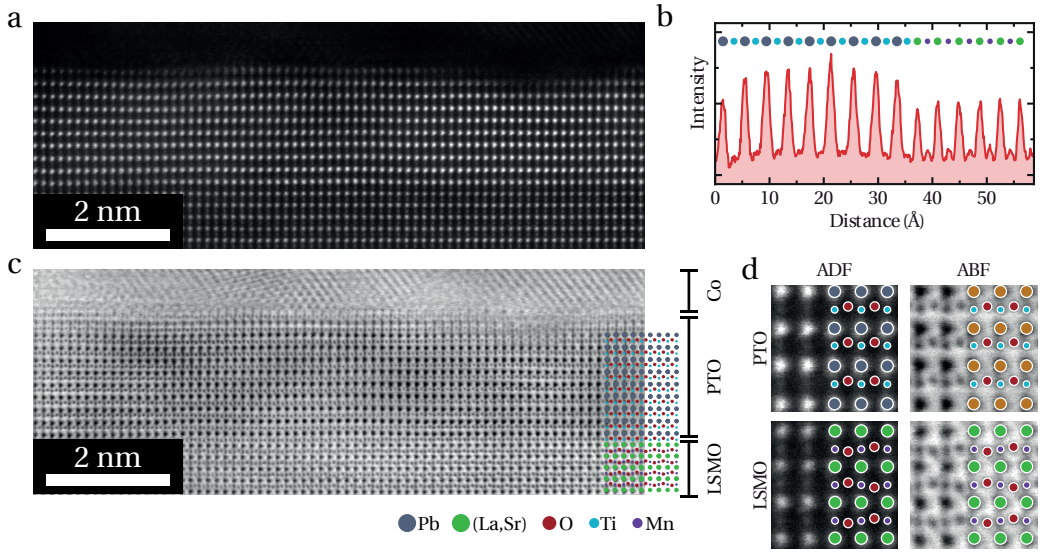

Figure 3.9: (a) Atomic resolution annular dark field (ADF) image of the 9 u.c. multiferroic tunnel junction. (b) Intensity plot from (a) showing atom column composition. (c) Annular bright field (ABF) signal collected simultaneously to (a). (d) Magnified regions from (a) and (c) showing the structure in $(La_{0.7}Sr_{0.3})MnO_3$ (LSMO) and $PbTiO_3$ (PTO) and the difference in contrast.

cell level. Using this, the domain structure can be revealed [7, 141] even in true nanoscale systems such as the ferroelectric tunnel junctions.

3.5.1 3.6 nm thick film

Figure 3.9(a) shows an ADF image from the 3.6 nm (9 unit cells (u.c.)) PTO sample, including the interfaces with the Co and LSMO electrodes. Using the fact that the ADF signal is sensitive to atomic number, it can be seen that there is a high quality epitaxial interface between the PTO and LSMO. The intensity profile across the interface, shown in Fig. 3.9(b), suggests that the termination is Ti-O/La-Sr. Whereas PTO and LSMO share a (relatively) common structure, the Co does not, combined with the fact that it was grown ex-situ means that the interface quality is not as good. Figure 3.9(c) shows the corresponding ABF image where the O^{2-} columns are now visible and the B cation contrast has improved. From this image the atom column positions are measurable to a few picometres [7, 141]. Side by side ADF

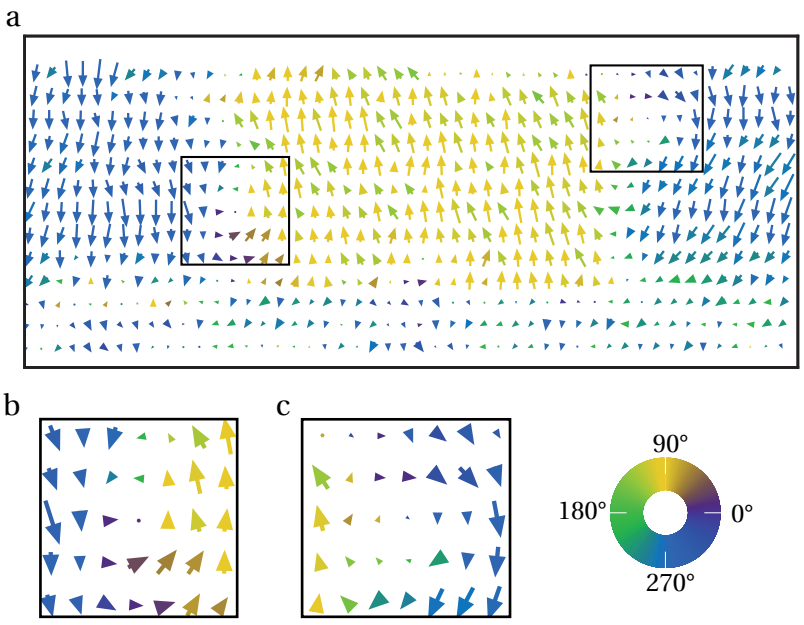

Figure 3.10: (a) Quiver plot of dipoles measured from Fig. 3.9(c)showing three domains. (b) and (c) Enlarged versions of the regions highlighted on the left and right domain walls in (a) respectively. Each area is centred on a vortex.

and ABF images are shown in Fig. 3.9(d) to highlight the differences in contrast. From these images, the ferroelectric oxygen displacement upwards is immediately observable in the PTO as well as the alternating up/down displacements from the octahedra tilting in the LSMO.

The two dimensional quiver plot of the local dipole, shown in Fig. 3.10(a), indicates that PTO is in a ferroelectric state. In the centre of the image, the polarisation points upwards towards the Co whereas on the left and right polarisation points downwards, i.e. a classic 180° Kittel domain structure. This would be expected to show Ising-type domain walls with a wall width of the order of 2 u.c. [26, 142]. Nevertheless, a relatively wide wall with a roughness of about 4-5 u.c. is revealed. Additionally, the polarisation map provides evidence of two small vortices, highlighted in Figs. 3.10(b) and 3.10(c). In these areas, the dipole direction changes continuously anti-clockwise and clockwise, respectively, forming a paired vortex and anti-vortex state similar to the PTO-STO superlattice case reported by

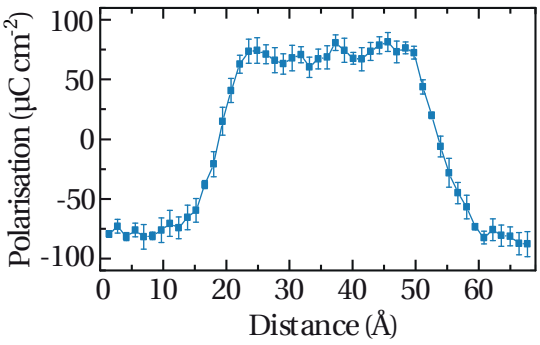

Figure 3.11: Average out-of-plane polarisation across the domains shown in Fig. 3.10. Error bars are the standard errors of the means.

Yadav *et al.* [56]. The vortices are located at the domain walls, forming a more complex structure separating the two opposite ferroelectric domains. The clockwise vortex is observed close to the Co-PTO interface whilst the anti-clockwise vortex is near the LSMO-PTO interface. Note that no projection effects are seen, where the atom columns contain varying displacements perpendicular to the beam direction indicating that the measured dipoles are constant through the thickness of the specimen. This would not be the case if domain walls existed within the thickness of the TEM specimen so that two separate domains are projected on top of each other (see Fig. 3.7).

From Fig. 3.10 it can therefore be inferred that the depolarisation field, always present in ferroelectric films, has an effect on the polarisation distribution when the PTO film thickness is below 10 unit cells, though this may extend to even thicker films, as predicted by ab-initio calculations [143]. It is important to note the asymmetry of the electrodes and how this affects polarisation in the PTO ultrathin film. Vertically averaging the out-of-plane polarisation gives Fig. 3.11 with the amplitude smoothly changing between positive and negative at the domain walls. The polarisation pointing down towards the LSMO electrode has an average value of 80$\pm$1 μC cm^{-2}, close to the value of $\sim$84 μC cm^{-2} obtained using bulk displacements [139]. There exists a decrease in the polarisation magnitude towards the Co (70$\pm$2 μC cm^{-2}), a result of the asymmetric screening of the depolarisation field

by the different electrodes. Cobalt, as a good metal, is able to screen the positive and negative charge accumulation, whereas LSMO is a half-metal with lower carrier concentration than Co [144]. Figure 3.11 also shows the rougher/thicker (4-5 u.c.) domain walls from the observed in-plane (90°) component of the polarisation vortices. This will have an effect on the domain wall motion and the piezoelectric coefficient.

3.5.2 2.4 nm thick film

Comparable analyses were carried out in heterostructures containing 2.4 nm (6 u.c.) of PTO between similar LSMO and Co electrodes. ADF and ABF imaging, Figs. 3.12(a) and 3.12(b) respectively, again demonstrate an excellent crystal quality with defect free atomically sharp interfaces. At first glance, both 9 u.c. and 6 u.c. look the same, but the quiver plot of the dipole in 3.12(c) indicates a drastic change in the domain pattern, although the PTO is still in a polarised state. The relatively well-defined domain walls (with associated small vortices) observed in 9 u.c. of PTO have been replaced with a structure showing a combination of Landau-Lifshitz flux closure domains and vortices. However, over a large area (∼75 nm) there is a high degree of disorder: Areas where polarisation switches from the top to bottom of the layer (Fig. 3.12(e)), complex regions of curling (Fig. 3.12(f)) and (110) type domain walls forming at 45° to the interface (Fig. 3.12(g)), typical of thicker films.

Some of these types of domain walls have been predicted by first-principles based methods for thicknesses corresponding to 6 u.c.. For instance, closure at the bottom LSMO electrode may occur as a response to the asymmetry in the electrode screening [61]. The high degree of disorder with a certain remanent periodicity (particularly of the downwards polarisation) observed here suggests that the system actually enters into an incommensurate phase. It has been recently predicted that general ferroelastic systems in a certain range of dimensionality no longer undergo a simple para-ferro phase transition, instead entering, across the tri-critical

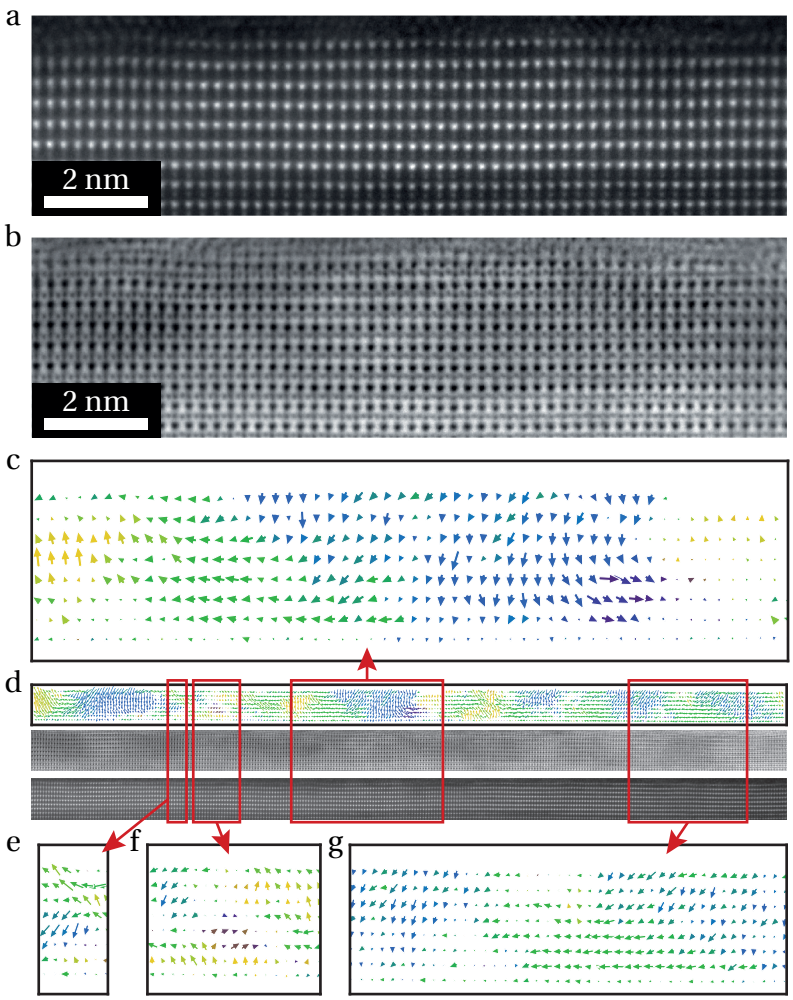

Figure 3.12: (a) and (b) Atomic resolution annular dark field (ADF) and annular bright field (ABF) images respectively. (c) Corresponding quiver plot of dipoles. (d) Large area analysis showing a dipole map, ABF and ABF images. (e)-(g) Regions of interest taken from the indicated regions of (d).

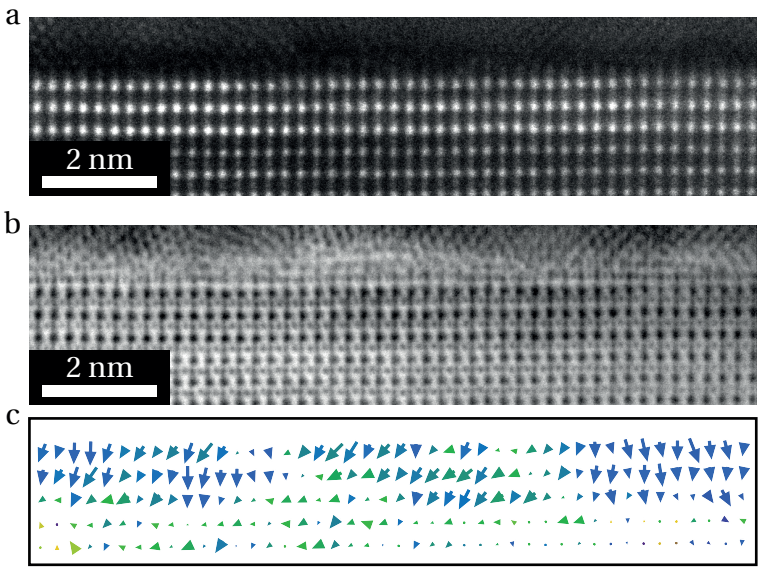

Figure 3.13: (a) and (b) Atomic resolution annular dark field and annular bright field images respectively. (c) Corresponding quiver plot of the local dipoles.

Lifshitz point, an incommensurate phase [145]. The driving force for this is the flexoelectric effect. Indeed our investigated PTO is both ferroelectric and ferroelastic and, under a certain thickness, additional parameters such as inhomogeneous electric fields might induce crossing of the Lifshitz point and drive the system into an incommensurate phase. Nevertheless, applying external electric field switches the polarisation as expected for a proper ferroelectric film (the TER effect is about 81 % as in Fig. 3.1(b)).

Interestingly, at the Co interface, the domain width can be up to $\sim$8 nm, larger than in the 9 u.c. sample (6.4$\pm$0.2 nm), though at the LSMO interface the domain reduces to $\sim$4 nm. Other domains with parallel walls, 45° to the substrate, have constant widths across the thickness of the film and can be as small as $\sim$3 nm. Thus the average of the measured widths is 5.3$\pm$0.7 nm, in agreement with the expected value of 5.2 nm obtained from the Kittel scaling law using the 9 u.c. domain width as input [58]. Due to the range of domain widths, depending on the particular domain and how the width is defined, it is likely that this is just coincidence, however it may be that measurements from the literature are measuring an

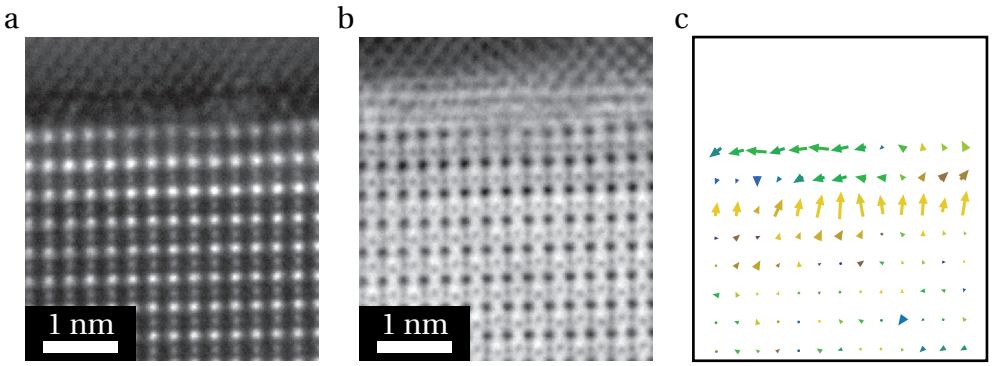

Figure 3.14: (a) and (b) Atomic resolution annular dark field and annular bright field images respectively. (c) Corresponding quiver plot of the local dipoles.

average effect and do not detect the variation in domain width.

3.5.3 1.2 nm thick film

Further reducing the thickness of the ferroelectric film to 1.2 nm (3 u.c.) results in the domain structure largely disappearing in unpoled material (Fig. 3.13). Instead the polarisation shows a significant gradient across the entire film thickness (Fig. 3.13(c)). Remanent curling/in-plane polarisation is present, but polarisation largely points from Co to LSMO. This is in contrast to theoretical models of equivalent films of PZT and BTO that show in-plane and random polarisation respectively [37]. These models do not account for any electrodes, suggesting that it is only the presence of the LSMO and Co that allows the out-of-plane polarisation from Fig. 3.13.

The magnitude of the polarisation at the Co interface is 76±5 μC cm^{-2} on average, the same as the equivalent measurement in 9 u.c. of 79±1 μC cm^{-2}, whilst the displacements at the LSMO interface are zero. This suggests that 3 u.c. is the lower limit of ferroelectricity in PTO on LSMO under this positive in-plane misfit strain. The TER effect disappears which is an indication that the ferroelectric polarisation cannot be switched any more, likely due to its gradient within the ferroelectric layer. We note that this gradient in polarisation must be associated with

a gradient in electric field and therefore with free charge localised within the ferroelectric layer. The TER effect for the 3 u.c. layer is suppressed, but the TMR effect is still significant. This demonstrates that the tunnel junction device based on the 3 u.c. PTO layer is functional but the internal gradient causes polarisation to become non-switchable.

In addition to this, some areas have been found that show an unexpected polarisation pattern where the polarisation reaches high out-of-plane values at the LSMO-PTO interface, but quickly decays to 0 at the Co interface where there is an in-plane component; an example quiver plot is shown along side the corresponding ADF and ABF images in Fig. 3.14. Looking closely at the two polarisation configurations, there seems to be a correlation with the tilt angle in the LSMO octahedra. Regions with a large out-of-plane polarisation in the PTO exhibit a tilt angle of $\sim 7^{\circ}$ whilst in these polarisation suppressed regions, the tilt is typically as high as $\sim 11^{\circ}$. Additionally, several differences can be noticed between the 9 u.c. case, where polarisation extends in to the LSMO, and the 3 u.c. case, where polarisation is zero at the LSMO. This will be discussed further in the next section.

3.6 Polarisation profiles

As the interfaces play such an important role in the functionality of the device and the polarisation configuration, it is enlightening to see exactly how the polarisation and structure change across the interfaces. As it is not possible to measure the polarisation or structure in the Co top electrode in any meaningful way, this section will examine the PTO-LSMO interface exclusively.

Figure 3.15 shows the profiles for both the polarisation and octahedral tilt from the specimen with 9 unit cells of PTO. The polarisation is relatively uniform within the PTO layer as is close to expected bulk values around 80 μC cm^{-2} [146–148]. There is a small decrease at the Co interface that may be associated with the

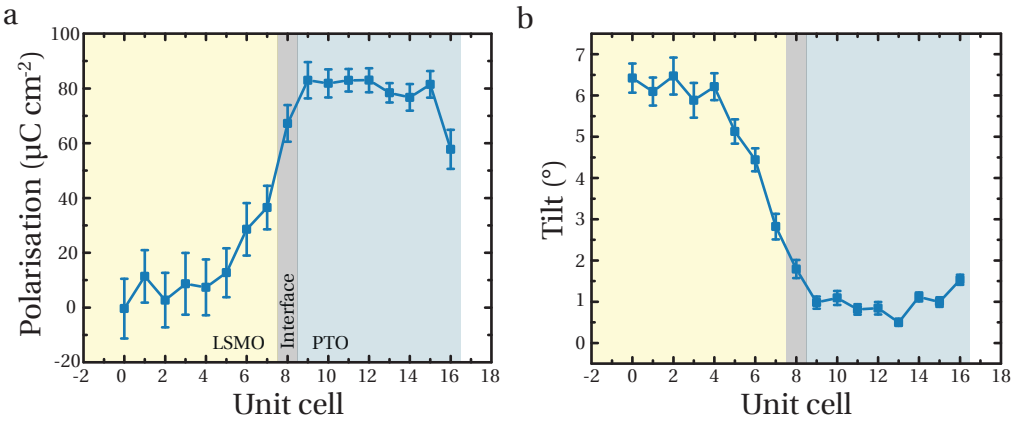

Figure 3.15: (a) Out-of-plane polarisation profile for a multiferroic tunnel junction with 9 unit cells of $PbTiO_3$. (b) Corresponding profile of the oxygen octahedra tilt angles. The region labelled as 'Interface' is where the O and B-sites are positions between Pb and (LaSr) A-site cations.

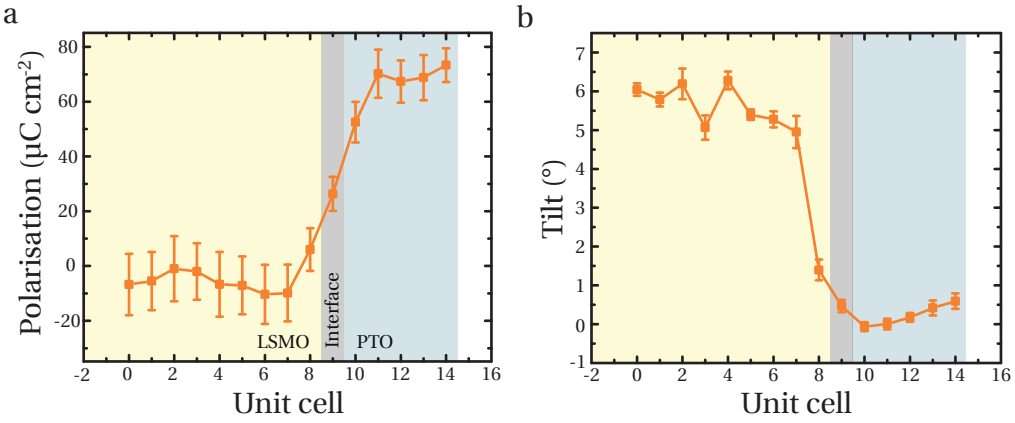

Figure 3.16: (a) Out-of-plane polarisation profile for a multiferroic tunnel junction with 6 unit cells of $PbTiO_3$. (b) Corresponding profile of the oxygen octahedra tilt angles. The region labelled as 'Interface' is where the O and B-sites are positions between Pb and (LaSr) A-site cations.

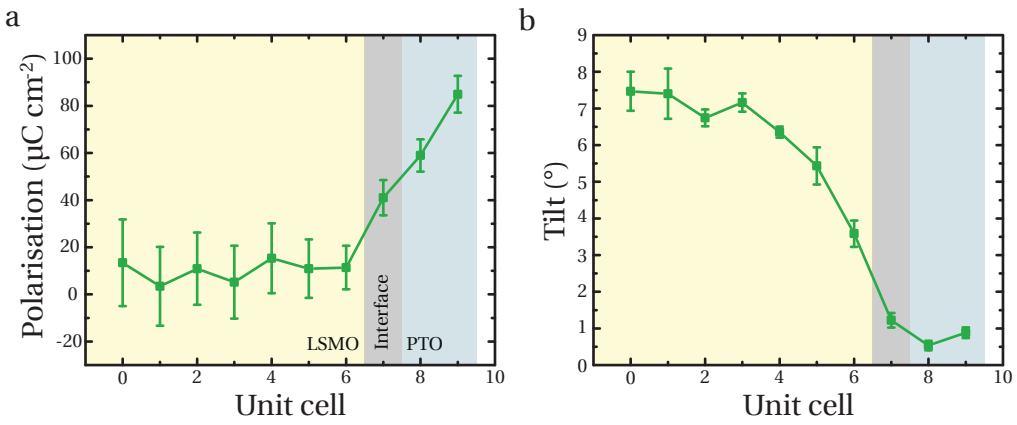

Figure 3.17: (a) Out-of-plane polarisation profile for a multiferroic tunnel junction with 3 unit cells of $PbTiO_3$ similar to Fig. 3.13. (b) Corresponding profile of the oxygen octahedra tilt angles. The region labelled as 'Interface' is where the O and B-sites are positions between Pb and (LaSr) A-site cations.

penetration of free charge and/or damage to the top layer. At the same time, the LSMO interface also shows a decrease in polarisation but the ionic shifts continue ~ 2 unit cells into the LSMO itself where the bound charge can be screened in-situ. Clearly there is an influence from the PTO on the LSMO near the interface. This is backed up by Fig. 3.15(b) where again the tilt in the PTO layer is uniformly minimal, but in the LSMO, there is a decrease of the expected tilt ∼2-3 unit cells from the interface.

This is not the case for MFTJ grown with 6 unit cells of PTO, as shown in Fig. 3.16. Now the polarisation starts to decrease within the PTO itself and only influences the first unit cell of LSMO. The tilt shows only a similar pattern in that the rotations are still uniform within the PTO, but again, only the very first layer of LSMO is affected. Note that there is no reduction of the polarisation at the Co interface, suggesting that the effect at this interface in Fig. 3.15(a) is due to structural abnormalities and is not purely an effect of the interface.

The 3 unit cells sample further develops the trend of Figs. 3.15 and 3.16. The polarisation is now purely in the PTO with no apparent effect on the LSMO whilst the octahedral tilting is still minimal in the PTO, including the interfacial region.

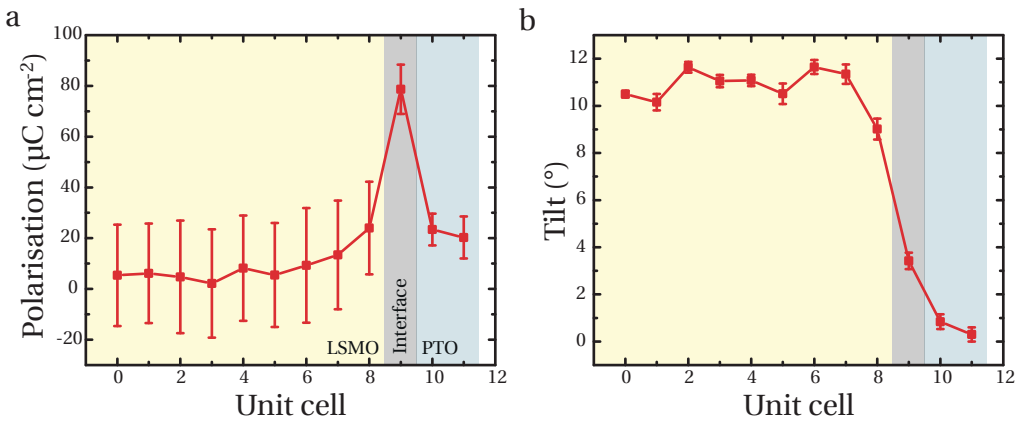

Figure 3.18: (a) Out-of-plane polarisation profile for a multiferroic tunnel junction with 3 unit cells of $PbTiO_3$ similar to Fig. 3.14. (b) Corresponding profile of the oxygen octahedra tilt angles. The region labelled as 'Interface' is where the O and B-sites are positions between Pb and (LaSr) A-site cations.

The polarisation profiles show that, at thicker PTO films, the ferroelectric PTO structure is dominant and the local LSMO is distorted to give a continuous change between the two. At lower thicknesses, the LSMO structure becomes more influential and contorts the PTO film. Interestingly, for all thicknesses, the gradient of the polarisation is always $\sim 20\mu$C cm^{-2} per unit cell (18 ± 2, 21 ± 1 and 24 ± 2 μC cm^{-2} per unit cell for the 9, 6 and 3 unit cells of PTO respectively). Because of this similarity, it is possible that the gradient is a property of the LSMO screening ability or the maximum strain gradient the system can handle. This will dictate the stability of polarisation in such thin films. At lower thicknesses, the required gradient to produce the polarisation is much larger and this may be the reason the ferroelectricity is suppressed in such systems.

Using the phenomenological theory set out by Kretschmer & Binder [41], the constant polarisation gradient also indicates that the shift in the polarisation penetration into the LSMO is purely related to the correlation length (a measure of the distance over which the electric dipoles interact) in the PTO film. Changing the film thickness alters the distribution of free charge in the ferroelectric. An explanation of the in-situ screening of polarisation inside the ferroelectric considers doping or the

change in interface termination [48, 149, 150]. This phenomenon does not explain why the start of the polarisation gradient shifts so systematically with film thickness and Z-contrast; ADF imaging indicates no appreciable doping in any of the examined structures and that the interface is always TiO_2-(La,Sr) terminated. Instead there must be a penetration of free charge into the PTO film, the penetration being driven by the competition between the PTO and LSMO structures.

Figure 3.18 shows the polarisation and tilt profiles for the area shown in Fig. 3.14. The large out-of-plane polarisation is visible in the interfacial region that is close to the expected bulk polarisation. The polarisation then diminishes towards the Co electrode as the out-of-plane component is replaced with an in-plane polarisation. The octahedral tilt profile shown in Fig. 3.18(b) shows two interesting phenomena: The tilt in the LSMO is significantly larger than Figs. 3.15-3.17 with a value of $\sim 11^\circ$ instead of 6-7°. In addition, the tilt at the interface unit cell is $3.4 \pm 0.3^\circ$ whereas the other specimens exhibit minimal rotations. This kind of combined antiferrodistortive octahedral tilting and ferroelectric displacements has only been observed before in PTO surfaces, driven by surface reconstruction [151, 152].

The origin of this phenomenon is unknown, though it is interesting to note the link between the peculiar polarisation configuration and the octahedral rotations in the LSMO. It is possible that a defect has been introduced at the STO-LSMO interface where the strain has enhanced the octahedral rotation in LSMO. This stronger rotation has then affected the competition between the LSMO and PTO such that octahedral tilting has been induced in the PTO interface and suppressed the out-of-plane polarisation. This, however, does not account for the large polarisation present in the interface region, where there must be an introduction of free charges in the PTO layer to screen the large depolarising field.

3.7 Chapter summary

Here it has been shown that in PTO-based MFTJs the ferroelectric domain pattern changes drastically even as the ferroelectric layer is changed by 3 u.c.. A classic antiparallel ($180°$) domain configuration is found for 9 u.c. thick PTO films with Ising type domain walls decorated with a pair of clockwise and anti-clockwise vortices. The domain configuration after reducing the PTO thickness to 6 u.c. changes drastically and now exhibits flux closures and an incommensurate phase. Again reducing the thickness by 3 u.c. produces relatively featureless domain configurations with polarisation pointing in one direction.

The effects of the PTO-LSMO interface have also been explored, with a change of the polarisation profile found as a function of the PTO thickness. Additionally, an unexpected link between the degree of oxygen octahedral tilt in LSMO and the polarity in the PTO has been found.

The present results show that the polarization curling and formation of vortex and flux-closure structures is a generic effect that appears in ultrathin ferroelectric films, even with metal electrodes. The screening of such electrodes does not prevent these polarization curling structures from forming and the possibility to manipulate these structures with local electric fields is open.

Chapter 4

Relaxor like behaviour in Pb_2ScTaO_6 as studied by transmission electron microscopy

4.1 Introduction

PST is a double perovskite that exhibits 1:1 ordering of the Ta and Sc on the B-site positions (see section 1.3.4). It exhibits a wide range of phenomena, most notably it is a relaxor ferroelectric when the B-site is disordered; increasing this order causes the material to behave more like a classical ferroelectric [68, 70, 83, 86, 88]. The defining characteristic of a relaxor is traditionally the temperature dependence of the dielectric that shows a frequency dependent, broad transition, in contrast to a traditional ferroelectric (see Fig. 1.14). This is associated with the transition from a paraelectric to a polar state where the polarisation is arranged in randomly oriented polar nano regions - polarised regions that fluctuate or 'flicker' with time. The PST studied in this chapter is highly ordered and does not exhibit the frequency dependent dielectric maximum (shown later in section 4.3.2) and can therefore not be called a relaxor ferroelectric. However, the material still exhibits

several phenomena, such as the presence of fluctuating polar regions, that are not fully understood or characterised.

Due to the fluctuations of the polarisation, it is difficult to properly examine the dynamics as the acquisition time for measurements (e.g. X-ray diffraction (XRD)) is significantly longer than the fluctuation frequency and, in some materials, the fluctuations appear static on timescales on the order of 10^{-12} s. What is in fact observed is an average of all the fluctuating states. Therefore, though relaxors have been studied since the 1950s, a complete understanding of relaxor behaviour is not available today [153], particularly at the nanoscale. To properly probe the fluctuations, a high time resolution is needed to properly determine the dynamics of such a material. In the field of electron microscopy, the relatively recent move towards digital control and developments in CCD acquisition mean that it is possible to acquire and store data with sufficient time resolution to study the PNRs.

4.2 Structure

All material studied in this chapter is in the form of polycrystalline ceramic PST that has been crushed with a pestle and mortar before TEM preparation. The original sample was fabricated using the mixed oxide method detailed by Osbond & Whatmore [154].

4.2.1 B-site ordering

As the properties of PST depend on the degree of ordering (and the distribution of that ordering can be different [69]), it is important to have a complete understanding of the sample ordering so that comparisons can be made to theory and previous experimental results. The ordering in PST presents itself as chequerboard/rock-salt ordering, where the B-site cations (Ta and Sc) alternate along the $\langle 100 \rangle$ directions (see section 1.3.4). This results in the $\{111\}$ planes only containing one species of

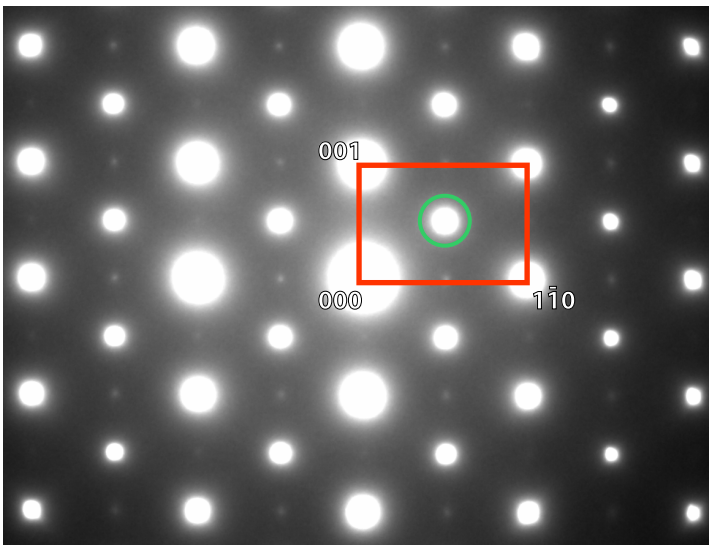

Figure 4.1: $\langle 110 \rangle$ high dynamic range electron diffraction pattern obtained from Pb_2ScTaO_6. The initial exposure time was 120 s. The reciprocal net has been highlighted with a red box and a $\frac{1}{2}1\bar{1}1$ ordering spot has been circled in green.

B-site cation and also doubles the unit cell size. The doubling of the $\{111\}$ planes is easily verified using selected area transmission electron diffraction. Figure 4.1 shows a $\langle 110 \rangle$ zone axis electron diffraction pattern where the presence of the extra $\frac{1}{2}\{111\}$ ordering spots is immediately obvious.

At this time, a note should be made on the choice of reference cell for indexing PST. Firstly, though the crystal system is rhombohedral at low temperatures, the pseudocubic cell has been used for simplicity throughout. Secondly, two separate reference cells for double perovskites are often used: The full double perovskite cell that includes the ordered B-sites or the single perovskite cell. The first is more crystallographically correct and represents the true structure, but the latter is perhaps more intuitive when comparing to traditional perovskites. Using the double perovskite cell to index the diffraction pattern in Fig. 4.1, the red square is defined by the 200 and 022 reflections. Using the single perovskite cell, the red square is defined by the 100 and 011 vectors. In this work, the indices given will correspond to the single perovskite cell.

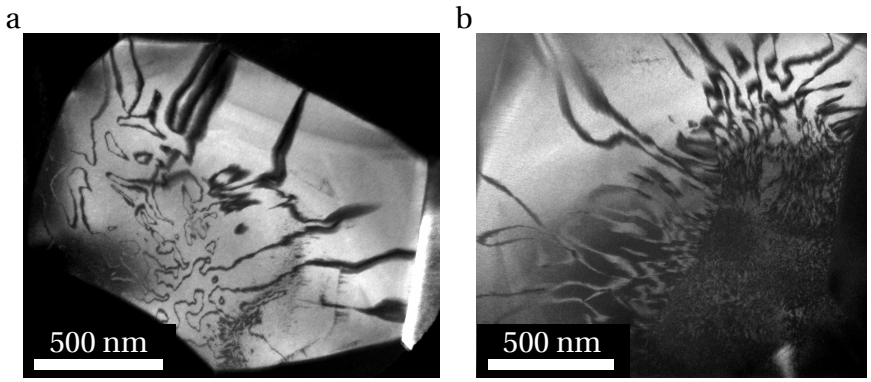

Figure 4.2: (a) Dark field transmission electron microscope image from a highly ordered single grain of Pb_2ScTaO_6 where the ordering can be seen as bright regions with the dark regions corresponding to meandering anti phase boundarys. (b) A separate grain from the same sample as (a) where the ordering is similar. The top and left side resemble (a) whilst the bottom right area has significantly more disorder.

Whilst diffraction provides an easy way to detect the presence of ordering, many of the properties of the PST depend on the extent of the ordering and it is not currently possible to extract this information quantitatively from a diffraction pattern. However, as the diffraction spot relating to the ordering can be identified, it is possible to isolate the spot for dark field imaging and observe the distribution of ordering. Figure. 4.2 shows two dark field images, from the same growth, taken using $\frac{1}{2}1\bar{1}1$ type spots.

Figure 4.2(a) shows a crystallite almost completely ordered. APBs, across which the crystal structure is displaced by half a unit cell, can be seen meandering through the crystal with a lower density at the edges. Figure 4.2(b), however, shows a mixture of highly ordered regions next to much more disordered regions. Characterising the materials properties in bulk then becomes more difficult as the ordering, and therefore properties, changes within the material and any bulk measurements will probe an average of these properties. The samples studied here contain predominantly regions with ordering similar to 4.2(a) and, for lack of a true quantification of the bulk, the sample will be treated as highly ordered ($> 85\%$) as

measured from ratio of bright to dark contrast in Fig. 4.2(a). Where possible in TEM experiments, similar dark field measurements have been taken from the examined regions to ensure a high degree of order is present.

The Z-contrast of ADF can also be leveraged to see the ordering on the atomic level. The atomic number of Ta is significantly larger than Sc (73 compared to 21) so the ordering should be immediately visible without performing any detailed analysis. Figure. 4.3 shows two $[110]$ ADF images which show the ordering. Fig. 4.3(a) shows a region with relatively high ordering and the Sc atoms appearing dark compared to the Ta atoms. Even in these highly ordered areas, however, there are fluctuations in the intensities of the Ta and Sc columns. Figure 4.4(a) shows the histogram of the peak intensities taken from the Voronoi cell around each position (defined by partitioning the image into areas closest to each atom column). Whilst there is a clear splitting in the intensities of the different B-sites due to the ordering, the intensity distribution is broad for both Ta and Sc columns. This shows that the ordering is not just split between purely ordered and disordered, but there is a small variation in the disorder in all areas. It should be noted that as the image is a projection through the 3D structure, it is not clear if this variation occurs everywhere, or if the small changes in order happen between contiguous regions. Despite this particular material not being a relaxor, this mixing of ordering supports several of the theories that require such non-negligible variations to explain the relaxor properties [75, 80]. Figure 4.3(b) shows a region containing an APB where the π phase shift is highlighted by the shift in the planes containing the Ta atoms. This boundary also produces mixing of the Sc and Ta columns along its length as seen from the homogeneous Z-contrast and explains why the APBs are visible in Fig. 4.2; the APBs can be considered as thin regions of disorder.

Due to the intricacies in the ADF image intensities, it is worthwhile to ensure that the ordering and structure are indeed as previously described. EDX measurements can reveal the ordering on the atomic scale through explicit measurements

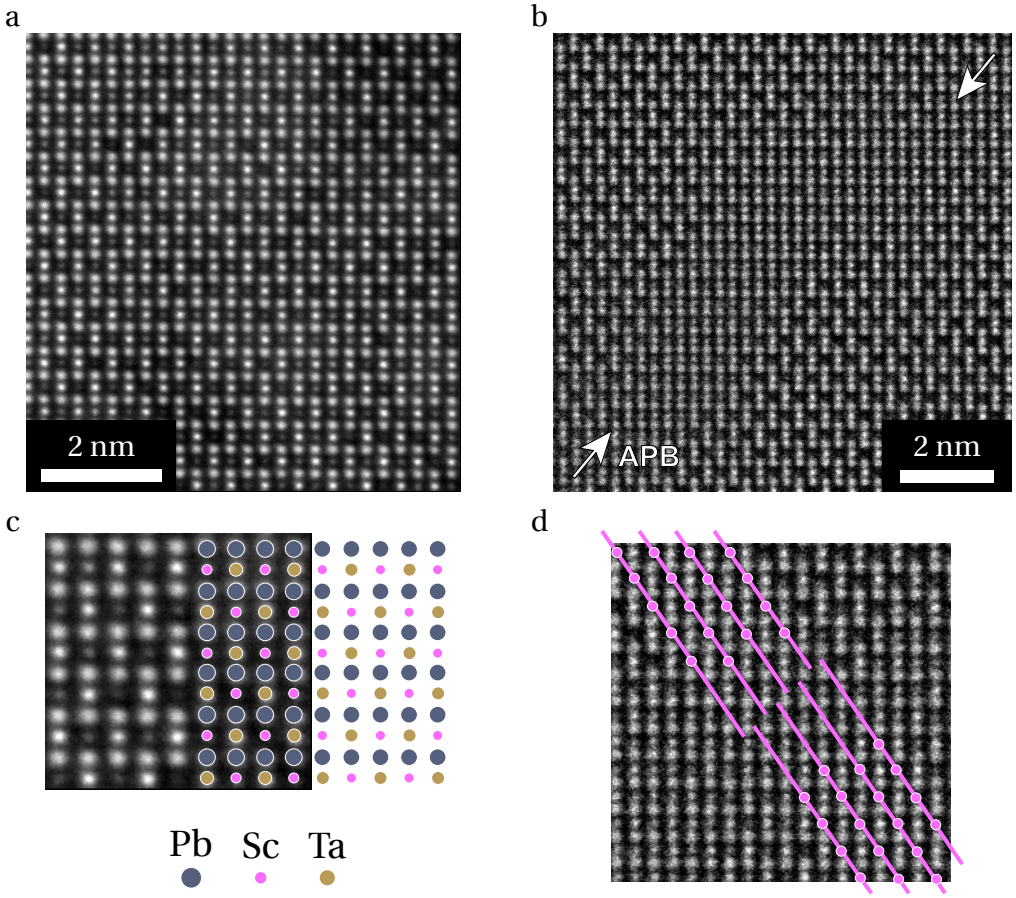

Figure 4.3: (a) Annular dark field (ADF) image of the $\langle 110 \rangle$ zone axis in Pb_2ScTaO_6 where the ordering is revealed through the alternating intensities of the Sc (dark) and Ta (bright) ions. Closer inspection reveals small variations in the intensities of the columns as the ordering is not 100 %. (b) ADF image of a separate region showing an anti phase boundary (APB) running diagonally from bottom left to top right. (c) A magnified region of (a) with the structure overlaid. (d) Enlarged region of (b) where the Sc columns and planes have been highlighted to shoe the phase shift across the boundary.

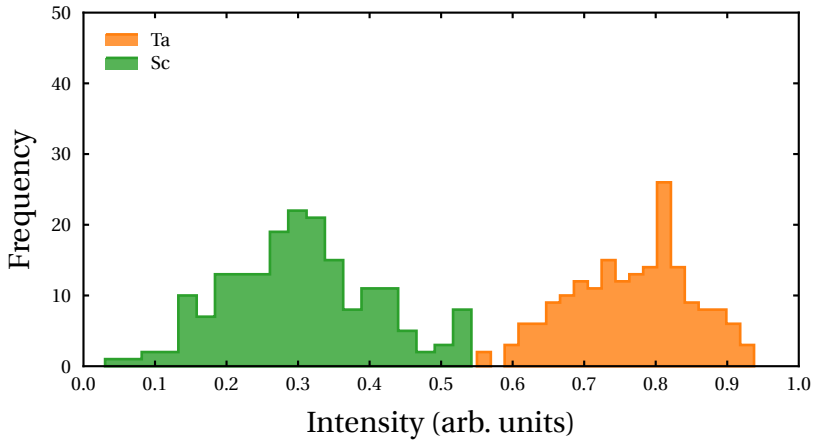

Figure 4.4: Histogram of the Ta and Sc column intensities measured from Fig. 4.3(a). Intensities were measured as the average of the data within the Voronoi cell around each column position.

of the Ta and Sc X-ray signal, removing any doubt about the composition. Figure 4.5(a) and (b) show respectively a simultaneously acquired ADF image and EDX map corresponding to the Sc K and Ta L signals. This confirms the chequerboard ordering pattern and matching the intensities in 4.5(a) as expected. Additionally, taking a line profile (Fig. 4.5(c)) confirms that the columns are indeed mixed to varying degrees.

Due to the difficulties in quantifying the small changes in ordering on the local scale, it has been largely ignored here and, for simplicity, regions are described as entirely ordered or entirely disordered. However, the small variations in ordering should not be completely forgotten; if the degree of ordering has such a large effect on the bulk properties, it should not be entirely discarded from having an effect on the local scale.

4.2.2 Ionic displacements

The ergodic nature of PNRs makes it difficult to get a true structure that is not effectively an average of multiple structures or orientations (similar to the so-called adaptive phase in PZT [155]). TEM is the technique of choice when locally imaging

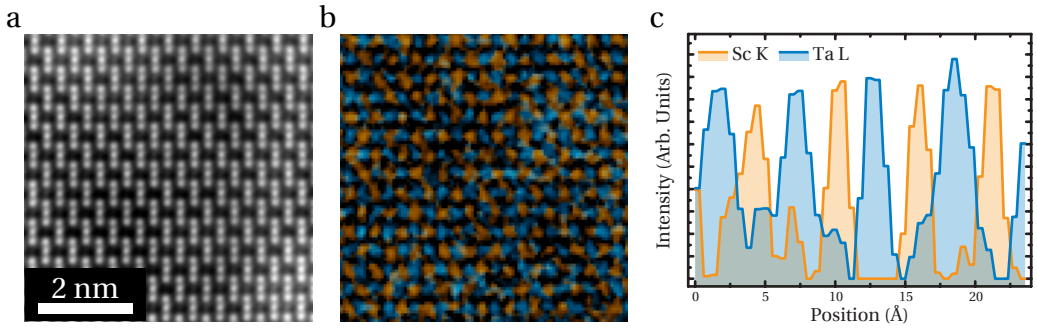

Figure 4.5: (a-b) Annular dark field image and the simultaneously acquired energy dispersive X-ray spectroscopy map for Ta (Blue) and Sc (Orange). (c) Profile taken from (b) showing the mixing of Ta and Sc columns.

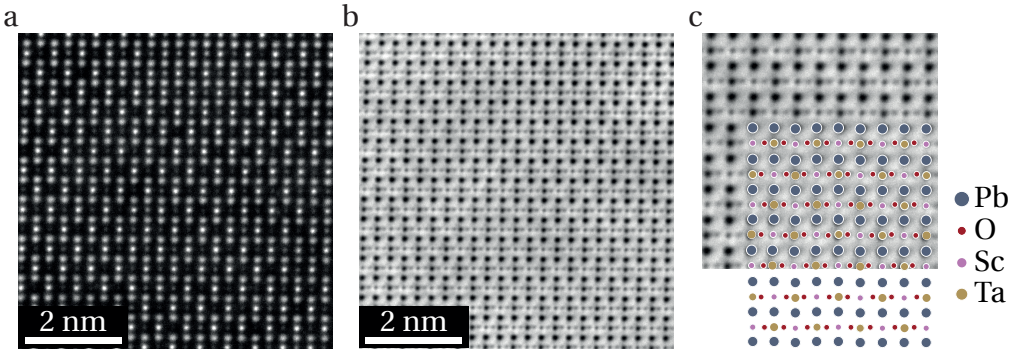

Figure 4.6: (a) Annular dark field and (b) annular bright field images along the $\langle 110 \rangle$ direction of Pb_2ScTaO_6. (c) shows an enlarged region of (b) with the structure overlaid to highlight the shift in oxygen positions.

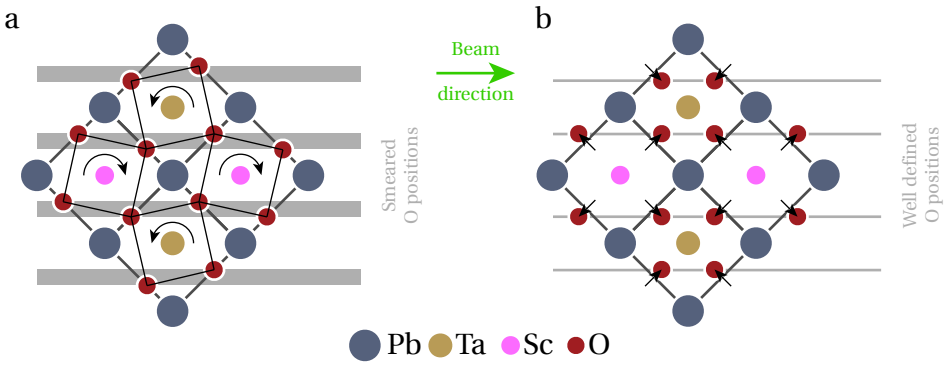

Figure 4.7: (a) Schematic of the projection effect of any oxygen octahedral rotation where there is a distribution of oxygen positions in the projection. (b) Schematic showing the projection effect of oxygen displacements towards and away from the Ta and Sc respectively. It can be seen that the oxygen positions still line up in the beam direction (left to right).

structure at the atomic scale. Figures 4.6(a) and (b) show simultaneously acquired ADF and ABF images from the [110] axis. The ABF images provide greater contrast for lighter elements and now the oxygen positions can be observed and measured (see section 2.1.5). If the PNR fluctuations are associated with a significant structure change, such as octahedral tilting, then the changing structure would present as ill defined, smeared out positions of the atoms in the ABF image, as shown in Fig. 4.7(a). Alternatively, if the PNR fluctuation rate is considered to be slow, any corresponding displacements in the oxygen positions would appear non-periodic. This is not the case, so the fluctuations cannot be attributed to any significant structural change at room temperature.

Interestingly, the oxygen atoms are actually shifted from their prototype structure positions towards the Ta columns by ~ 0.1 Å. If this displacement was a tilting displacement, the projection would appear either smeared or without displacement (depending on the tilt magnitude) as the tilt necessitates alternating displacements through the thickness of the specimen (see Fig. 4.7(a)). Instead this must be a kind of breathing distortion where the oxygens contract and expand towards the Ta and Sc ions respectively, as shown in Fig. 4.7(b) [156]. The shifts can

be explained by considering the atomic radii of the B-site ions. Sc has as radius of 0.87 Å compared to the radius of Ta at 0.74 Å, making Sc larger by 0.13 Å [157]. This agrees well with the measured difference of ~ 0.1 Å in the $\langle 110 \rangle$ directions (giving a displacement of 0.14 Å in $\langle 100 \rangle$) and indicates that there is no additional phenomenon, such as Jahn-Teller distortions, at play. It would be assumed that in less ordered PST crystals, the mixing of Ta and Sc columns would remove or average such distortions and they may be undetectable. If, however, such distortions do still exist on the local scale, they could be an important factor in the dynamics of the material.

It should be readily apparent that in the ADF images (Figs. 4.3 and 4.6), the intensity of the Ta-site appears brighter than the Pb columns. This goes against the stated power law that the intensity approximately varies proportionally to Z^2, where Z is the atomic number. Ta and Pb have atomic numbers of 73 and 82 respectively and therefore Pb would be expected to appear brighter. Figure 4.8(a) shows the Voronoi intensities of all the column types from Fig. 4.3(a) where it can be seen that the Pb intensities have a slightly higher average, but there is a lot of overlap with the Ta intensities. Figure 4.8(b) shows the average intensities as a function of scaling the fraction of the Voronoi cell considered [158] and shows that the Ta columns have a higher intensity than the Pb columns towards the middle of the peak but at larger averaging areas, the Pb is actually more intense. In other words, the peaks corresponding to the Ta positions are brighter but narrower whereas the Pb peaks are dimmer but broader.

This breaking of the intensity power law has previously been explained via changes in the Debye-Waller factors (atomic vibrations), from small displacements in the atom columns that broaden the measured peak or from channelling effects [116, 159–161]. This would make sense in the context of PST as the polar fluctuations are expected to appear as displacements of the atoms perpendicular to the beam direction or, alternatively, the rapid fluctuations could be interpreted as large

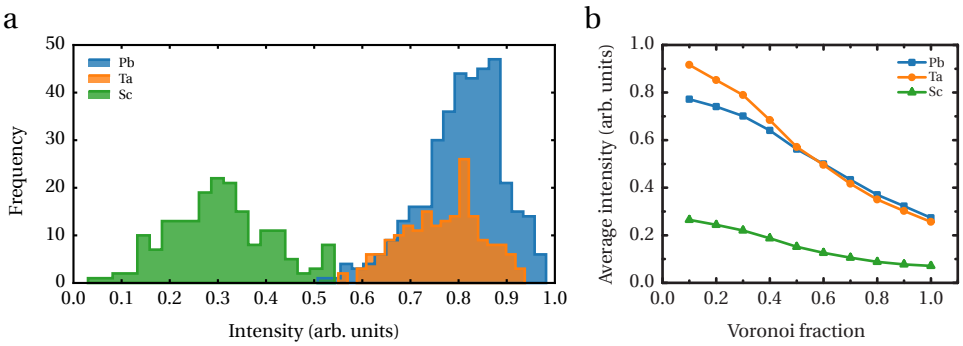

Figure 4.8: Histogram of peak intensities measured from Fig. 4.3(a). Intensities were measured as the average of the data within the Voronoi cell about the peak centre. (b) Average intensities for varying the fraction of the Voronoi cell summed over (always centred on the column position).

Table 4.1: Mean square displacements for Pb_2ScTaO_6 at 400 K. Data calculated by Woodward & Baba-Kishi [89].

Element	U_{iso} (Å^2)
Pb	0.0440
Ta	0.0096
Sc	0.0096
O	$U_{11} = 0.0085$
	$U_{22} = 0.0351$
	$U_{33} = 0.0351$

thermal vibrations that change the Debye-Waller factors. It has been reported in the literature that both the Pb ions and the B-site ions can be displaced [86, 162–164]. A large displacement or thermal vibration in the Ta column might be expected to make the peak broader but with a lower magnitude [126, 161]. Therefore, displacements in the Pb columns are put forward as the most plausible explanation.

To try and elucidate the origin of this phenomenon, PST structures have been simulated whilst changing parameters that would affect the intensity of the atomic columns. To form a baseline, Fig. 4.9(a) shows an ADF image simulated through a perfect PST crystal (i.e. no TDS, no displacements and perfect ordering). Here

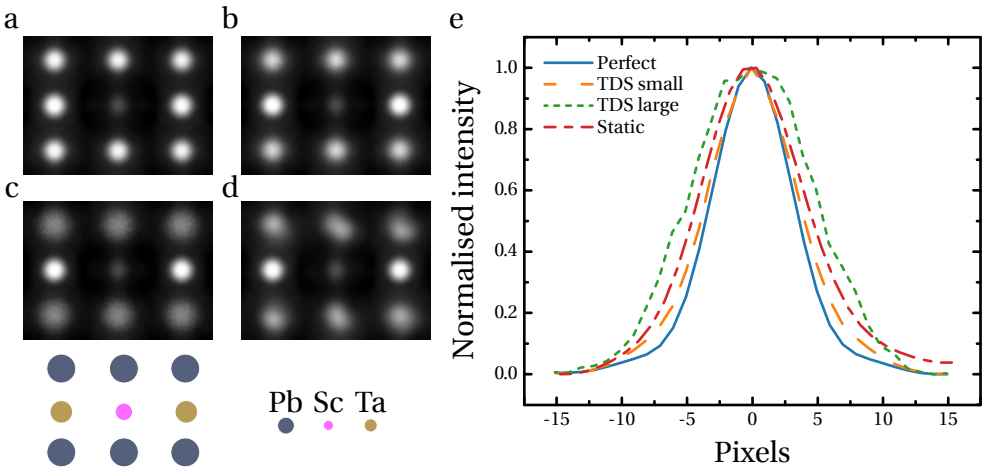

Figure 4.9: Annular dark field image simulations for: (a) perfect, (b) small thermal diffuse scattering (TDS) values from Table. 4.1, (c) large TDS estimated from the low temperature phase and (d) static displacements from the low temperature phase. (e) shows normalised profiles of the Pb columns from (a-d). For all simulations, crystal thicknesses of 20 nm were used. An annular dark field detector of radius 85-267 mrad was used with a beam convergence angle of 20 mrad. TDS was simulated using 20 configurations.

the intensities of the Ta and Pb are approximately equal, indicating there may be some channelling effects [116], however the difference is not large ($\sim$ 10%) and the small amount of disorder in the experimental images would only decrease the Ta column intensity. Further simulations then incorporate displacements and TDS taken from Woodward & Baba-Kishi [89]. Estimates for TDS values and displacements of the Pb ions have been taken from Woodward & Baba-Kishi [89] and have been reproduced in Table 4.1 whilst Fig. 4.10 shows the vibrations schematically. The corresponding simulation is shown in Fig. 4.9(b). Additionally, displacements have been taken from the low temperature phase, with a magnitude of 0.28 Å [89], to simulate static displacements (Fig. 4.9(c)) and TDS from PNR (and associated structure) fluctuations (Fig. 4.9(d)).

All simulations shown in Fig. 4.9(b-d) exhibit a reduced Pb column intensity compared to Fig. 4.9(a). Since it is difficult to experimentally determine the amount of disorder in each Ta/Sc column and simulate accordingly, it is fruitless to compare

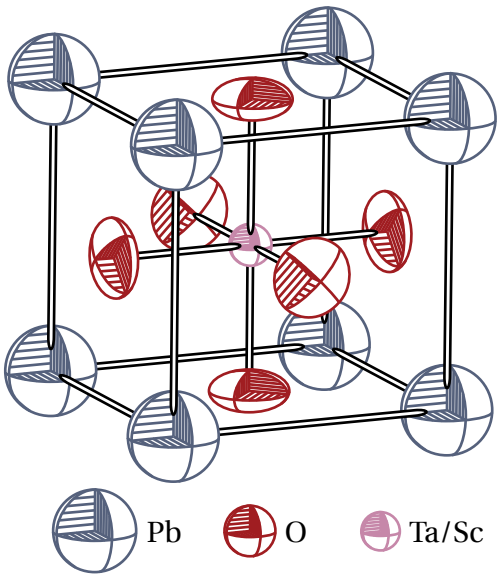

Figure 4.10: Thermal ellipsoids indicating the anisotropic atom displacements due to thermal vibrations for Pb_2ScTaO_6 as given by Table. 4.1. Pb are outlined in grey, O in red and Sc/Ta are represented by purple.

relative peak intensities. Instead, it is more rewarding to compare the shape of the peaks produced. The first observation is that the the Pb columns with static displacements are not rotationally symmetric. This is purely an effect of the model structure as the displacements are not truly random through the thickness of the specimen.

Figure 4.9(e) shows the profiles of the peaks from Fig. 4.9(a-d) where the intensities have been normalised to compare the shape of the peaks. The image simulated using the mean square displacements from Table 4.1 (Fig. 4.9(b)) shows a small change in the profile of the Pb columns that may produce the intensity switch demonstrated in Fig. 4.8(b). Increasing the Pb mean square displacement to 0.28 Å, to emulate the low temperature phase, (Fig. 4.9(c)) produces a further broadening in the profile of the peak and further reduces the intensity. Columns with Pb atoms statically displaced randomly up to 0.28 Å (Fig. 4.9(d)) also show a wider Pb column though less than simulations with equivalent TDS values. A fully quantitative analysis is not possible here, but it is feasible that a combination of

the static displacements and TDS can produce intensities and profiles as seen in the experimental ADF images (Fig. 4.8(b)). Note that oxygen position shifts, as seen in Fig. 4.6, have not been considered as oxygen atoms are not expected to change the intensity of the much heavier Pb/Ta columns in ADF imaging.

It is clear from the images that the Pb columns do not behave as would be expected from a conventional structure (i.e. PTO) and an obvious link is to the polar fluctuations. Comparing the Pb peaks to the Ta/Sc columns indicates that, in this crystal, it is the Pb ion and not the B-site ions that provide the main displacement to create the polarity. The difference between the TDS and the static model is the frequency of the displacements. As an electron travels through the material, it will see a single configuration of atoms if the frequency is much less than the speed of the electron. Likewise if the frequency of the displacements is much higher, the electron effectively sees multiple configurations of each atom, as is the case for TDS. Previous studies have shown the frequency of the PNRs to be on the order of 10 Hz [165], though nuclear magnetic resonance measurements (with time scales ~ 0.1 MHz [166]) show the PNRs to be dynamic [167]. It will be shown in section 4.4 that the PNRs can be observed at ~ 40 Hz and, though this would suggest static displacements are the cause of peak broadening, it is possible that a wide range of PNR fluctuation frequencies are found in one sample.

4.3 Low temperature phase transitions

It is predicted that a low-temperature, ferroelectric phase exists in PST. Now the structure has been explored at room temperature, it is interesting to see this transition to the low temperature phase. Here, several low-temperature methods are employed to find and characterise the potential transition.

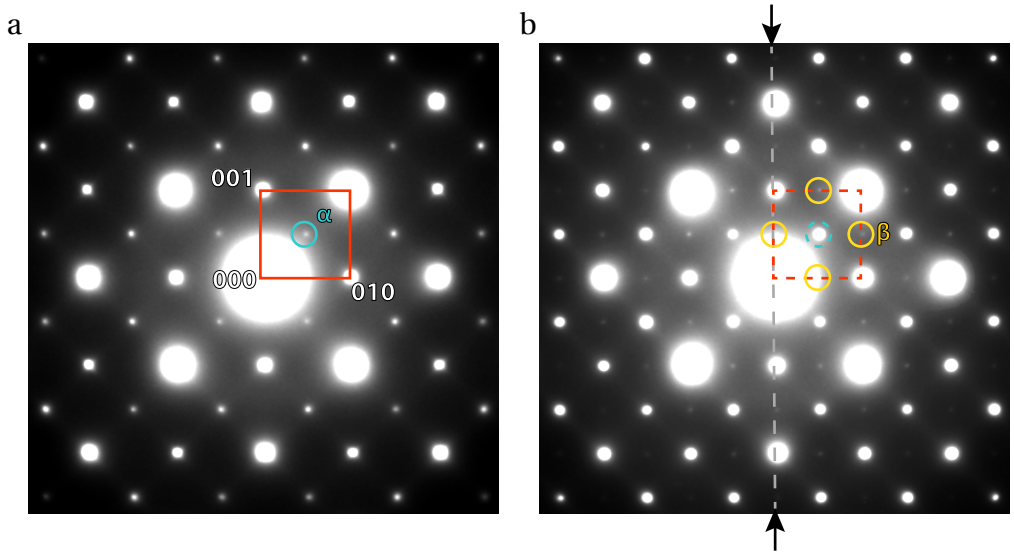

Figure 4.11: (a) Room temperature (296.5 K) $\langle 100 \rangle$ high dynamic range (HDR) electron diffraction image from Pb_2ScTaO_6. The reciprocal net has been highlighted in red with the α spots highlighted in blue. Some diffuse streaking is also visible in the 110 directions. (b) 122.9 K $\langle 100 \rangle$ HDR electron diffraction image taken from the same area as (a). All the spots are brighter but now extra β spots are visible and have been highlighted in orange. The arrows and grey dashed line indicate the profile shown in Fig. 4.12. Both HDR acquisitions used an initial exposure of 120 s.

4.3.1 Quantitative selected area diffraction

A simple method to expose the structure and potential phase changes in a material is selected area diffraction. Whilst not able to expose fine structure changes such as the small differences between cubic and rhombohedral phases (where the angle between the lattice vectors can change by $< 0.2^{\circ}$ [89]), it can easily show the presence of extra structural spots and can be performed on a relatively local scale ($<< 1$ μm^2). An example room temperature (296.5 K) $\langle 100 \rangle$ diffraction pattern is shown in Fig. 4.11(a), here two distinct types of diffraction spot are visible. The first set are the matrix spots, corresponding to the standard perovskite structure. A second set of spots, here called α spots, is present at the centre of the reciprocal unit cell. It is tempting to attribute these spots to the ordering within the sample, however in a $\langle 100 \rangle$ orientation, the ordered sites mix in the projection and cannot contribute to the extra spots; similar arguments can be made for the effect of the O-site displacements towards/away from the Ta/Sc positions.

It should be noted that whilst there are no $\frac{1}{2}$100 spots in Fig. 4.11(a), they are faintly visible in the room temperature $\langle 110 \rangle$ diffraction pattern (Fig. 4.1). However this could be due to multiple diffraction where the electron mean free path is much less than the thickness of the specimen. In this case, electrons diffracted to the $\frac{1}{2}$111 ordering spots may be diffracted again by the $\frac{1}{2}$100 planes to the $\frac{1}{2}$110 positions. Other multiple diffraction events will diffract onto and already existing reflection. In the $\langle 100 \rangle$ diffraction pattern, no reflections can multiply diffract to the $\frac{1}{2}$110 positions so the intensities must only be from the structure. Note also that, as the paraelectric transition temperature for this highly ordered PST is expected to be ~ 298 K, the material at room temperature (~ 296 K) will exhibit PNRs. Considering the paraelectric Fm$\bar{3}$m produces no extra spots so the structure should be thought of in terms of the dynamic, fluctuating PNR structure that is expected to be rhombohedral.

Figure 4.11(b) shows a diffraction pattern, taken under the same conditions,

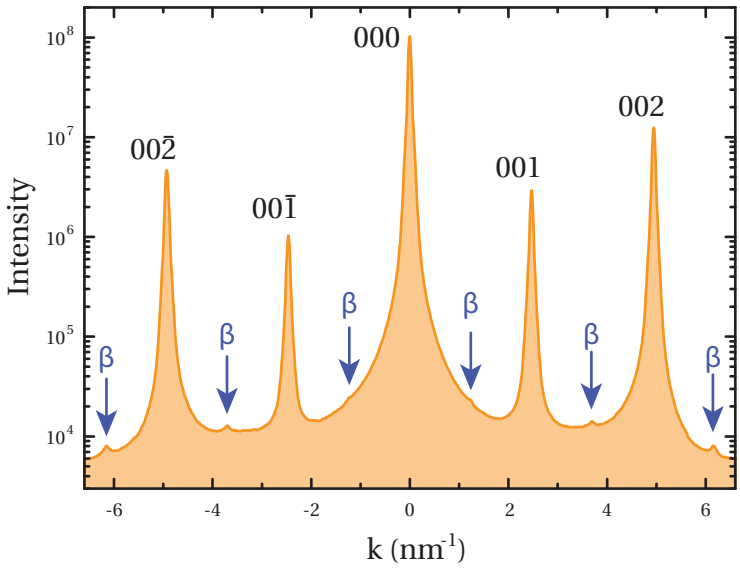

Figure 4.12: Profile of the diffraction intensity taken from the grey dashed line (indicated by arrows) in Fig. 4.11(b). Note the log scale. Blue arrows mark the positions of the β spots.

but now at a temperature of 122.9 K. As would be expected, the intensities of all peaks has increased due to the reduction of TDS, but an additional set of spots is now visible, here called the β spots. Note that the intensity of the central spot is ~ 4 orders of magnitude greater than the weak β spots (see Fig. 4.12), meaning that HDR imaging is necessary to acquire a full diffraction pattern.

To try and determine the origin of such spots, a series of diffraction patterns were acquired at different temperatures. To access information about the weak spots, their intensities need to be separated from those of the larger spots. To do this a simple background measurement was made using the average area inside a ring around the spot as demonstrated in Fig. 4.13. This averaging method effectively assumes a linear change of the background across the diffraction spot which is not the case as can be seen from the surrounding area. Therefore, any error in the background measurement was minimised by keeping the radius as small as possible to where the background curve is better approximated as linear. This procedure was

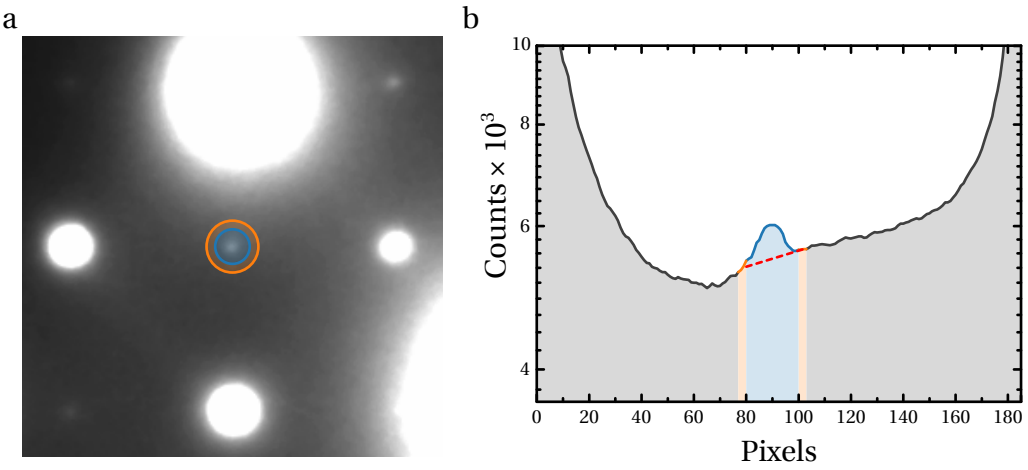

Figure 4.13: (a) Example of the regions used for signal (blue) and background (orange). (b) Profile from a low temperature $\langle 100 \rangle$ diffraction pattern demonstrating how the peak intensities were calculated. Blue indicates area designated as the signal, orange the background and grey is not considered. The red dashed line indicates the interpolated background signal under the peak.

then carried out on all the β spots up to the second order and all measurements were averaged across the diffraction pattern. So that all the peaks can be compared, even at larger g vectors where the spot intensities are decreased, the ratio of the signal to background is measured instead of the intensities.

Figure 4.14 shows the change in the weak spot intensity for both cooling and heating. Initially the β spots signal to background ratio is 1 or, in other words, the spots are not present. On cooling, the β spots remain absent until 220 K where there is a sudden, sharp increase in the intensity which then increases linearly with decreasing temperature. This transition is not repeated when reheating the sample to room temperature, instead the intensity changes in a smooth linear fashion matching that of the cooling but without the discontinuity. This clearly suggests some low-temperature phase transition that has not been explained before.

A transition at similar temperatures has been reported before by [168], though no explanation is offered and no indication of the extent of the order is given. A possible explanation is that after the PNRs form, they are the state of rapid

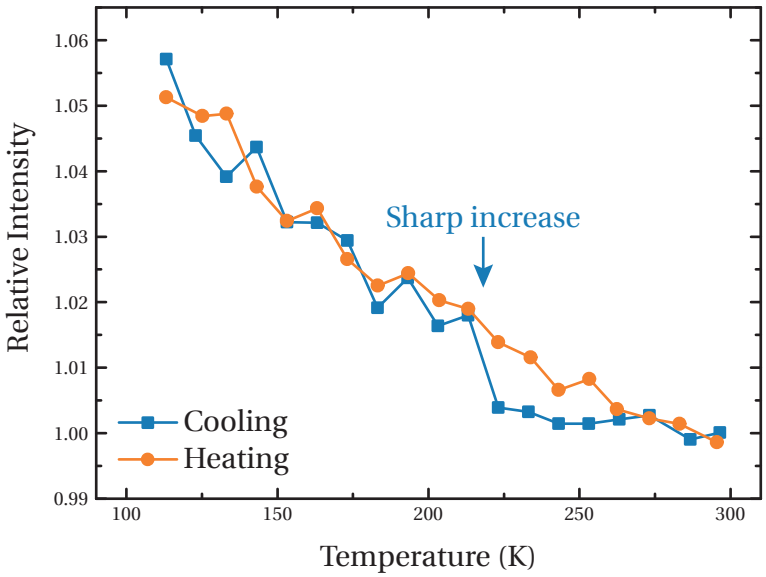

Figure 4.14: Ratio of the β spot intensities to the local background as a function of temperature for cooling (blue squares) and heating (orange circles). At room temperature the ratio is ~ 1, indicating that there is no peak. On cooling, there is a transition at 220 K which is not present in the heating data.

fluctuation. This causes the β spots to become so diffuse that they are not visible against the background. On further cooling to ~ 220 K, the PNRs suddenly coalesce and the diffuse β spots form defined peaks as a result of defined, static ferroelectric domains. On reheating the sample, the PNRs do not immediately return to the room temperature state and instead gradually start to fluctuate. This is much more of a continuous transition so the transition is not visible on heating and is reminiscent of more diffuse melting of water in confined pores [169].

Interestingly, Baba-Kishi & Pasciak found evidence for an incommensurate anti-ferroelectric state in similarly ordered PST (> 90 %) that exists in the range of 223 K to 323 K. This low-temperature transition could be related to the changes seen in the Fig. 4.14. However, they typically observed strong satellite peaks in their electron diffraction that are not visible in Figs. 4.1 or 4.11, though the diffuse streaking may be related.

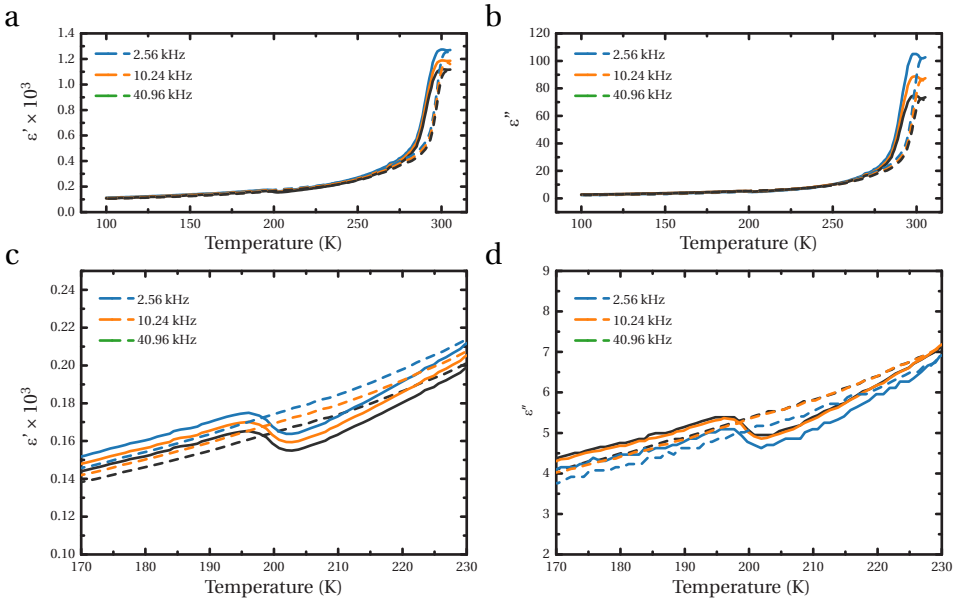

Figure 4.15: (a) and (b), real and imaginary part of the dielectric spectrum respectively. (c) and (d) show a subsection of (a) and (b), respectively, showing a small peak on cooling. Solid lines show the cooling spectrum and dashed lines show the heating for the frequencies given.

4.3.2 Dielectric spectroscopy

If it is the case that the low temperature transition is associated with the freezing of the PNRs, then dielectric spectroscopy is an ideal probe. By applying an alternating electric field, it is possible to see how the polar regions respond and then see how the response changes with temperature. Figures 4.15(a-b) show both real and imaginary parts of the dielectric permittivity. Most noticable is the large peak at 300 K, associated with the transition from paraelectric to the formation and coupling of PNRs (see section 1.4). Evidence that the highly ordered PST is not a true relaxor is that this peak position is not frequency dependent.

Closely examining the data reveals a noticeable, but small, peak starting at ~ 203 K as shown in Figs 4.15(c-d). This change is also only observable on the cooling cycle, in agreement with the transition found from electron diffraction. However, the temperature is different to the electron diffraction data by $\sim 10 - 20$ K.

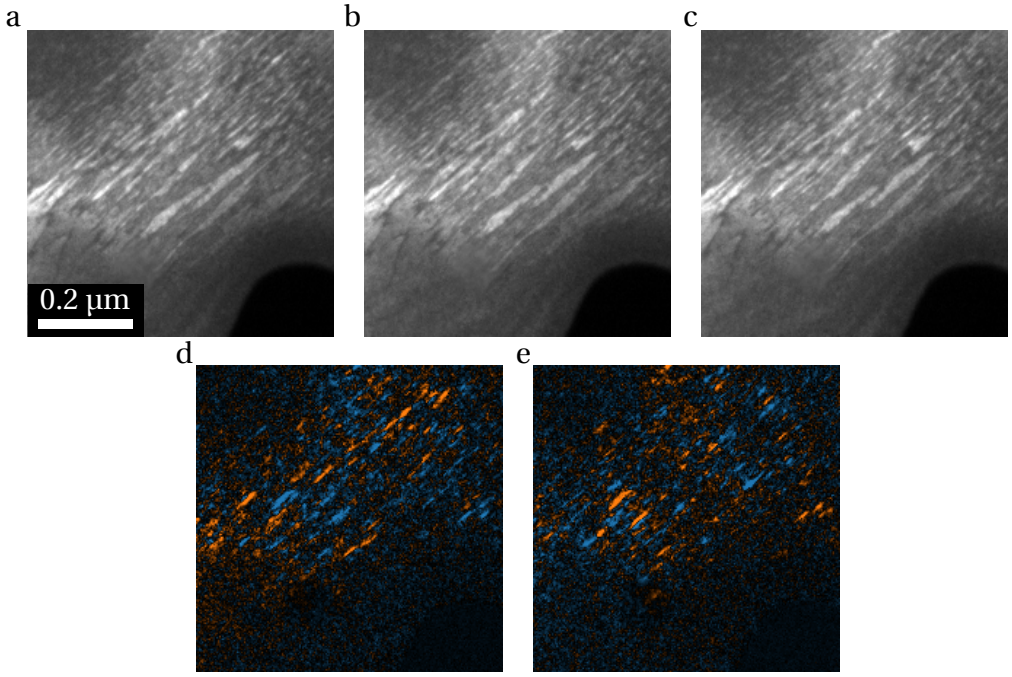

Figure 4.16: (a-c) Dark field images showing the polar nano domains at times separated by 0.2 s. (d) and (e) show the differences between (a) to (b) and (b) to (c) respectively. Blue and orange indicate a positive and negative change in intensity, respectively.

This can be reconciled by the inaccuracy of the temperature measurements of both systems. Looking at Sections 2.1.8 and 2.4 that detail the measurement equipment used, it can be seen that, particularly for the electron diffraction data, the temperature is measured and controlled several centimetres away from the specimen and relies on good conduction to the sensor. In the case of the electron diffraction data, the nitrogen has to cool down a $\sim$ 23 cm rod and then conduct heat away through limited contacts to the actual specimen, this can easily introduce a 10 K error. Alternatively, if the ordering is assumed to have an effect, then variations of the bulk ordering compared to the local area studied by SAED may produce such a temperature shift.

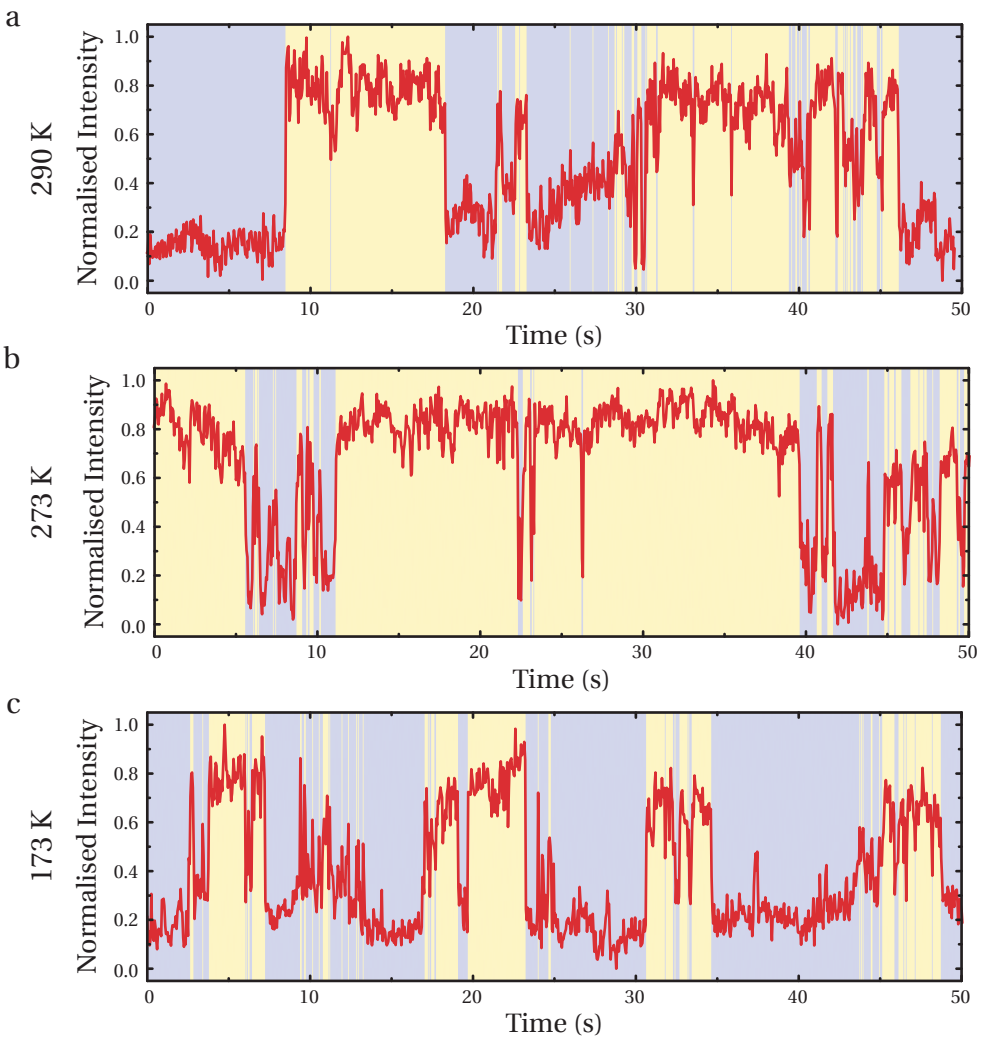

Figure 4.17: (a-c) intensities from a 3×3 region as a function of time for 290 K, 273 K and 173 K respectively. The blue and yellow backgrounds highlight the low and high intensity states.

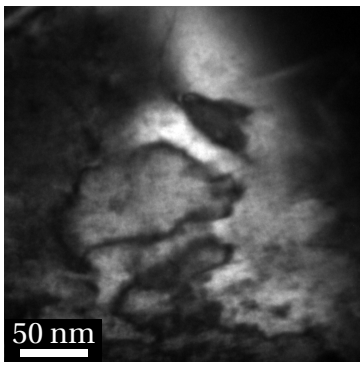

Figure 4.18: Dark field image taken at 230 K with contrast showing that large, single domains have formed.

4.4 Direct observation of polar nano regions

To try and elucidate the origin of the additional diffraction spots, dark field imaging can be performed using them. Fig. 4.16(a) gives an example of the contrast seen, bright and dark striations are visible. Perhaps the most interesting feature is that the contrast changes rapidly with time. This so called 'tweed' structure can be interpreted as the polar nano regions in the material. Figure 4.16 highlights the difference in the contrast with time, various regions of the image can be see to change from bright to dark and back again (and vice versa).

Figure 4.17(a) shows the intensity profile of one particular region as a function of time, recorded at 50 Hz. This shows that there is no obvious periodicity to the intensity profile. It should be noted that the acquisition time is 0.025 s per frame (limited by the CCD quantum efficiency and the total electron intensity) and it is possible that the fluctuation rate of the polar tweed is greater than the acquisition rate. Therefore, any fluctuations with a frequency greater than 40 Hz will not be detected in Fig. 4.17, instead an average of the fluctuations will be seen. It is also possible that different regions fluctuate at different rates and, to characterise the macroscopic sample, statistics on a high number of regions across the sample is needed. Nevertheless, some information can be gleaned by examining limited regions of the sample.

Figures 4.17(b) and (c) show the intensity profiles of selected regions for lower temperatures. Here it can be seen the independence of frequency with temperature. Initially the fluctuations seem to decrease by lowering the temperature from 290 K to 273 K, as might be expected from moving away from the dielectric maximum and as predicted by previous reports [91–93]. However, the specimen exhibits more frequent flickering on further lowering the temperature to 173 K, indicating that the predicted slowing of the fluctuations does not hold, at least for all areas of the sample.

This is in contrast to previous statements that at temperatures below $\sim$220 K, the tweed is expected to coalesce into static domains. Dark field imaging does reveal this to be true, as shown in Fig. 4.18, where large domains can be seen that no longer resemble the tweed structure seen in Fig. 4.16. However, some residual flickering tweed is still observed, even at 123 K, that indicates that the domains are not fully stable, particularly around defects and domain walls that may act to influence the PNRs [74, 170–172].

It is possible that this is an effect of introducing additional energy with the electron beam, this is also supported by the fact that it is also possible to move the frozen domains using the electron beam. Additionally, D-LACBED measurements support the idea that the domains are unstable under the electron beam. Figure. 4.19 shows a D-LACBED pattern taken at 203 K. Here it would be expected that there would be a breaking of symmetry to correspond to the change in crystal structure at lower temperatures, however this is not the case. It is possible then that the electron beam is indeed enough to excite the polar fluctuations and the average cubic structure is seen instead. This means that standard TEM measurements may struggle to determine the structure. Low dose methods may be required, though then the required signal will be hard to achieve.

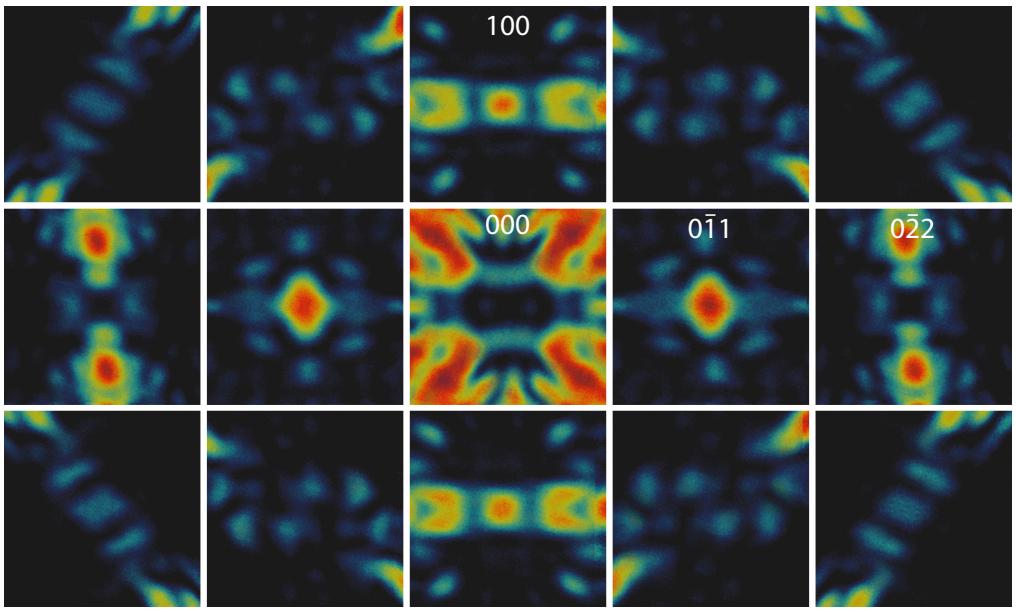

Figure 4.19: Digital large angle convergent beam electron diffraction pattern from the $\langle 110 \rangle$ zone axis of Pb_2ScTaO_6 at 203 K.

4.5 Chapter summary

Relaxors and relaxor like materials prove a challenge to understand, in part due to the varying phenomena with the level of ordering. Here highly ordered PST has been studied that gives a non-relaxor state as shown from the lack of frequency dependence of the dielectric maxima at T_m. First, the ordering has been thoroughly explored using dark field imaging and STEM, the high degree of ordering is seen to hold for the majority of the sample, permeated with APBs and local fluctuations in the disorder.

The atomic structure has also been examined using ADF-STEM. The dynamic nature of the sample provides limitations, but from the ADF intensities it can be inferred that the Pb atoms are displaced. Furthermore, ABF imaging revealed a previously unseen chequerboard expansion and contraction of the oxygen octahedra.

Finally, the dynamics of the sample have been examined. A low temperature phase transition has been found using novel SAED measurements and dielectric

spectroscopy, attributed to a freezing of the PNRs. Additionally, direct imaging of the polar domains show a freezing to a ferroelectric state, though individual PNRs do not appear to behave as theory might suggest.

Due to the dependence on ordering, the phenomena here have been described in context with the locally determined ordering. Several existing effects, such as the ordering and PNRs, have been studied using old (e.g. dark field, dielectric spectroscopy) and new (e.g. ADF-STEM, real-time dark field imaging) techniques. The new phenomenon of the low temperature phase transition has then been studied to add to the expansive jigsaw that makes up this complex material.

Chapter 5

Artefacts in strain measurements from atomic resolution images

5.1 Introduction

With the relatively widespread pervasion of aberration correctors, atomic resolution imaging is becoming routine. However, it is not always the case that the complimentary analysis methods take account of the differences between a conventional TEM image and an atomic resolution image. Strain analysis is an important technique that is frequently used in microscopy to aid in growth optimisation [173] and also for understanding the functional properties of materials [94, 174–178]. The two most common strain measurement methods, GPA and PP, were both developed before aberration correctors were widely available (1998 and 2007 respectively) and were only developed for lattice-resolution TEM [101, 102]. As such, extra care must be taken when measuring strain from atomic resolution Z-contrast image, even when using more modern techniques like the template matching method developed in 2014 [103].

The most obvious issue is the definition of strain in a crystal whose unit cell contains more than one distinct atom position. Ultimately several reference frames

can be chosen: Is the strain based on distances between atoms within the unit cell or is it on a unit cell by unit cell basis? If the latter is chosen then what point in the image defines the unit cell. Using the example of the ferroelectric PTO from chapter 3, the strain will change depending on whether the Pb or Ti is used to define the unit cell. In the end, this can only be resolved by the user with careful thought about the structure under consideration and what exactly they want to measure. Despite these complications, a large issue arises in GPA which is, unlike other techniques, a Fourier space technique. Whilst this presents a greater ease of use than other techniques (no image filtering or template generation to consider), it also obfuscates the underlying process to many casual users. With added complications, that will be examined in this chapter, it is then very easy for an incorrect strain analysis to be performed with no obvious warning. Related problems can also present themselves in the real space techniques, but the concepts that limit the strain analysis are easier to understand and therefore avoid.

5.2 Image formation in Fourier space

To understand the complications of examining atomic resolution, Z-contrast images using GPA, the knowledge of how such an image is created in Fourier space is necessary. Starting from the image formation of a simple, single atom lattice used by Hÿtch, Snoeck & Kilaas [101] and detailed in section 1.5.1:

$$I(\boldsymbol{r}) = \sum_{\mathrm{g}} H_{\mathrm{g}}(\boldsymbol{r}) \exp(2\pi i \boldsymbol{g} \cdot \boldsymbol{r}). \tag{5.1}$$

For an image with multiple sublattices, the image is described as a combination of a lattice (a mathematical array of points described by a 2D Dirac comb function $\mathrm{III} = \delta(\boldsymbol{r} - \boldsymbol{p}_j)$, where $\boldsymbol{p}_j$ are vectors describing the lattice points) and a basis image

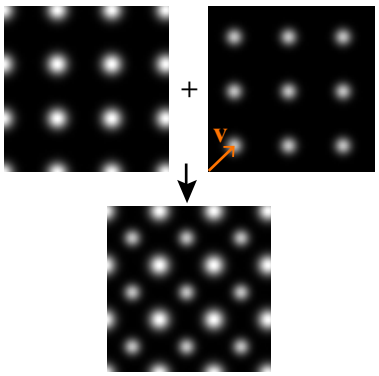

Figure 5.1: Demonstration of how an atomic resolution image with multiple sublattices is formed from two separate, single sublattice images, displaced by a vector $\boldsymbol{v}$ (orange arrow).

f (e.g. the image of the unit cell that is placed at each lattice point):

$$I(\boldsymbol{r}) = \text{III} \otimes f. \tag{5.2}$$

For simplicity, an image of two distinct sublattices is considered, A and B, though it should be obvious how to extend this to additional sublattices. Going back to fourier space, this multi-sublattice image can be described by:

$$I(\boldsymbol{r}) = \sum_g H_g^{\text{A}} \exp(2\pi i \boldsymbol{g} \cdot \boldsymbol{r}) + \sum_g H_g^{\text{B}} \exp(2\pi i \boldsymbol{g} \cdot \boldsymbol{r}) \exp(2\pi i \boldsymbol{g} \cdot \boldsymbol{v}), \tag{5.3}$$

where the A lattice has been taken as the origin and $\boldsymbol{v}$ is a vector describing the displacement between the sublattices (see Fig. 5.1). Assuming that the images of the A atoms are identical to the images of the B atoms, only differing in intensity, it can be written that

$$H_g^{\text{A}} = \alpha H_g \tag{5.4a}$$

$$H_g^{\text{B}} = \beta H_g \tag{5.4b}$$

where $H_g(\boldsymbol{r})$ are the Fourier coefficients of a normalised image of a single lattice

crystal. Using this, Eq. 5.3 can then be rewritten as a single Fourier series,

$$I(\boldsymbol{r}) = \sum_{\mathrm{g}} C_{\mathrm{g}} \exp(2\pi i \boldsymbol{g} \cdot \boldsymbol{r}) \exp(i\phi) \tag{5.5}$$

where

$$C_{\mathrm{g}} = H_{\mathrm{g}} \sqrt{\alpha^2 + \beta^2 + 2\alpha\beta \cos(2\pi \boldsymbol{g} \cdot \boldsymbol{v})} \tag{5.6a}$$

$$\tan\phi = \frac{\beta \sin(2\pi \boldsymbol{g} \cdot \boldsymbol{v})}{\alpha + \beta \cos(2\pi \boldsymbol{g} \cdot \boldsymbol{v})}. \tag{5.6b}$$

Note that Eq. 5.5 has exactly the same form as Eq. 5.1 but with an additional factor $e^{(i\phi)}$ that is related to the basis image. Thus, when applying GPA to a high resolution image with multiple sublattices, the calculated phase given by Eq. 1.8 becomes

$$P_{\mathrm{g}}(\boldsymbol{r}) = -2\pi \boldsymbol{g} \cdot \boldsymbol{u} + \phi(\boldsymbol{r}). \tag{5.7}$$

where there is the term $\phi(\boldsymbol{r})$ describing contributions from the basis image in addition to the lattice strain. This additional phase shift is what can cause artefacts in GPA.

5.3 Phase shifts at interfaces

First it should be noted that if the basis image does not change as a function of position, ϕ from Eq. 5.7 simply adds a constant phase across the whole image and has no effect on the strain components as it is the differential that is used. However, if the basis image changes, e.g. at an interface, then the additional phase will change as a function of position and can generate artefacts in the GPA results (leading to incorrect interpretations of the strain fields).

To illustrate this, a 1D case is first considered. Figure. 5.2 shows a series of peaks similar to those found in III-V semiconductors as well as the measured

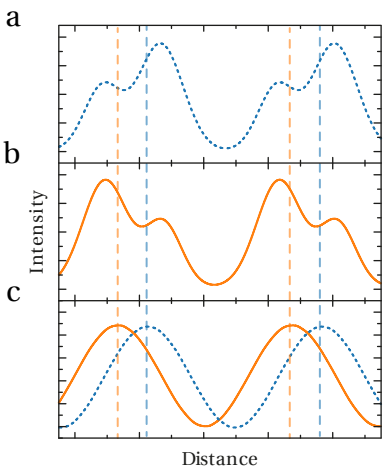

Figure 5.2: (a) and (b) Intensities representing a lattice built from a basis image with two peaks (bigger and smaller). The intensities have been swapped between (a) and (b). (c) The sine waves phases from (a) and (b) produced by filtering the g-vector corresponding to the unit cell size in real space.

sine wave when isolating just the g-vector corresponding to a single unit cell in real space. It is apparent that switching the intensities of the peaks changes the phase of the sine wave to more closely correspond to the most intense peak. Note that here more extreme cases are used to clearly indicate the phase changes, but cases where the relative peak intensities change will also produce smaller phase changes.

5.4 Strategies to remove strain artefacts

So far, origin of an additional, non-structural phase component has been identified, but it is not clear if this artefact can be removed or if it is inherently part of the analysis. Fortunately, the mathematics are quite simple. Taking Eq. 5.7, it is evident that ϕ, determined by Eq. 5.6b needs to be 0. This is trivially solved by setting the amplitude of the second sublattice, β, to zero, where the original single lattice case is formed. Alternatively, the sine term can be set to 0 by ensuring that the selected

g-vectors used in the analysis satisfy

$$\boldsymbol{g} \cdot \boldsymbol{v} = \frac{n}{2}, \tag{5.8}$$

where n is an integer (including zero). However, when n is an odd integer (so that $\frac{n}{2}$ is itself not an integer), then this has the effect that the intensity of the planes from Eq. 5.6a actually inverts and a maximal phase shift is observed. Therefore, Eq. 5.8 is refined to give

$$\boldsymbol{g} \cdot \boldsymbol{v} = n \tag{5.9}$$

as a rule to remove the additional phase that would compromise any strain analysis. Perhaps a more intuitive explanation is that the crystal planes selected from the FFT must contain all the sublattices.

It is therefore of the utmost importance that when presenting GPA strain analyses that the choice of $\boldsymbol{g}$-vectors is also given. Otherwise it is not clear if strain results are real or contain an artefact [173, 179–181].

5.5 Strain artefacts from geometric phase analysis of atomic resolution images

In this section, two experimental examples will be studied: An InGaAs-AlAsSb quantum cascade laser (QCL) device and a STO-$SrRuO_3$ (SRO) interface used as a buffer in a ferroelectric PZT device. To confirm the artefacts observed are an inherent part of the analysis (and not from other factors, e.g. noise or scan distortion), simulated images of ideal structures (i.e. containing no strain) have also been analysed by the same methods. The application of Eq. 5.9 is then demonstrated.

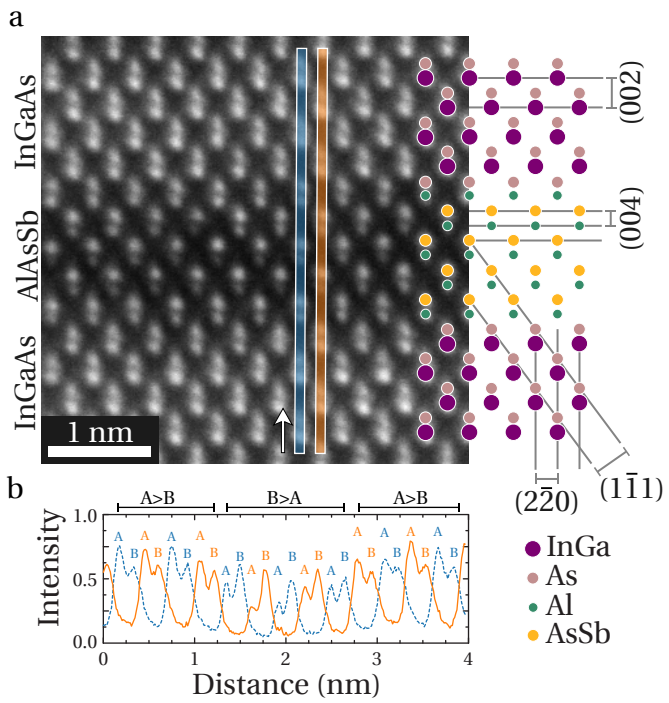

Figure 5.3: (a) Annular dark field image of an InGaAs-AlAsSb interface, as highlighted by the structure on the right along with the lattice planes. (b) Intensity profile of the boxed regions in (a) following the overlaid arrow.

5.5.1 InGaAs-AlAsSb

An ADF-STEM image of two interfaces in an epitaxial layer structure for a quantum cascade laser is shown in Fig. 5.3(a). In this image, taken along the $[110]$ crystal axis, the group III and group V atom columns are readily resolved as a 'dumbbell', with the lower part corresponding to the group III sublattice (A) and the upper part corresponding to the group V sublattice (B). The displacement of the two sublattices in this projection is $\boldsymbol{v} = \frac{1}{4}[001]$ (there is also a displacement along the incident electron beam direction, which has no effect on the image). The dark, horizontal, central band is a thin $AlAs_{0.8}Sb_{0.2}$ layer, roughly 3 monolayers in thickness, between $In_{0.7}Ga_{0.3}As$ layers (top and bottom). In such devices one is often interested in the ability to achieve the epitaxial design with sharp interfaces, and strain measurement can be a crucial part of this assessment. In this image, the relative intensities of the

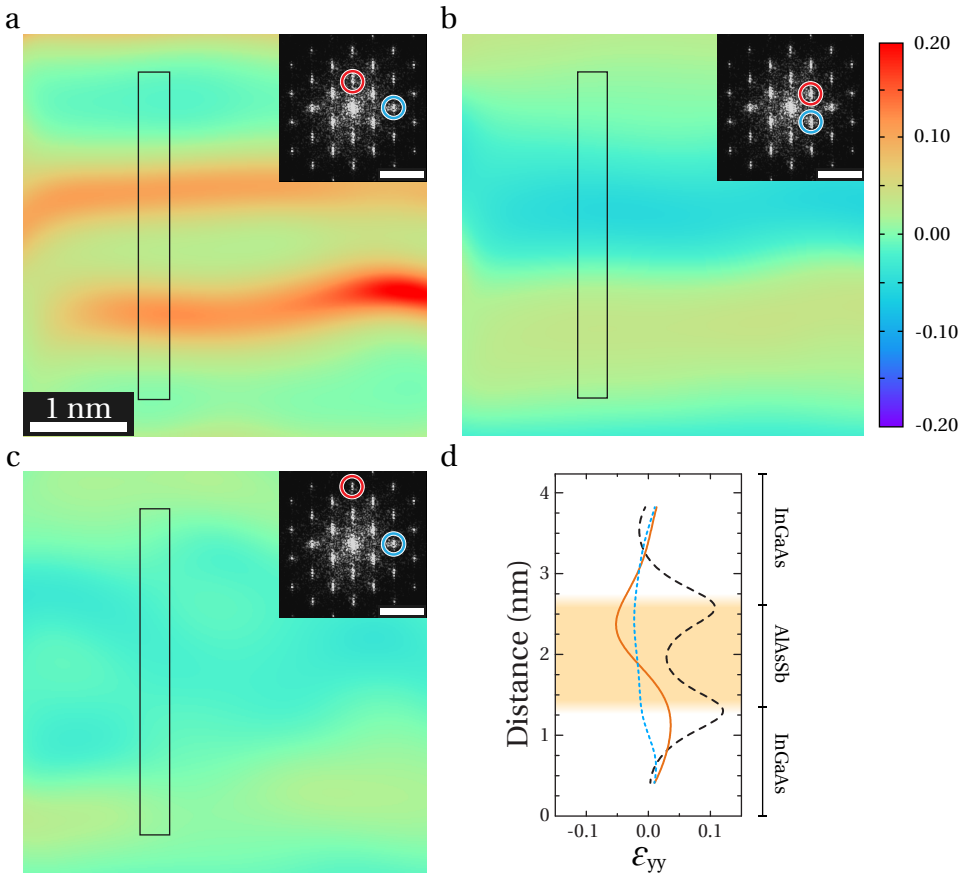

Figure 5.4: (a-c) ε_{yy} strain measured from Fig. 5.3(a) using the Bragg spots highlighted in the inset fast Fourier transforms (scale bars 5 nm^{-1}). (d) strain profiles from the boxed regions in (a) (dashed black), (b) (solid orange) and (c) (dotted blue). Fourier components were selected using a Gaussian mask with a full width half maximum of 0.81 nm^{-1}.

sublattice A and B swap as shown in Fig. 5.3(b). The occupancy of the A sublattice switches from In+Ga (brighter) to Al (fainter), while the B sublattice changes from As (fainter) to As+Sb (brighter).

Figure 5.3 has the characteristics of an image that will contain phase shifts in Fourier components that are caused by the basis image, rather than the lattice. Figure 5.4(a) shows the ε_{yy} output of GPA performed using Fig. 5.3(a), using the $\boldsymbol{g} = 002$ and $\boldsymbol{g} = 2\bar{2}0$ spots. Since $\boldsymbol{g} \cdot \boldsymbol{v} = \frac{1}{2}$ for $\boldsymbol{g} = 002$, this component is affected by the changes in the basis image. There is an apparent strain of 10% at the interfaces that does not agree with a visual inspection of the image. Conversely, $\boldsymbol{g} \cdot \boldsymbol{v} = 0$ for

the $\boldsymbol{g} = 2\bar{2}0$ and it is insensitive to this effect. Naively, one might hope that this issue may be overcome by avoiding the $\boldsymbol{g} = 002$ component and using, for example, the $\boldsymbol{g} = 111$-type Fourier components. Nevertheless, in this case $\boldsymbol{g} \cdot \boldsymbol{v} = \frac{1}{4}$. Therefore the $\boldsymbol{g} = \bar{1}1\bar{1}$ and $\boldsymbol{g} = \bar{1}11$ spots are also expected to produce specious strains at the interfaces, as is the case in Fig. 5.4(b). The effect is much smaller since $\boldsymbol{g} \cdot \boldsymbol{v}$ is small, and may be easily overlooked. A true strain map (Fig. 5.4(c)) is only obtained by choosing $\boldsymbol{g}$-vectors that obey Eq. 5.8, for example $\boldsymbol{g} = 004$ and $\boldsymbol{g} = 2\bar{2}0$. This shows the true strain at the interface to be only $\sim 1\%$. Note that the TEM specimen thickness will have a significant impact on quantitative strain measurements due to surface relaxation effects. Nevertheless, the contrast of ADF images is relatively insensitive to thickness, so has little impact on the results presented here.

It is apparent in Fig. 5.4 that there is some real lattice strain that is combined with the artefact produced by changes in basis image. In order to demonstrate phase shifts without any lattice strain, a similar procedure was performed on a multislice-simulated ADF-STEM image of a strain-free $In_{0.7}Ga_{0.3}As$-$AlAs_{0.8}Sb_{0.2}$ model heterostructure (Fig. 5.5). The GPA maps use the same sets of $\boldsymbol{g}$-vectors as used in Fig. 5.4. The apparent strains at the interfaces can be seen to have a similar sign and magnitude as in the experimental images of Fig. 5.4, although they are more visible (mainly because the interface is perfectly abrupt) and are zero in Fig. 5.5(d)

5.5.2 $SrTiO_3$-$SrRuO_3$

ABO_3 perovskites are the focus of intense study using aberration-corrected STEM [175, 182, 183], and as a compound material they can also exhibit erroneous strain when examined using GPA. This has on occasion been interpreted as a real interfacial strain [179]. Most investigations to date have used ADF-STEM, which is insensitive to the oxygen atoms, and so can be considered to produce biatomic images. However, annular bright field (ABF-STEM) is increasingly popular [120, 121, 184]

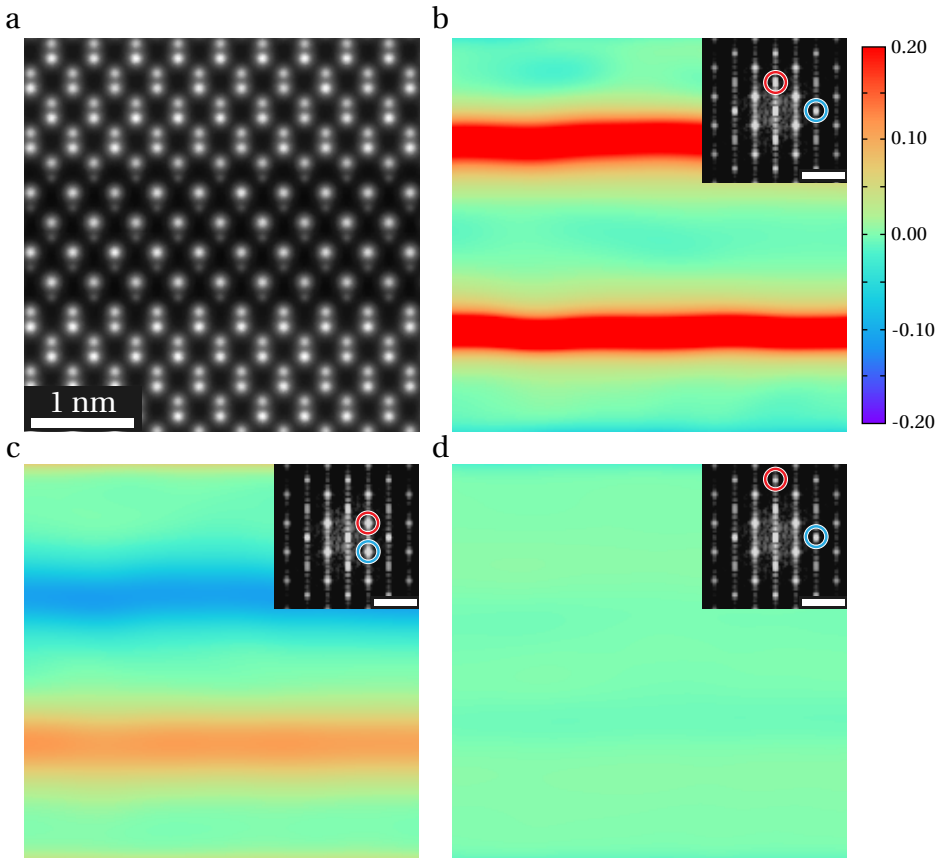

Figure 5.5: (a) Simulation of $In_{0.7}Ga_{0.3}As$-AlAsSb interfaces with a specimen thickness of 5 nm. (b-d) ε_{yy} strain measured using the Bragg spots highlighted in the inset fast Fourier transforms (scale bars 5 nm^{-1}). A Gaussian mask with full width half maximum of 0.68 nm^{-1} was used to select the Bragg spots.

since these images also show oxygen atoms [185, 186]. In $\langle 100 \rangle$ ABF-STEM images of such materials there are effectively four sublattices, meaning that great care must be taken in strain analysis. The analysis here is restricted to the simple case of a $[100]$ ADF-STEM image, with only two sublattices related by $\boldsymbol{v} = \frac{1}{2}[011]$ (note this choice of $\boldsymbol{v}$ is somewhat arbitrary since it can be defined modulo any lattice vector). An interface between STO (bottom) and SRO (top) is shown in Fig. 5.6(a) and, although the Sr sublattice remains constant across the interface, the A and B sublattices show a form of inversion in the basis image as $Z_{\mathrm{Ti}} < Z_{\mathrm{Sr}}$ in STO while in SRO $Z_{\mathrm{Ru}} > Z_{\mathrm{Sr}}$.

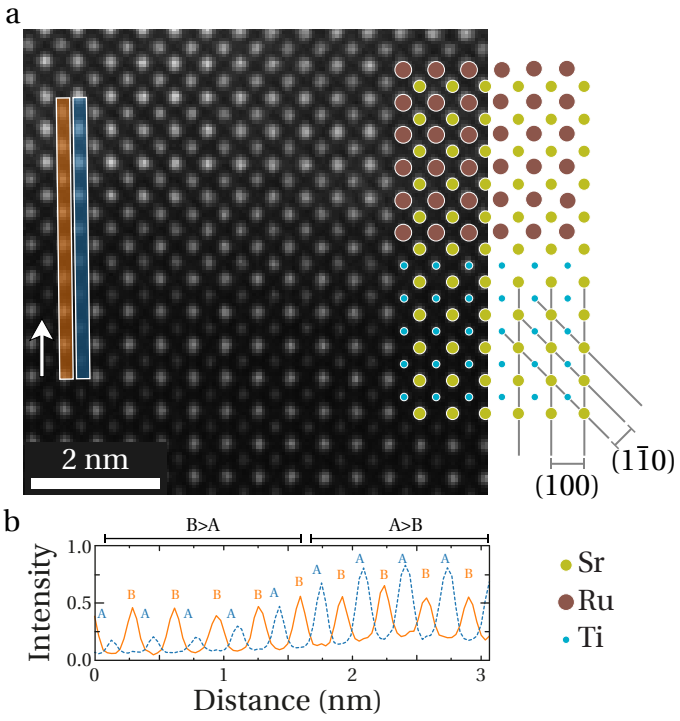

Figure 5.6: (a) Annular dark field image of an $SrTiO_3$-$SrRuO_3$ interface, as highlighted by the structure on the right along with the lattice planes. (b) Intensity profile of the boxed regions in (a) following the overlaid arrow.

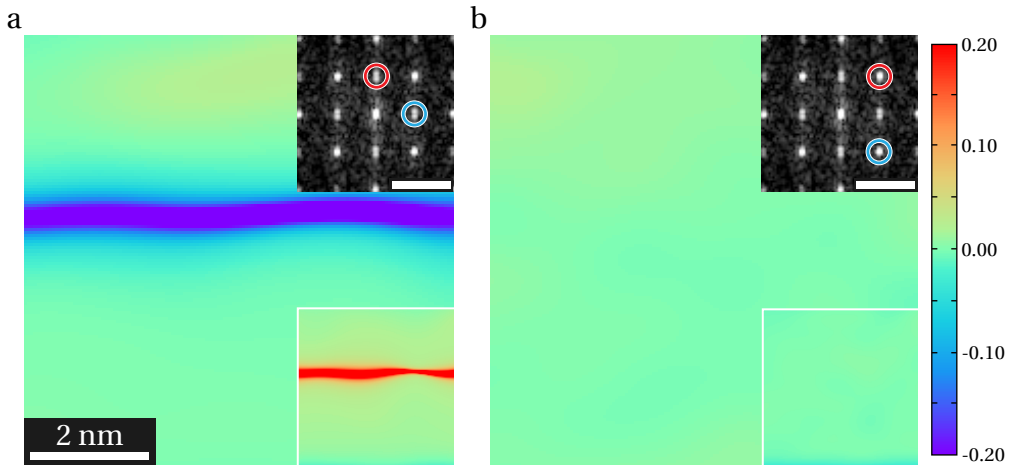

Figure 5.7: (a), (b) Geometric phase analysis strain maps from Fig. 5.6(a) for the ε_{xx} components and ε_{yx} components (lower insets) produced using the Bragg spots highlighted in the upper inset (scale bar 4 nm^{-1}). To select the fourier components, a Gaussian mask with a full width half maximum of 0.65 nm^{-1} was used.

In this case it is possible to produce artefacts that appear as large shear strains (that are clearly unphysical) as well as those that appear perpendicular to the interface. Figure 5.7(a) shows the axial and shear GPA maps produced using the $\boldsymbol{g} = 001$ and $\boldsymbol{g} = 0\bar{1}0$ Fourier components, both of which give $\boldsymbol{g} \cdot \boldsymbol{v} = \frac{1}{2}$. Since this gives a basis image-induced phase shift of π, strong artefacts in a GPA strain map are to be expected. Indeed, at the interfaces in Fig. 5.7(a), strains greater than 20% are found both in the ε_{yy} and ε_{yx} components. As before, such artefacts can be avoided by choosing spots such as $\boldsymbol{g} = 011$ and $\boldsymbol{g} = 0\bar{1}1$ that give $\boldsymbol{g} \cdot \boldsymbol{v} = 1$ and zero respectively 5.7(b). It is evident that there is in fact minimal strain in the image ($< 2\%$). Analysis of a simulated image from a strain-free model structure produces the same results (Fig. 5.8) with strains measured as zero in Fig. 5.8(c).

5.6 Phase shifts in other strain measurement methods

The effects of phase shifts at interfaces can be seen in other methods, though it is easier to notice and easier to diagnose in most cases.

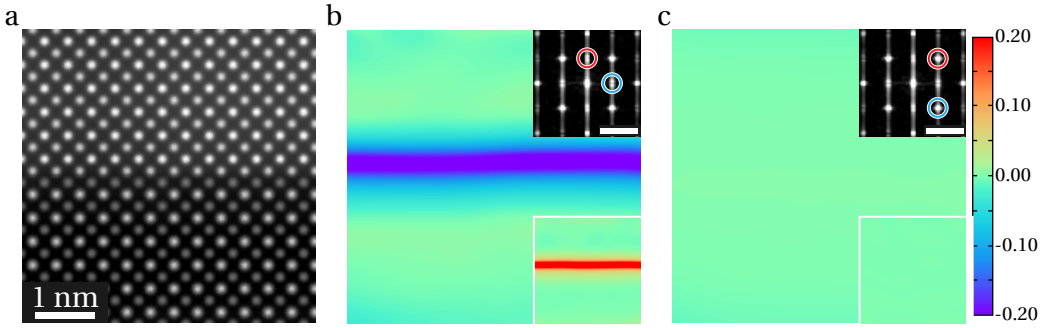

Figure 5.8: (a) Simulation of an $SrTiO_3$-$SrRuO_3$ interface with specimen thickness of 5 nm. (b), (c) Geometric phase analysis strain maps from (a), showing the ε_{xx} components and ε_{yx} components (lower insets). The inset fast Fourier transforms show the Bragg spots used for the analysis, scale bars are 4 nm^{-1}. Gaussian masks with full width half maximum of 0.60 nm^{-1} were used to select the Fourier components.

5.6.1 Template matching

Depending on the implementation, the template matching method of strain measurement can exhibit similar phase shift problems to GPA. Because the method relies on cross correlation to match the template to the experimental image, intensities will also be matched. Hence, if there is a phase shift in the intensities, there will be a corresponding phase shift in the cross correlation of the template. Figure. 5.9 shows an example using the STO-SRO system from Fig. 5.6. The QCL system from Fig. 5.3 is not susceptible to this problem in template matching as the intensity is mirrored, rather than a phase change. This means that, whilst any choice of template will match better in one orientation than another, the template will match at the sample position in all regions.

Template matching is often used merely as a form of image filter for use with PP, this can avoid the problems from Fig. 5.9 as well as other issues with matching a template around defects. Additionally, problems arising from template matching are often revealed during the analysis, as is the same for PP.

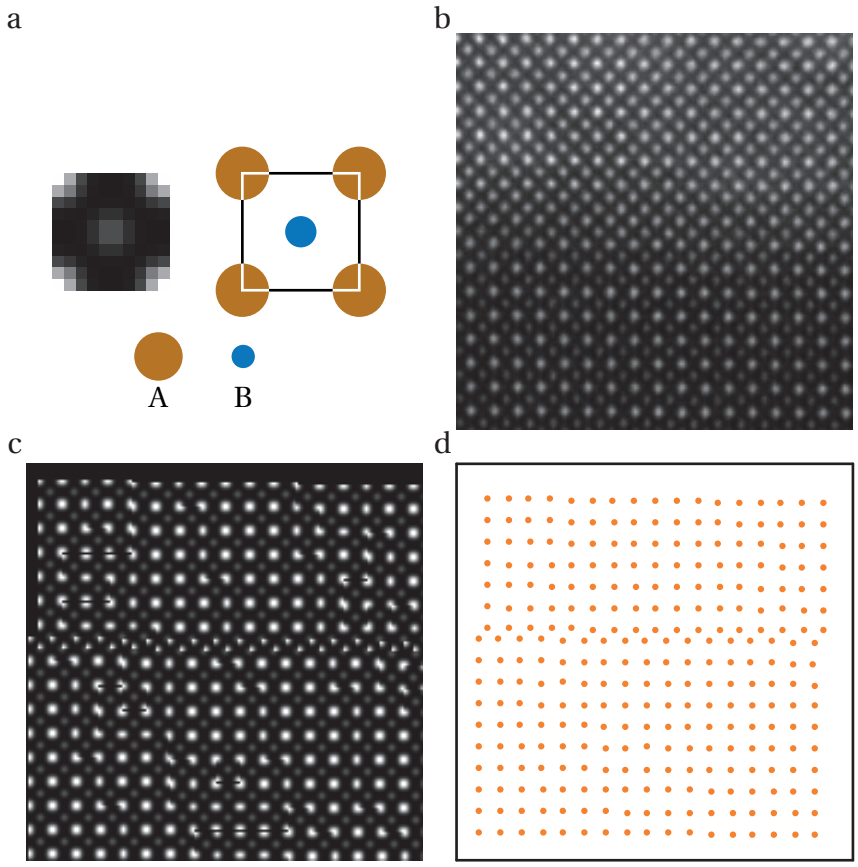

Figure 5.9: (a) template of a generic ABO_3 perovskite used for template matching with (b). (c) reproduction of (b) created by placing the template at the correlated positions that are shown in (d).

5.6.2 Peak pairs

In peak pairs, any phase shift does not inherently produce any error in the strain analysis. As long as all the peaks are detected, there is no preference for different intensities. Careful consideration should still be taken to consider what exactly is being measured, though this is system dependent as is the responsibility of the experimentalist. In addition, the peaks and lattice used to calculate strain are often shown and can easily be examined for error.

5.7 Chapter summary

Strain analysis is a useful and important tool for many areas of microscopy and material science. As microscope resolution has improved, existing methods for analysing images have not been reassessed. Here, GPA has been assessed mathematically and experimentally in its use for atomic resolution image of compound materials. Materials with multiple sublattices of different intensities have been shown to be susceptible to anomalous strain at interfaces and boundaries.

Methods have been presented to counter this effect, with the selection of the correct Bragg spots in the analysis being the key. Therefore, it is important that any GPA analysis is interpreted in relation to the Bragg spots chosen and that such information is always provided.

Additionally, a similar effect has been described in template matching, though it is expected that such effects will be easily noticeable due to the real space nature of the method.

Strain analysis is not any less valid due to the effects described here, it must simply be performed with more care and thought for what the analysis is actually measuring. The anomalies here are actually a result of additional information that may yet be used to glean extra insight into the materials studied.

Chapter 6

Conclusions and future work

In this thesis, the power of TEM has been leveraged to examine the structure and ferroelectricity in several perovskite oxides. The atom displacements that lead to ferroelectricity in such oxides is well suited to measurements using aberration corrected TEM. The exact nature of the polarisation, on a unit cell by unit cell basis, is an important factor in understanding how a ferroelectric system may function, particularly when considering nanoscale devices. Even in systems where the polarity is not static, TEM has been used to probe the local dynamics of the polarisation.

Chapter 3 shows the precise form of the polarisation in ferroelectric PTO within fully functional MFTJ devices. This has enhanced the understanding of how the devices work and how future devices may be made to function. Varying the film thickness was found to alter the depolarisation field caused by bound charges and the polarisation reconfigures to compensate for this. The 3.6 nm thick film exhibits a more traditional Kittel type domain configuration, the 2.4 nm thick film shows a complex domain structure with flux closure and polarisation curling. At the limit of ferroelectricity, the 1.2 nm thick film displays uniform polarisation. This has been related to the depolarisation field, as the distance between the bound surface charges is reduced, the improper screening from the electrodes creates the need to reduce the average bound charge. Additionally, the screening at the LSMO interface

has been shown to alter with film thickness, with the polarisation permeating into the electrode. Finally, examining the oxygen in the LSMO shows a link between octahedral rotation and the form of the polarisation.

Although the polarisation has been explored in a functional device, future work needs to answer the question of how the polarisation behaves as the device is functioning. As an electric field is applied, it might be expected that the polarisation would point in a uniform direction. However, this would increase the depolarisation field and might be expected to relax to some state with domains, possibly defeating the purpose of a non-volatile device. To fully understand this effect, in-situ electrical biasing measurements need to be made, where the polarisation can be switched and imaged at the same time. Another interesting aspect to be further explored is the effect of different electrodes and the choice of ferroelectric. The interplay of the depolarisation field, strain and screening mechanism provides a number of possible outcomes. The depolarisation could potentially be completely screened, producing a more classical domain pattern even at nanometre scale thicknesses. Alternatively, more intricate polarisation domains might be constructed, opening the possibility to control and manipulate toroidal polarisation.

In chapter 4, the complex nature of relaxor-like PST is examined using conventional TEM, atomic resolution STEM and in-situ techniques. To be able to study such a material properly, a thorough investigation of the chemical ordering was performed, finding a highly ordered crystal (> 85 %) permeated with disordered APBs. It has also been seen that there are slight variations in the ordering throughout the material, theorised to be instrumental in the material's properties. Additionally, a chequerboard distortion in the oxygen octahedra was found and has been attributed to the size of the ordered Sc and Ta ions.

The phenomenon that relaxors are most known for is the presence of PNRs. This thesis studies these rapidly fluctuating, polarised regions using ADF STEM, where the polarisation changes appear as large thermal vibrations in the image con-

trast. For the first time, direct measurements of PNR dynamics were made using dark field imaging. The results show that with decreasing temperature, in the limited regions examined, the PNR fluctuations do not slow or that the domain size does not grow, contrary to proposed theories. Further in-situ experiments found the presence of a phase transition at 220 K that might be associated with the freezing of PNRs into the ferroelectric phase.

The work presented here sets out a comprehensive study of the ordering that can be correlated with the material's properties. To build on this, a systematic study of different ordering and the related properties should be conducted. This would firstly allow a better comparison with the literature, that typically only focusses on one value of order at a time, but would also further the understanding of how the PNRs behave. For example, the expected behaviour of the frequency and size of the PNRs may only hold true for canonical relaxors or even a specific range of ordering.

Further understanding of the PNRs is still required and could be achieved by increasing the number of PNRs examined. It is currently unclear if the PNRs need to be studied as an average of a large number, or if the behaviour observed in this thesis holds for all PNRs. These large scale observations are not easily made using the direct measurements in dark field, but if the intensity of the diffraction spots are monitored in real time, some statistics on the fluctuations can be measured. The number of PNRs monitored could be roughly controlled by the size of the SAED aperture. Furthermore, advances in electron detection open the possibility to image the PNRs on timescales of < 0.01 s to examine the higher frequency dynamics.

Confusion still exists over the structural changes associated with the PNRs. This thesis proposes that the movement of the Pb cation causes the polarisation, though the some reports propose B-site cation movement as the source of the polarisation. A plausible explanation is that highly ordered PST exhibits Pb displacements and disorder produces B-site movement. Currently, no single study has been conducted to confirm this hypothesis, as is required.

The final results chapter presents a study of strain measurement from atomic resolution images with the caveats and pitfalls that arise from the increased image resolution. Since many of the strain measurement techniques were developed before the widespread availability of aberration corrected imaging, it is important to reassess exactly how the existing strain measurements work, and how they apply to the new information available in atomic resolution images. This thesis shows, mathematically and empirically, that GPA analysis at interfaces between materials with more than one sublattice can exhibit erroneous strain. This arises from additional phase shifts caused by the changes in sublattice intensities. A rule to avoid incorrect measurements of strain has then been laid out. Furthermore, this effect has been discussed with reference to the template matching method of measuring strain, where a similar problem can be found.

Further efforts should be used to exploit the extra information that interferes with the traditional GPA measurements. For example, a perfect 180° domain wall in PTO has no strain when considering the Pb lattice, but the opposite Ti displacements will provide some small phase shift in a GPA output. If this phase information could be separated from the lattice phase information, an easy way to map measure the Ti displacement, and hence the polarisation, across large areas could be developed. The difficulty arises in separating the phase information of two sublattices when they inherently have the same frequency. Further study of direct methods of imaging strain (e.g. electron holography) should also be made to detect if similar artefacts are present.

With the development of nanometre scale ferroelectric devices, characterisation of the properties on the atomic scale will become increasingly necessary. An understanding of polarisation and how it changes on these very local length scales is key in forming high density and effective devices. For this purpose TEM is indispensable and, with the continued development of analysis techniques, is likely to be a prominent tool for understanding and designing new devices.

Bibliography

[1] Feynman, R. P. *"There's plenty of room at the bottom."* Engineering and science **23,** 22–36 (1960).

[2] Drost, R., Ojanen, T., Harju, A. & Liljeroth, P. *"Topological states in engineered atomic lattices."* Nature physics (2017).

[3] Krivanek, O. L., Dellby, N. & Lupini, A. R. *"Towards sub-Å electron beams."* Ultramicroscopy **78,** 1–11 (1999).

[4] Haider, M., Hartel, P., Muller, H., Uhlemann, S. & Zach, J. *"Current and future aberration correctors for the improvement of resolution in electron microscopy."* Philosophical transactions of the royal society a: mathematical, physical and engineering sciences **367,** 3665–3682 (2009).

[5] Pennycook, S. J., Varela, M., Hetherington, C. J. D. & Kirkland, A. I. *"Materials advances through aberration-corrected electron microscopy."* Mrs bulletin **31,** 36–43 (2006).

[6] Kimoto, K. *et al. "Local crystal structure analysis with several picometer precision using scanning transmission electron microscopy."* Ultramicroscopy **110,** 778–782 (2010).

[7] Kim, Y.-M. *et al. "Probing oxygen vacancy concentration and homogeneity in solid-oxide fuel-cell cathode materials on the subunit-cell level."* Nature materials **11,** 888–894 (2012).

[8] Wang, Y., Salzberger, U., Sigle, W., Eren Suyolcu, Y. & van Aken, P. A. *"Oxygen octahedra picker: A software tool to extract quantitative information from STEM images."* Ultramicroscopy **168,** 46–52 (2016).

[9] Nord, M., Vullum, P. E., MacLaren, I., Tybell, T. & Holmestad, R. *"Atomap: a new software tool for the automated analysis of atomic resolution images using two-dimensional Gaussian fitting."* Advanced structural and chemical imaging **3** (2017).

[10] Van den Bos, K. *et al. "Locating light and heavy atomic column positions with picometer precision using ISTEM."* Ultramicroscopy **172,** 75–81 (2017).

[11] Klie, R., Arslan, I. & Browning, N. *"Atomic resolution electron energy-loss spectroscopy."* Journal of electron spectroscopy and related phenomena **143,** 105–115 (2005).

[12] Chen, Z. *et al. "Quantitative atomic resolution elemental mapping via absolute-scale energy dispersive X-ray spectroscopy."* Ultramicroscopy **168,** 7–16 (2016).

[13] Wenner, S., Jones, L., Marioara, C. D. & Holmestad, R. *"Atomic-resolution chemical mapping of ordered precipitates in Al alloys using energy-dispersive X-ray spectroscopy."* Micron **96,** 103–111 (2017).

[14] Fong, D. D. *et al. "Ferroelectricity in ultrathin perovskite films."* Science **304,** 1650–1653 (2004).

[15] Pantel, D. *et al. "Tunnel electroresistance in junctions with ultrathin ferroelectric* $Pb(Zr_{0.2}Ti_{0.8})O_3$ *barriers."* Applied physics letters **100,** 232902 (2012).

[16] Valasek, J. *"Piezo-electric and allied phenomena in rochelle salt."* Physical review **17,** 475–481 (1921).

[17] Von Hippel, A. *"Ferroelectricity, domain structure, and phase transitions of barium titanate."* Reviews of modern physics **22,** 221 (1950).

[18] Aizu, K. *"Possible species of ferromagnetic, ferroelectric, and ferroelastic crystals."* Physical review b **2,** 754 (1970).

[19] Scott, J. F. *"Ferroelectrics go bananas."* Journal of physics: condensed matter **20,** 021001 (2008).

[20] Seidel, J. *et al. "Conduction at domain walls in oxide multiferroics."* Nature materials **8,** 229–234 (2009).

[21] Vanderbilt, D. & King-Smith, R. D. *"Electric polarization as a bulk quantity and its relation to surface charge."* Physical review b **48,** 4442–4455 (1993).

[22] Resta, R. *"Macroscopic electric polarization as a geometric quantum phase."* Epl **22,** 133 (1993).

[23] King-Smith, R. D. & Vanderbilt, D. *"First-principles investigation of ferroelectricity in perovskite compounds."* Physical review b **49,** 5828 (1994).

[24] Spaldin, N. A. *"A beginner's guide to the modern theory of polarization."* Journal of solid state chemistry. *Polar Inorganic Materials: Design Strategies and Functional Properties* **195,** 2–10 (2012).

[25] Jia, C.-L. *et al. "Unit-cell scale mapping of ferroelectricity and tetragonality in epitaxial ultrathin ferroelectric films."* Nature materials **6,** 64–69 (2007).

[26] Jia, C.-L. *et al. "Atomic-scale study of electric dipoles near charged and uncharged domain walls in ferroelectric films."* Nature materials **7,** 57–61 (2008).

[27] Tang, Y. L. *et al. "Atomic-scale mapping of dipole frustration at 90° charged domain walls in ferroelectric* $PbTiO_3$ *films."* Scientific reports **4** (2014).

[28] Mi, S.-B., Jia, C.-L., Vrejoiu, I., Alexe, M. & Hesse, D. *"Atomic-scale structure and properties of epitaxial* $PbZr_{0.2}Ti_{0.8}O_3/SrRuO_3$ *heterointerfaces."* Advanced materials interfaces **2,** 1500087 (2015).

[29] Spurgeon, S. R. *et al. "Polarization screening-induced magnetic phase gradients at complex oxide interfaces."* Nature communications **6,** 6735 (2015).

[30] Gao, P. *et al. "Atomic mechanism of polarization-controlled surface reconstruction in ferroelectric thin films."* Nature communications **7,** 11318 (2016).

[31] Petraru, A. *et al. "Wedgelike ultrathin epitaxial $BaTiO_3$ films for studies of scaling effects in ferroelectrics."* Applied physics letters **93,** 072902 (2008).

[32] Béa, H. *et al. "Ferroelectricity down to at least 2 nm in multiferroic $BiFeO_3$ epitaxial thin films."* Japanese journal of applied physics **45,** L187 (2006).

[33] Gajek, M. *et al. "Tunnel junctions with multiferroic barriers."* Nature materials **6,** 296–302 (2007).

[34] Li, C. *et al. "Ultrathin $BaTiO_3$-based ferroelectric tunnel junctions through interface engineering."* Nano letters **15,** 2568–2573 (2015).

[35] Quindeau, A. *et al. "Four-state ferroelectric spin-valve."* Scientific reports **5,** 9749 (2015).

[36] Kittel, C. *"Theory of the structure of ferromagnetic domains in films and small particles."* Physical review **70,** 965–971 (1946).

[37] Lai, B.-K., Ponomareva, I., Kornev, I., Bellaiche, L. & Salamo, G. *"Thickness dependency of 180° stripe domains in ferroelectric ultrathin films: A first-principles-based study."* Applied physics letters **91,** 152909 (2007).

[38] Garcia, V. & Bibes, M. *"Ferroelectric tunnel junctions for information storage and processing."* Nature communications **5,** 4289 (2014).

[39] Stengel, M., Vanderbilt, D. & Spaldin, N. A. *"Enhancement of ferroelectricity at metal–oxide interfaces."* Nature materials **8,** 392–397 (2009).

[40] Velev, J. P. *et al. "Magnetic tunnel junctions with ferroelectric barriers: Prediction of four resistance states from first principles."* Nano letters **9,** 427–432 (2009).

[41] Kretschmer, R. & Binder, K. *"Surface effects on phase transitions in ferroelectrics and dipolar magnets."* Physical review b **20,** 1065–1076 (1979).

[42] Zhou, C. & Newns, D. M. *"Intrinsic dead layer effect and the performance of ferroelectric thin film capacitors."* Journal of applied physics **82,** 3081–3088 (1997).

[43] Stengel, M. & Spaldin, N. A. *"Origin of the dielectric dead layer in nanoscale capacitors."* Nature **443,** 679–682 (2006).

[44] Hwang, C. S. *"Thickness-dependent dielectric constants of (Ba,Sr)TiO_3 thin films with Pt or conducting oxide electrodes."* Journal of applied physics **92,** 432–437 (2002).

[45] Kim, D. J. *et al. "Polarization relaxation induced by a depolarization field in ultrathin ferroelectric $BaTiO_3$ capacitors."* Physical review letters **95,** 237602 (2005).

[46] Plonka, R., Dittmann, R., Pertsev, N. A., Vasco, E. & Waser, R. *"Impact of the top-electrode material on the permittivity of single-crystalline $Ba_{0.7}Sr_{0.3}TiO_3$ thin films."* Applied physics letters **86,** 202908 (2005).

[47] Tagantsev, A. K. & Stolichnov, I. A. *"Injection-controlled size effect on switching of ferroelectric thin films."* Applied physics letters **74,** 1326–1328 (1999).

[48] Ohtomo, A. & Hwang, H. Y. *"A high-mobility electron gas at the $LaAlO_3/SrTiO_3$ heterointerface."* Nature **427,** 423–426 (2004).

[49] Gerra, G., Tagantsev, A. K., Setter, N. & Parlinski, K. *"Ionic polarizability of conductive metal oxides and critical thickness for ferroelectricity in $BaTiO_3$."* Physical review letters **96** (2006).

[50] Zhuravlev, M. Y., Sabirianov, R. F., Jaswal, S. S. & Tsymbal, E. Y. *"Giant electroresistance in ferroelectric tunnel junctions."* Physical review letters **94,** 246802 (2005).

[51] Rodríguez Contreras, J. *et al. "Resistive switching in metal–ferroelectric–metal junctions."* Applied physics letters **83,** 4595–4597 (2003).

[52] Pantel, D., Goetze, S., Hesse, D. & Alexe, M. *"Reversible electrical switching of spin polarization in multiferroic tunnel junctions."* Nature materials **11,** 289–293 (2012).

[53] Choi, K. J. *et al. "Enhancement of ferroelectricity in strained $BaTiO_3$ thin films."* Science **306,** 1005–1009 (2004).

[54] Damodaran, A. R. *et al. "New modalities of strain-control of ferroelectric thin films."* Journal of physics: condensed matter **28,** 263001 (2016).

[55] Zhou, Z. D. & Wu, D. Y. *"Domain structures of ferroelectric films under different electrical boundary conditions."* Aip advances **5,** 107206 (2015).

[56] Yadav, A. K. *et al. "Observation of polar vortices in oxide superlattices."* Nature **530,** 198–201 (2016).

[57] Prosandeev, S., Ponomareva, I., Naumov, I., Kornev, I. & Bellaiche, L. *"Original properties of dipole vortices in zero-dimensional ferroelectrics."* Journal of physics: condensed matter **20,** 193201 (2008).

[58] Catalan, G. *et al. "Fractal dimension and size scaling of domains in thin films of multiferroic $BiFeO_3$."* Physical review letters **100,** 027602 (2008).

[59] Schilling, A. *et al. "Scaling of domain periodicity with thickness measured in $BaTiO_3$ single crystal lamellae and comparison with other ferroics."* Physical review b **74,** 024115 (2006).

[60] Mitsui, T. *"Domain structure of Rochelle salt and KH_2PO_4."* Physical review **90,** 193–202 (1953).

[61] Prosandeev, S. & Bellaiche, L. *"Asymmetric screening of the depolarizing field in a ferroelectric thin film."* Physical review b **75,** 172109 (2007).

[62] Goldschmidt, V. M. *"Die Gesetze der Krystallochemie."* Naturwissenschaften **14,** 477–485 (1926).

[63] Benedek, N. A. & Fennie, C. J. *"Why are there so few perovskite ferroelectrics?"* Journal of physical chemistry c **117,** 13339–13349 (2013).

[64] Mani, B. K., Chang, C.-M. & Ponomareva, I. *"Atomistic study of soft-mode dynamics in $PbTiO_3$."* Physical review b **88** (2013).

[65] Paul, A., Sun, J., Perdew, J. P. & Waghmare, U. V. *"Accuracy of first-principles interatomic interactions and predictions of ferroelectric phase transitions in perovskite oxides: Energy functional and effective Hamiltonian."* Physical review b **95** (2017).

[66] Glazer, A. M. *"The classification of tilted octahedra in perovskites."* Acta crystallographica section b: structural crystallography and crystal chemistry **28,** 3384–3392 (1972).

[67] Hirota, K., Wakimoto, S. & E. Cox, D. *"Neutron and X-ray scattering studies of relaxors."* Journal of the physical society of japan **75,** 111006 (2006).

[68] Aktas, O. *et al. "Ferroelectric precursor behavior in $PbSc_{0.5}Ta_{0.5}O_3$ detected by field-induced resonant piezoelectric spectroscopy."* Physical review b **88,** 174112 (2013).

[69] Randall, C. A., Barber, D. J., Whatmore, R. W. & Groves, P. *"A TEM study of ordering in the perovskite, $Pb(Sc_{1/2}Ta_{1/2})O_3$."* Journal of materials science **21,** 4456–4462 (1986).

[70] Stenger, C. G. F. & Burggraaf, A. J. *"Order–disorder reactions in the ferroelectric perovskites $Pb(Sc_{1/2}Nb_{1/2})O_3$ and $Pb(Sc_{1/2}Ta_{1/2})O_3$. II. Relation between ordering and properties."* Physica status solidi (a) **61,** 653–664 (1980).

[71] Chu, F., Setter, N. & Tagantsev, A. K. *"The spontaneous relaxor-ferroelectric transition of $Pb(Sc_{0.5}Ta_{0.5})O_3$."* Journal of applied physics **74,** 5129–5134 (1993).

[72] Dul'kin, E., Salje, E. K. H., Aktas, O., Whatmore, R. W. & Roth, M. *"Ferroelectric precursor behavior of highly cation-ordered $PbSc_{0.5}Ta_{0.5}O_3$ detected by acoustic emission: Tweed and polar nanoregions."* Applied physics letters **105,** 212901 (2014).

[73] Burns, G. *"Crystalline ferroelectrics with glassy polarization behavior."* Physical review b **28,** 2527–2530 (1983).

[74] Bokov, A. A. & Ye, Z.-G. *"Recent progress in relaxor ferroelectrics with perovskite structure."* Journal of materials science **41,** 31–52 (2006).

[75] Smolensky, G. *"Ferroelectrics with diffuse phase transition."* Ferroelectrics **53,** 129–135 (1984).

[76] Isupov, V. A., Pronin, I. P. & Sizykh, V. I. *"Investigation of the diffuse ferroelectric phase transition in leadmagnesium niobate."* Ferroelectrics **90,** 147–150 (1989).

[77] Cross, L. E. *"Relaxor ferroelectrics."* Ferroelectrics **76,** 241–267 (1987).

[78] Bokov, A. A. *"Influence of disorder in crystal structure on ferroelectric phase transitions."* Journal of experimental and theoretical physics **84,** 994–1002 (1997).

[79] Westphal, V., Kleemann, W. & Glinchuk, M. D. *"Diffuse phase transitions and random-field-induced domain states of the "relaxor" ferroelectric $PbMg_{1/3}Nb_{2/3}O_3$."* Physical review letters **68,** 847 (1992).

[80] Glinchuk, M. D. & Farhi, R. *"A random field theory based model for ferroelectric relaxors."* Journal of physics: condensed matter **8,** 6985 (1996).

[81] Pirc, R. *"Spherical random-bond–random-field model of relaxor ferroelectrics."* Physical review b **60,** 13470–13478 (1999).

[82] Shorrocks, N. M., Whatmore, R. W. & Osbond, P. C. *"Lead scandium tantalate for thermal detector applications."* Ferroelectrics **106,** 387–392 (1990).

[83] Stenger, C. G. F., Scholten, F. L. & Burggraaf, A. J. *"Ordering and diffuse phase transitions in $Pb(Sc_{0.5}Ta_{0.5})O_3$ ceramics."* Solid state communications **32,** 989–992 (1979).

[84] Sivasubramanian, V. & Kojima, S. *"Brillouin scattering studies of acoustic phonon modes and central peak in single-crystal $Pb(Sc_{1/2}Ta_{1/2})O_3$."* Physical review b **85** (2012).

[85] Baba-Kishi, K. Z. & Barber, D. J. *"Transmission electron microscope studies of phase transitions in single crystals and ceramics of ferroelectric $Pb(Sc_{1/2}Ta_{1/2})O_3$."* Journal of applied crystallography **23,** 43–54 (1990).

[86] Baba-Kishi, K. Z. & Pasciak, M. *"An electron diffraction and Monte Carlo simulation study of an incommensurate antiferroelectric state in the relaxor ferroelectric Pb_2ScTaO_6."* Journal of applied crystallography **43,** 140–150 (2010).

[87] Groves, P. *"Low-temperature studies of ferroelectric lead scandium tantalate."* Journal of physics c: solid state physics **18,** L1073 (1985).

[88] Stenger, C. G. F. & Burggraaf, A. J. *"Order–disorder reactions in the ferroelectric perovskites $Pb(Sc_{1/2}Nb_{1/2})O_3$ and $Pb(Sc_{1/2}Ta_{1/2})O_3$. I. Kinetics of the ordering process."* Physica status solidi (a) **61,** 275–285 (1980).

[89] Woodward, P. M. & Baba-Kishi, K. Z. *"Crystal structures of the relaxor oxide $Pb_2(ScTa)O_6$ in the paraelectric and ferroelectric states."* Journal of applied crystallography **35,** 233–242 (2002).

[90] Chang, Y.-J. & Chen, Z.-L. *"A study on ordered and ferroelectric domains in ordered $Pb(Sc_{1/2}Ta_{1/2})O_3$, ceramics."* Ferroelectrics letters section **4,** 13–18 (1985).

[91] Blinc, R. *"Field cooled and zero field cooled ^{207}Pb NMR and the local structure of relaxor $Pb(Mg_{1/3}Nb_{2/3})O_3$."* Physical review letters **91** (2003).

[92] Jeong, I.-K. *et al. "Direct observation of the formation of polar nanoregions in $Pb(Mg_{1/3}Nb_{2/3})O_3$ using neutron pair distribution function analysis."* Physical review letters **94** (2005).

[93] Dul'kin, E., Salje, E. K. H. & Roth, M. *"Evidence of presence of tweed in $Pb(Sc_{0.5}Ta_{0.5})O_3$ crystals based on acoustic emission frequency spectrum analysis."* Epl **111,** 47001 (2015).

[94] Peng, X., Tang, F. & Logan, P. *"Band structure of Si/Ge core-shell nanowires along the [110] direction modulated by external uniaxial strain."* Journal of physics: condensed matter **23,** 115502 (2011).

[95] Liu, H. L., Lin, M. K., Cai, Y. R., Tung, C. K. & Chu, Y. H. *"Strain modulated optical properties in $BiFeO_3$ thin films."* Applied physics letters **103,** 181907 (2013).

[96] Iuşan, D. *et al. "Effects of strain on ferroelectric polarization and magnetism in orthorhombic $HoMnO_3$."* Physical review b **87** (2013).

[97] Li, J., Shan, Z. & Ma, E. *"Elastic strain engineering for unprecedented materials properties."* Mrs bulletin **39,** 108–114 (2014).

[98] Schlom, D. G. *et al. "Elastic strain engineering of ferroic oxides."* Mrs bulletin **39,** 118–130 (2014).

[99] Hÿtch, M., Houdellier, F., Hüe, F. & Snoeck, E. *"Nanoscale holographic interferometry for strain measurements in electronic devices."* Nature **453,** 1086–1089 (2008).

[100] Koch, C. T., Özdöl, V. B. & van Aken, P. A. *"An efficient, simple, and precise way to map strain with nanometer resolution in semiconductor devices."* Applied physics letters **96,** 091901 (2010).

[101] Hÿtch, M. J., Snoeck, E. & Kilaas, R. *"Quantitative measurement of displacement and strain fields from HREM micrographs."* Ultramicroscopy **74,** 131–146 (1998).

[102] Galindo, P. L. *et al. "The peak pairs algorithm for strain mapping from HRTEM images."* Ultramicroscopy **107,** 1186–1193 (2007).

[103] Zuo, J.-M. *et al. "Lattice and strain analysis of atomic resolution Z-contrast images based on template matching."* Ultramicroscopy **136,** 50–60 (2014).

[104] Hÿtch, M. & Houdellier, F. *"Mapping stress and strain in nanostructures by high-resolution transmission electron microscopy."* Microelectronic engineering **84,** 460–463 (2007).

[105] Erni, R. *"Aberration-corrected imaging in transmission electron microscopy: an introduction."* (Imperial College Press, London, 2012).

[106] Pennycook, S. J. *et al. "Aberration-corrected scanning transmission electron microscopy: from atomic imaging and analysis to solving energy problems."* Philosophical transactions of the royal society a: mathematical, physical and engineering sciences **367,** 3709–3733 (2009).

[107] Kirkland, E. J. *"Advanced computing in electron microscopy."* 2nd Ed. (Springer, New York, 2010).

[108] Evans, K. & Beanland, R. *"High dynamic range electron imaging: The new standard."* Microscopy and microanalysis **20,** 1601–1604 (2014).

[109] Williams, D. B. & Carter, C. B. *"Transmission electron microscopy: a textbook for materials science."* (Springer, New York, 2009).

[110] Tanaka, M., Saito, R., Ueno, K. & Harada, Y. *"Large-angle convergent-beam electron diffraction."* Journal of electron microscopy **29,** 408–412 (1980).

[111] Beanland, R., Thomas, P. J., Woodward, D. I., Thomas, P. A. & Roemer, R. A. *"Digital electron diffraction – seeing the whole picture."* Acta crystallographica section a: foundations of crystallography **69,** 427–434 (2013).

[112] Brydson, R. *"Aberration-corrected analytical electron microscopy."* (Wiley, Chichester, 2011).

[113] Sanchez, A. M. *et al. "An approach to the systematic distortion correction in aberration-corrected HAADF images."* Journal of microscopy **221,** 1–7 (2006).

[114] Baba, N., Terayama, K., Yoshimizu, T., Ichise, N. & Tanaka, N. *"An autotuning method for focusing and astigmatism correction in HAADF-STEM, based on the image contrast transfer function."* Journal of electron microscopy **50,** 163–176 (2001).

[115] Bals, S., Kilaas, R. & Kisielowski, C. *"Nonlinear imaging using annular dark field TEM."* Ultramicroscopy **104,** 281–289 (2005).

[116] Haruta, M., Kurata, H., Komatsu, H., Shimakawa, Y. & Isoda, S. *"Effects of electron channeling in HAADF-STEM intensity in La_2CuSnO_6."* Ultramicroscopy **109,** 361–367 (2009).

[117] Walther, T. *"A new experimental procedure to quantify annular dark field images in scanning transmission electron microscopy."* Journal of microscopy **221,** 137–144 (2006).

[118] Findlay, S. D. *et al. "Robust atomic resolution imaging of light elements using scanning transmission electron microscopy."* Applied physics letters **95,** 191913 (2009).

[119] Findlay, S. D. *et al. "Dynamics of annular bright field imaging in scanning transmission electron microscopy."* Ultramicroscopy **110,** 903–923 (2010).

[120] Okunishi, E., Sawada, H. & Kondo, Y. *"Experimental study of annular bright field (ABF) imaging using aberration-corrected scanning transmission electron microscopy (STEM)."* Micron **43,** 538–544 (2012).

[121] Findlay, S. D., Kohno, Y., Cardamone, L. A., Ikuhara, Y. & Shibata, N. *"Enhanced light element imaging in atomic resolution scanning transmission electron microscopy."* Ultramicroscopy **136,** 31–41 (2014).

[122] Uhlemann, S. & Haider, M. *"Residual wave aberrations in the first spherical aberration corrected transmission electron microscope."* Ultramicroscopy **72,** 109–119 (1998).

[123] Wirth, R. *"Focused ion beam (FIB) combined with SEM and TEM: Advanced analytical tools for studies of chemical composition, microstructure and crystal structure in geomaterials on a nanometre scale."* Chemical geology **261,** 217–229 (2009).

[124] Beanland, R. *"Rapid cross-section TEM specimen preparation of III-V materials."* Microscopy today **11,** 29–31 (2003).

[125] Loane, R. F., Xu, P. & Silcox, J. *"Thermal vibrations in convergent-beam electron diffraction."* Acta crystallographica section a: foundations of crystallography **47,** 267–278 (1991).

[126] Wang, Z. L. *"Thermal diffuse scattering in sub-angstrom quantitative electron microscopy—phenomenon, effects and approaches."* Micron **34,** 141–155 (2003).

[127] Asami, K. *"Characterization of heterogeneous systems by dielectric spectroscopy."* Progress in polymer science **27,** 1617–1659 (2002).

[128] Schou, J. *"Physical aspects of the pulsed laser deposition technique: The stoichiometric transfer of material from target to film."* Applied surface science **255,** 5191–5198 (2009).

[129] Martin, L., Chu, Y.-H. & Ramesh, R. *"Advances in the growth and characterization of magnetic, ferroelectric, and multiferroic oxide thin films."* Materials science and engineering: r: reports **68,** 89–133 (2010).

[130] Yamada, H. *et al. "Giant electroresistance of super-tetragonal $BiFeO_3$-based ferroelectric tunnel junctions."* Acs nano **7,** 5385–5390 (2013).

[131] Yin, Y. W. *et al. "Enhanced tunnelling electroresistance effect due to a ferroelectrically induced phase transition at a magnetic complex oxide interface."* Nature materials **12,** 397–402 (2013).

[132] Wen, Z., Li, C., Wu, D., Li, A. & Ming, N. *"Ferroelectric-field-effect-enhanced electroresistance in metal/ferroelectric/semiconductor tunnel junctions."* Nature materials **12,** 617–621 (2013).

[133] Catalan, G., Scott, J. F., Schilling, A. & Gregg, J. M. *"Wall thickness dependence of the scaling law for ferroic stripe domains."* Journal of physics: condensed matter **19,** 022201 (2007).

[134] Keys, R. *"Cubic convolution interpolation for digital image processing."* Ieee transactions on acoustics, speech, and signal processing **29,** 1153–1160 (1981).

[135] Stigler, S. M. *"Gauss and the invention of least squares."* Annals of statistics **9,** 465–474 (1981).

[136] Marquardt, D. *"An algorithm for least-squares estimation of nonlinear parameters."* Journal of the society for industrial and applied mathematics **11,** 431–441 (1963).

[137] Joseph, J., Vimala, T. M., Sivasubramanian, V. & Murthy, V. R. K. *"Structural investigations on $Pb(Zr_xTi_{1-x})O_3$ solid solutions using the X-ray Rietveld method."* Journal of materials science **35,** 1571–1575 (2000).

[138] Schaffer, B. *Stackbuilder* - http://dmscript.tavernmaker.de.

[139] Glazer, A. M. & Mabud, S. A. *"Powder profile refinement of lead zirconate titanate at several temperatures. II. Pure $PbTiO_3$."* Acta crystallographica section b: structural crystallography and crystal chemistry **34,** 1065–1070 (1978).

[140] Bellaiche, L. & Vanderbilt, D. *"Intrinsic piezoelectric response in perovskite alloys: PMN-PT versus PZT."* Physical review letters **83,** 1347–1350 (1999).

[141] Yankovich, A. B. *et al. "Picometre-precision analysis of scanning transmission electron microscopy images of platinum nanocatalysts."* Nature communications **5,** 4155 (2014).

[142] Jia, C.-L., Urban, K. W., Alexe, M., Hesse, D. & Vrejoiu, I. *"Direct observation of continuous electric dipole rotation in flux-closure domains in ferroelectric $Pb(Zr,Ti)O_3$."* Science **331,** 1420–1423 (2011).

[143] Junquera, J. & Ghosez, P. *"Critical thickness for ferroelectricity in perovskite ultrathin films."* Nature **422,** 506–509 (2003).

[144] Park, J.-H. *et al. "Direct evidence for a half-metallic ferromagnet."* Nature **392,** 794–796 (1998).

[145] Pöttker, H. & Salje, E. K. H. *"Flexoelectricity, incommensurate phases and the Lifshitz point."* Journal of physics: condensed matter **28,** 075902 (2016).

[146] Haun, M. J., Furman, E., Jang, S. J., McKinstry, H. A. & Cross, L. E. *"Thermodynamic theory of $PbTiO_3$."* Journal of applied physics **62,** 3331–3338 (1987).

[147] Sharma, H., Kreisel, J. & Ghosez, P. *"First-principles study of $PbTiO_3$ under uniaxial strains and stresses."* Physical review b **90** (2014).

[148] Zhang, H.-M., An, M., Yao, X.-Y. & Dong, S. *"Orientation-dependent ferroelectricity of strained $PbTiO_3$ films."* Frontiers of physics **10,** 1–5 (2015).

[149] Wang, P.-Z., Cai, T.-Y., Ju, S. & Wu, Y.-Z. *"First-principles study of interface doping in ferroelectric junctions."* Scientific reports **6,** 24209 (2016).

[150] Wang, Y. *et al. "Ferroelectric dead layer driven by a polar interface."* Physical review b **82** (2010).

[151] Munkholm, A. *et al. "Antiferrodistortive reconstruction of the $PbTiO_3$(001) surface."* Physical review letters **88,** 016101 (2001).

[152] Bungaro, C. & Rabe, K. M. *"Coexistence of antiferrodistortive and ferroelectric distortions at the $PbTiO_3$ (001) surface."* Physical review b **71,** 035420 (2005).

[153] Cowley, R. A., Gvasaliya, S. N., Lushnikov, S. G., Roessli, B. & Rotaru, G. M. *"Relaxing with relaxors: a review of relaxor ferroelectrics."* Advances in physics **60,** 229–327 (2011).

[154] Osbond, P. C. & Whatmore, R. W. *"DiC17: High dielectric constant ceramics in the $PbSc_{0.5}Ta_{0.5}O_3$-$PbZrO_3$ system."* Ferroelectrics **133,** 159–161 (1992).

[155] Cordero, F., Trequattrini, F., Craciun, F. & Galassi, C. *"Octahedral tilting, monoclinic phase and the phase diagram of PZT."* Journal of physics: condensed matter **23,** 415901 (2011).

[156] Balachandran, P. V. & Rondinelli, J. M. *"Interplay of octahedral rotations and breathing distortions in charge-ordering perovskite oxides."* Physical review b **88** (2013).

[157] Shannon, R. D. *"Revised effective ionic radii and systematic studies of interatomic distances in halides and chalcogenides."* Acta crystallographica section a: crystal physics, diffraction, theoretical and general crystallography **32,** 751–767 (1976).

[158] Mostaed, A. *et al. "Atomic structure study of the pyrochlore $Yb_2Ti_2O_7$ and its relationship with low-temperature magnetic order."* Physical review b **95** (2017).

[159] LeBeau, J. M. *et al. "High-angle scattering of fast electrons from crystals containing heavy elements: Simulation and experiment."* Physical review b **79** (2009).

[160] Cosgriff, E., Nellist, P., Hirsch, P., Zhou, Z. & Cockayne, D. *"ADF STEM imaging of screw dislocations viewed end-on."* Philosophical magazine **90,** 4361–4375 (2010).

[161] Grillo, V., Carlino, E. & Glas, F. *"Influence of the static atomic displacement on atomic resolution Z-contrast imaging."* Physical review b **77** (2008).

[162] Mihailova, B. *et al. "Ferroic nanoclusters in relaxors: the effect of oxygen vacancies."* Journal of physics: condensed matter **19,** 246220 (2007).

[163] Mihailova, B., Maier, B., Steilmann, T., Dul'kin, E. & Roth, M. *"Electric-field-induced local structural phenomena in Pb-based ABO_3-type relaxor ferroelectrics."* Ieee transactions on ultrasonics, ferroelectrics, and frequency control **62,** 7–17 (2015).

[164] Baba-Kishi, K. Z. *"Direct observation of B-site cation displacements in Pb-based complex perovskite relaxor oxides."* Journal of applied crystallography **44,** 111–121 (2011).

[165] Bursill, L. A., JuLin, P., Hua, Q. & Setter, N. *"Relationship between nanostructure and dielectric response of lead scandium tantalate — (I) structure and domain textures."* Physica b: condensed matter **205,** 305–326 (1995).

[166] Blinc, R. *et al. "^{207}Pb NMR study of the relaxor behavior in $PbMg_{1/3}Nb_{2/3}O_3$."* Physical review b **63** (2000).

[167] Blinc, R., Gregorovič, A., Zalar, B., Pirc, R. & Lushnikov, S. G. *"^{45}Sc NMR study of the relaxor transition in a lead scandotantalate single crystal."* Physical review b **61,** 253 (2000).

[168] Abdulvakhidov, K. G., Mardasova, I. V., Myasnikova, T. P., Vitchenko, M. A. & Oshaeva, E. N. *"Phase transitions in $PbSc_{0.5}Ta_{0.5}O_3$."* Technical physics **55,** 514–516 (2010).

[169] Kondrashova, D., Reichenbach, C. & Valiullin, R. *"Probing pore connectivity in random porous materials by scanning freezing and melting experiments."* Langmuir **26,** 6380–6385 (2010).

[170] Chu, F., Reaney, I. M. & Setter, N. *"Role of defects in the ferroelectric relaxor lead scandium tantalate."* Journal of the american ceramic society **78,** 1947–1952 (1995).

[171] Baba-Kishi, K. Z., Tai, C. W. & Meng, X. *"Nanoscale global mixed ordering of B-site cations in $Pb_2M'M''O_6$ complex perovskite relaxors."* Philosophical magazine **86,** 5031–5051 (2006).

[172] Correa, M., Kumar, A. & Katiyar, R. S. *"Strain-induced relaxor behavior in $PbSc_{0.50}Nb_{0.25}Ta_{0.25}O_3$ thin films: A comparison with nanoceramics."* Journal of the american ceramic society **91,** 1788–1795 (2008).

[173] Nicolai, J. *et al. "Elastic strains at interfaces in InAs/AlSb multilayer structures for quantum cascade lasers."* Applied physics letters **104,** 031907 (2014).

[174] Wilks, S. P. *"Engineering and investigating the control of semiconductor surfaces and interfaces."* Journal of physics d: applied physics **35,** R77–R90 (2002).

[175] Hwang, H. Y. *et al. "Emergent phenomena at oxide interfaces."* Nature materials **11,** 103–113 (2012).

[176] Bellingeri, E. *et al. "T_c=21 K in epitaxial $FeSe_{0.5}Te_{0.5}$ thin films with biaxial compressive strain."* Applied physics letters **96,** 102512 (2010).

[177] Huang, S. X., Chien, C. L., Thampy, V. & Broholm, C. *"Control of tetrahedral coordination and superconductivity in $FeSe_{0.5}Te_{0.5}$ thin films."* Physical review letters **104,** 217002 (2010).

[178] Kim, Y. S. *et al. "Observation of room-temperature ferroelectricity in tetragonal strontium titanate thin films on $SrTiO_3$ (001) substrates."* Applied physics letters **91,** 2005–2008 (2007).

[179] Zhu, Y., Ophus, C., Ciston, J. & Wang, H. *"Interface lattice displacement measurement to 1 pm by geometric phase analysis on aberration-corrected HAADF STEM images."* Acta materialia **61,** 5646–5663 (2013).

[180] Oni, A. A. *et al. "Large area strain analysis using scanning transmission electron microscopy across multiple images."* Applied physics letters **106** (2015).

[181] Guzmán, R. *et al. "Polar-graded multiferroic $SrMnO_3$ thin films."* Nano letters **16,** 2221–2227 (2016).

[182] Varela, M. *et al. "Materials characterization in the aberration-corrected scanning transmission electron microscope."* Annual review of materials research **35,** 539–569 (2005).

[183] Park, D. *et al. "Studies of local structural distortions in strained ultrathin $BaTiO_3$ films using scanning transmission electron microscopy."* Microscopy and microanalysis **20,** 740–747 (2014).

[184] Huang, R. *et al. "Atomic-scale visualization of polarization pinning and relaxation at coherent $BiFeO_3/LaAlO_3$ interfaces."* Advanced functional materials **24,** 793–799 (2014).

[185] Aso, R., Kan, D., Shimakawa, Y. & Kurata, H. *"Control of structural distortions in transition-metal oxide films through oxygen displacement at the heterointerface."* Advanced functional materials **24,** 5177–5184 (2014).

[186] Dachraoui, W. *et al. "Local oxygen-vacancy ordering and twinned octahedral tilting pattern in the* $Bi_{0.81}Pb_{0.19}FeO_{2.905}$ *cubic perovskite."* Chemistry of materials **24,** 1378–1385 (2012).